ROMA TRE

UNIVERSITÀ DEGLI STUDI

DIPARTIMENTO DI INGEGNERIA

TESI DI DOTTORATO

Design, Development and Characterization of Stress-Optimized Ti-TiN
Multilayer PVD-Coatings

DOTTORANDO

Rashid Ali

Rashid Ali

COORDINATORE

Prof. Edoardo Bemporad

TUTOR

Prof. Edoardo Bemporad

CICLO XXVII

Abstract

Residual stresses in the PVD-coatings usually deteriorate the adhesion of coatings and adversely affect the performance of coated components. Nonetheless, it might have some positive effects such as resistance to crack nucleation and propagation, as well as wear and fatigue failures. A proper control of residual stress always remains essential for successful coating development. Multilayer systems with alternate hard (ceramic) and soft (metallic) layers compared with a monolayer, usually offer a much more ease to control the residual stresses, improve adhesion, increase overall thickness and produce the toughening response. However, in order to control the residual stresses, it is always important to find the optimal thickness of individual layers. An increase in metallic layer thickness significantly relieves the residual stress in ceramic layer. However, the performance of multilayer systems could be affected. Alternatively, an increase in thickness of ceramic layer close to the substrate could mostly increase the residual stress level. Hence the thickness of individual layers remains a key factor for the optimal performance of multilayer coating systems.

In the present work, finite element analysis (FEA) of residual stress coupled with ANSYS optimization algorithm was used to develop stress-optimized Ti-TiN multilayer coatings. Thickness of individual layer was optimized for the coating configuration comprising of six-layer while taking into account the thermal as well as thickness dependent intrinsic residual stresses.

Multilayer coatings corresponding to those of FEM stress-optimization were experimentally produced in comparison with bilayer using magnetron sputtering physical vapour deposition system. The nanoindentation hardness and elastic modulus of multilayer coatings in comparison with bilayer was investigated for the assessment of deterioration in stiffness taken place by the incorporation of Ti (titanium) interlayers. Further, investigations of the stress-optimized multilayer configurations were performed for the influence on in-plane residual stress and practical scratch-adhesion. Analytical description of the failure mode under scratch adhesion testing was demonstrated for an accurate measurement of practical adhesion of coatings to the stainless steel

substrate. Finally, the scratch adhesion, nanoindentation and experimental in-plane residual stresses results clearly demonstrated the significance of preliminary stress-optimization measures for the development of Ti-TiN multilayer wear-resistance coating systems.

The dissertation consists of six chapters. Chapter 1 is about the introduction in which Gap of knowledge, significance of the investigation and objective, approach and scope of investigation is described. Chapter 2 presents a literature review on the evolution of residual stress in magnetron sputtering PVD-coating and their influence on failures in coating. The multilayer approach to control the residual stress and procedure adopted so far for the stress-optimization of multilayer coating architecture. Chapter 3 is about the basic details about the modelling activities used in the present studies to design stress-optimized multilayer coating configuration and in Chapter 4, experimental and characterization techniques are described in details.

Chapter 5 summarizes the modelling and experimental results in three sections. In the first section results of finite element based design of stress-optimized Ti-TiN multilayer coating is summarized. In the second section, influence of Ti-TiN multilayer coating design on the mechanical properties and practical scratch adhesion are described in detail. The third section is about the influence of coating design on the in-plane residual stress. Finally, the thesis is summarized in Chapter 6 with the contributions and the remaining interesting tasks.

Table of Contents

Title Page

List of Figures

List of Tables

Acknowledgements

I have no words to express my deepest sense of gratitude to Almighty Allah, the Most Merciful and the Beneficent, Who bestowed upon me the courage, health and will to complete this project, and contribute a little to the field of knowledge and science.

First, and the foremost, I would like to thank my supervisor, Prof. Edoardo Bemporad, for his valuable guidance and facilitation throughout the research and in the preparation of this thesis. My sincere thanks to Dr. Marco Sebastiani for his constant guidance and encouragement for the completion of this research work. I would like to express my thanks to the University of "Roma Tre" Engineering Doctorate School for the financial support, including the scholarship during my studies and grateful acknowledgement for the additional funding in response of work for the "Istress" project. Dr. Marco Sebastiani deserves special thanks for the additional funding.

I would like to extend particular thanks to Marco Renzelli, Dr. M. Zeeshan Mughal and Dr. Antonio Cusma for their suggestions throughout the research period and writing of this dissertation. I would like to thank for the cooperation of current and past members of the Materials Science and Technology Group (STM), including, Andrea D'Abronzo, Fabrizia Vallerani, Federico Massimo, Giuditta Montesanti, Dr. Mattia Piccoli, Dr. M.Boota, Dr. Luca Mazzola and Dragana Nikolic. Many thanks to Daniele de Felicis, Riccardo Moscatelli and Vincehzo Mangione for their technical help, they taught me all about Scanning Electron Microscope, Nanoindenter, Optical profilometer and Dr. Marco Sebastiani, who taught me the Modelling skills and how to write the science. I deeply acknowledge my uncle Prof. Abdul Ghafoor for perpetual encouragement, moral support and technical as well as refining the language of this thesis.

I have no words to thank the Administration, especially Prof. F. Ahmad Khalid (Ex. Pro-reactor academic), Prof. J. Ahmad Chattha (Pro-reactor academic) and Dr. Fida Mohammad (Dean FMSE), of the GIK, Topi, Pakistan for encouraging and granting me leave for Ph.D. studies at University of Roma Tre, Rome, Italy.

I would like to thank my parents for their continued support and congregations for my success. I am deeply indebted to my wife Mrs. Nusrat Parveen for continuous encouragement for higher studies; my son M.Umar Sindhu and daughter Tahreem Rashid for patiently and sometimes eagerly kept waiting for completion of my studies and return to Pakistan.

Chapter 1 INTRODUCTION

1.1 Significance of the Investigation

Thin film technology is growing field as the number of its application is increasing day by day with the advancement and miniaturization. In industrial applications, the effective way of protecting and increasing the life-time of engineering components operating in corrosive, erosive, high temperature and under heavy contact load is to apply thin hard coating layer. Hard coatings are a class of coatings that have been developed as a surface engineering enhancement solution for cutting tools, dies, drills, moulds and other tribological applications. Today, almost every tool or tribological component is coated which decrease the production cost and perform well. All of these applications are based on the fact that coatings are hard, abrasive resistant, provide low friction surfaces and well-adhered to the material to be protected.

During the past few years, scientific research has been focused on multilayer coatings, which may be very effective for increasing overall coating thickness, improving hardness, adhesion, fracture toughness and controlling the residual stresses. To effectively design a multilayer system for a specific application, it is important to know the mechanical, tribological and structure properties of the coating materials. Hardness of material to be coated, number of coating layers, individual layer thickness and coating production parameters are additional design variables. Of course, the required properties are changed with the change of these properties and variables. If not all, a few basic properties of the coated system such as hardness, residual stress and adhesion have primary importance; which are also relevant and common to a wide range of applications. Among them, residual stress state could significantly alter the overall performance, life-time and is essential to control so that coated system could withstand the additional in-service loading stresses without failure.

In view of this, the objective of this PhD thesis was to develop NOVEL DESIGN RULES for the modelling and production of multi-layered coated systems with improved adhesion and optimal

surface hardness and wear resistance.

1.2 Gap of Knowledge

Hard-coatings failures on relatively compliant substrate in many tribological situations are caused by delamination of coating from the substrate (adhesive failure) and fracture in coating, i.e. cohesive failure [1, 2]. The failures are sometimes related with relatively high compressive residual stress and stress gradient through coating thickness. An increase in thickness of metallic layer could provide a reduction of in-plane stress but could significantly decrease the performance of the multilayer coating system [3]. Alternatively, multilayer configuration having equal thickness of ceramic layers could have different amount of residual stress. In case of comparatively thick titanium nitride (TiN) ceramic layer near to the substrate results in a large in-plane residual stress (dense columnar growth at the start is present), which usually causes the system's failure due to crack propagation [4]. Therefore, a specific thickness of Ti interlayer is required for a particular TiN coating thickness. The optimum coating layer thickness could further enhance the performance of multilayer in terms of adhesion and toughness. Nonetheless, most of the studies focused on the development and characterization of multilayer coatings and only a few on the multilayer coating architecture design [5]. As a result, further development seems imperative in the design of stress-optimized multilayer physical vapour deposition (PVD) coatings.

The starting point for the present work was the previous work by Bemporad et.al. [5] in which they investigated the effect of a titanium buffer layer position on the decrease of interfacial stress that improved the adhesion of TiN based systems by Finite Element Modelling (FEM) and micro-mechanical testing. A four-layer Ti-TiN multilayer coating was numerically analyzed and experimentally tested. In their work, only three Ti-TiN multilayer (four layers) configurations were simulated. They demonstrated that having a lower position of the Ti buffer layer improved the adhesion of coating to the substrate. However, a fully automated procedure to find the optimal position of the Ti buffer layer still has to be developed. In addition, the analysis and optimization of systems with the inter-position of the two (or more) Ti layers has not been investigated, yet. In the

2

present work, finite element Modelling of residual stress analysis coupled with the ANSYS optimization algorithm was used to design and develop a stress-optimized Ti-TiN multilayer configuration comprising of 6-layers.

1.3 Objective, Approach and Scope of Investigation

The objective of this thesis is the finite element Modelling based design of Ti-TiN multilayer coating system to find optimal thickness of each layer that decrease interfacial stresses responsible for delamination failure in coating. As interface delamination is one of the major failure modes of hard coatings on stiff and compliant substrate.

Such an approach could be used to develop stress-optimized multilayer coatings with minimal experimental work and help save resources during trial and error efforts. The developed optimization procedure can be used to design interfacial stress-optimized multilayer coating comprising of many layers to meet a variety of functional requirements. Further, at multilayer coating production scale, such optimization tool could be more refined to be implemented for particular multilayer (metallic/ceramic) coated systems. In addition, the finite element Modelling based measures are important to consider the coating at the preliminary component design stage instead of using as finishing operation. In general, the main aim of this work was to develop knowledge-based design tool for the multilayer coating architecture optimization considering microstructure-related functional properties of thin films such as residual stress, elastic modulus, hardness, toughness and wear resistance.

1.4 Thesis Overview

The thesis has been organized into six chapters. Chapter 2 presents a literature review on the evolution of residual stress in magnetron sputtering PVD-coating and their influence on failures in coating. The multilayer approach to control the residual stress and procedure adopted so far for the stress-optimization of multilayer coating architecture. Chapter 3 is about the details of the

Modelling activities used to design stress-optimized multilayer coating configuration and in Chapter 4, experimental techniques used in the present thesis are described in details.

Chapter 5 summarizes the modelling and experimental results in three sections. In the first section results of finite element based design of stress-optimized Ti-TiN multilayer coating is summarized. In the second section, influence of Ti-TiN multilayer coating design on the mechanical properties and practical scratch adhesion are described in detail. The third section is about the influence of coating design on the in-plane residual stress. Finally, the thesis is summarized in Chapter 6 with the contributions and the remaining interesting tasks.

Chapter 2 LITERATURE REVIEW

2.1 Introduction

Residual stress in PVD-coating is a function of film thickness, elastic modulus of coating material, morphology and film density. Sometimes, stress level could be equal to yield strength of the material for example in case of high elastic modulus materials such as tungsten, metal nitride and metal oxide. For low-modulus material such as gold, silver and titanium, yielding will relive the stresses before to develop high stress level [6]. In addition, similar to elastic modulus residual stress is also structure dependent property. Considering this structure behaviour of residual stress, microstructure and intrinsic stress evolution in thin films are first reviewed in this chapter. Then residual stress related failures in thin films are elaborated followed by multilayer coating practices to control the residual stress and related failures. Finally, the Modelling and optimization approaches to control the residual stresses in multilayer coatings are described.

2.2 Microstructure Evolution in PVD-Coatings

The microstructure of thin film could substantially influence the functional properties such as mechanical, optical and electrical. Microstructure to a larger extent is determined by the grain size, morphology and grain boundary morphology. The important characteristic of coating production through deposition is the microstructure modification for the enhancement in mechanical properties in comparison with bulk counterpart material [7]. For example, Ti thin films has elastic modulus equivalent to the bulk Ti but has enhanced plastic properties. The nature of high plastic behaviour was found to be dependent upon film thickness. As with the thickness in sub-micron range, the typical finer grain size present in metal film. Also, the evaluation technique used for the determination of plastic properties could caused large strain gradients which usually lead to geometrically necessary dislocations for the enhanced plastic properties [8]. Therefore,

understanding the process behind the microstructure evolution is imperative, especially for the development of coatings used in mechanical applications.

The evolution of thin film microstructure during growth is highly dependent on the deposition conditions. This has lead to the development of the structure zone model (SZM) for the provision of an overview of the relationship between microstructure of coatings and common deposition parameters. The first such model was presented by Movchan and Demchisin [9] through which influence of deposition temperature on the microstructure was assessed as a function of homologous temperature or deposition temperature normalized to the melting temperature of the deposited material (T_{dep} /T_{melt}). This model was ten year work of Movchan-Demchishin in which thick and thin coatings of Ti, Ni, W, ZrO_2, Al_2O_3 were deposited with electron beam evapouration on substrate over which temperature gradients were maintained. According to this model, coatings are characterized with zone 1, zone 2 and zone 3 (Fig. 2.1a).

(a)   **(b)**
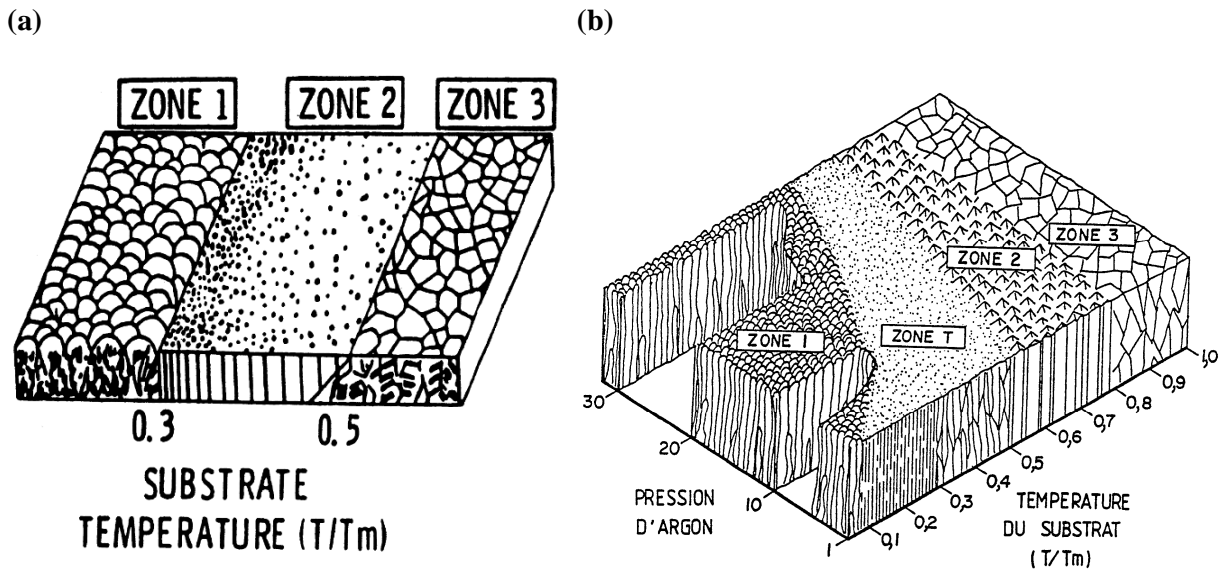
Fig. 2.1 Structural zone model for growth in metal films: (a) Model of Movchan-Demchishin [9]; (b) Model proposed by Thornton [10].

The zone 1 in the structure zone model (Fig. 2.1a) corresponds to low temperature at which ad-atom diffusion is small which results in grains with domed tops, high density of lattice imperfections and

6

porous (voided) grain boundaries; hence the term 'porous columnar' is used to describe this type of structure. At significantly higher deposition temperature ad-atom diffusion/mobility becomes significant and zone 2 structure evolves with large columnar grains and dense grain boundaries. At temperature close to melting temperature (T_{dep} /T_{melt} > 0.8), the film consists of large equiaxed grains comparable to film thickness due to both the surface and bulk diffusion of ad-atom (zone 3). However, the microstructure of metallic film deposited with sputtering depends on transfer of energy from energetic particle to the growing films. Considering this fact, Thornton [10] added an additional axis in the model to account for the sputtering gas pressure (Fig.2.1b). According to Thornton model, zone 1 structure is promoted with substrate roughness, low temperature and high argon pressure. At low temperature atoms have extremely low mobility on the surface; they tend to stick where these land on the substrate. It could persist even at higher temperatures due to substrate roughness and is promoted even on smooth substrate with high inert gas pressure. A fourth zone consisting of a dense array of poorly defined fibrous grains identified between zones 1 and zone 2 and is termed as zone T. The zone T is believed to be a transition zone. The zone T structure is formed by either thermally inducing greater ad-atom mobility or by ion bombardment. Momentum exchange then causes the coating atom to fill the boundaries of loosely packed zone 1 column.

Further, Messier [11] have found that bias potential on the substrate induce ad-atom mobility which appears to be mostly affecting the physical structure rather than pressure induced bombardment by ad-atom mobility. Therefore, the pressure axis in Thornton's model is replaced by floating bias potential of the substrate to account for the separate contribution of bombardment to ad-atom mobility. The purpose to apply the bias on substrate is also to increase the total energy arriving at the substrate, so Musil et al. [12] have suggested the replacement of bias voltage with an energy parameter, E_p. Later the energy parameter E_p has been replaced with universal parameter ion-to-atom arrival ratio.

The latest and recently proposed universal structure zone diagram (SZD) is by Anders [13], who still considered it originally the three structure zone and a transition zone (Fig. 2.2). There, film growth is classified according to thermal activation, T^*, which includes homologous temperature plus temperature shift caused by the potential energy of particles arriving at the film surface and kinetic activation E^*, describing displacement and heating effects caused by kinetic energy of bombarding particles. A third axis considers the net film thickness t^*, which provides to maintain the qualitative illustration of film structure while indicating thickness reduction by densification and sputtering. The diagram also includes a "negative thickness" due to the effect of ion etching at excessive ion energies and intensities.
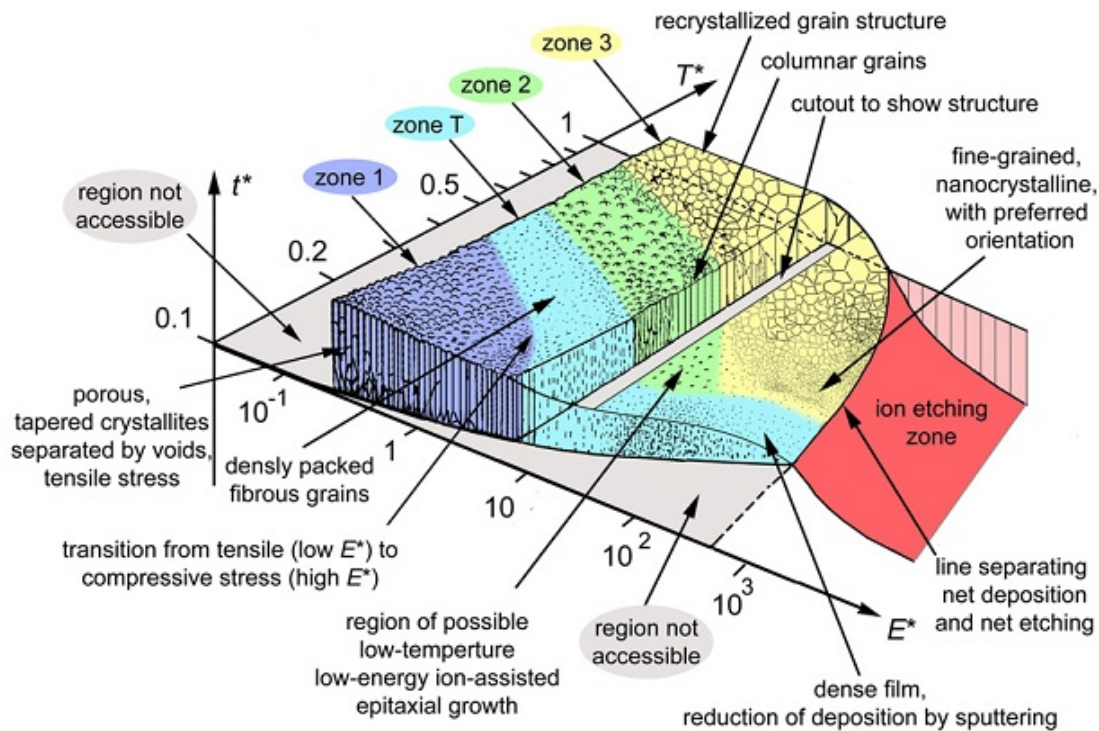
Fig. 2.2 Structure zone diagram applicable to energetic deposition

2.3 Residual Stress Evolution in PVD-Coatings

The general state of stress depends on deposition conditions as well as on structure, morphology and thickness of coatings. The stress evolution in hard transition metal nitrite coating is important to understand the origin of intrinsic stress and to control the stress level in order to avoid residual

stress related failures. It could help to engineer the coating system with required level of residual stress.

In general, coating with zone T (transition region) could result in high intrinsic stress due to dense fiber structure with smooth and highly reflective surface. The zone1 structure is too porous to support intrinsic stress. Recovery and recrystallization limits the intrinsic stress in zone 2 and 3. Daniel et.al [14] and all the references therein, analyzed the origin of intrinsic stress in magnetron-sputtered thin films with zone T-structures. The evolution of the average stress with the film thickening is schematically shown in Fig 2.3. At the early film growth (region-I), compressive stress is caused by the isolated crystallite islands prior to coalescence. The development of compressive stress only proceeds until the island establishes large area across the growth surface. The interaction forces acting across voids between adjacent islands to force them to come in contact and interact within the elastic distortion from the original position. This interaction generally results in energy gain originating from the decrease in surface area through formation of grain boundary out of the free surfaces of two adjacent islands. Formation of a continuous layer by closing all the gaps between adjacent islands is then accompanied by a film volume decrease that induces development of tensile stress (region-II). It is named as shrinkage stress (σ_{sh}) originating from volume shrinkage accompanied with grain growth (Fig. 2.3b). The maximum tensile stress indicates the end of coalescence process, although its magnitude depends on the grain boundary motion and the number of voids annihilated between the grains during coalescence. Surface ad-atom mobility also contributes to the stress development and it determines whether the tensile stress decrease in the magnitude or become compressive with increasing film thickness. That is, only under high mobility diffusion condition in which excess sputtered adatom to the grain boundaries occurs that give rise to compressive stress (region-III). This is named as ion-peening stress (σ_{ip}) component (Fig. 2.3b). The mechanism for the incorporation of surface adatom into grain boundaries decrease their free energy that is more likely at higher substrate temperature or under ion irradiation. However, grain boundaries are microstructure and thickness dependent. From this, continuous

increase in grain size is observed as the layer thickens under continuous flux of sputtered material. The grain growth proceeds with the annihilation of grain boundaries which subsequently leads to a decrease in the total area of grain boundary surface and thus to decrease of the number of ad-atom incorporated there. In addition, diffusion flux towards grain boundary area is suppressed with the existing compressive stress which increases chemical potential of atoms in the grain boundaries. Both of these effects contribute to decrease the compressive stress component (region-IV). It is stress component (σ_{diff}) due to ad-atom diffusion to the grain boundaries (Fig. 2.3b). The evolution of low-density atomic structure along grain boundaries evolves during grain growth into a dense well-organized grain structure; the subsequent volume shrinkage is accompanied by the development of tensile stress (region-V).
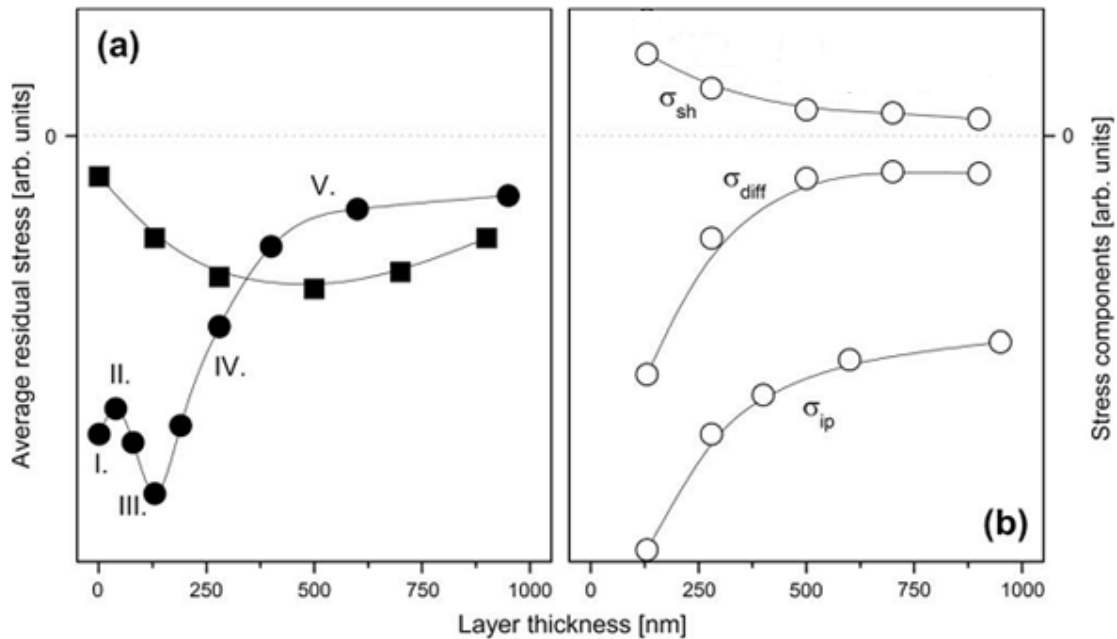
Fig. 2.3 Schematic diagram for the development of residual stress in zone-T structure: (a) Average stress in zone-T layers having various structures (full circle: single CrN layer with V-shaped morphology; full square: CrN top layer with equi-axed columnar structure); (b) The growth stress component [σsh, σdiff and σip originating from volume shrinkage during grain growth, ad-atom diffusion to grain boundaries and ion-peening under conditions of high kinetic energy, respectively]. Source [14]

The intrinsic stress is changed dramatically with film thickening and it is due to microstructure

evolution through sequence of growth stages; including nucleation, island growth, coalescence of islands formation of continuous structure and subsequent film growth. Every growth stage is essentially characteristic of unique film forming processes that give rise to generation of growth (intrinsic) stress which differs in magnitude and can be either tensile or compressive.

2.4 Residual Stress Related Failures in Coatings

Residual stresses are commonly present in coatings irrespective of deposition techniques. Overall performance of coatings is closely related to the process induced residual stress. For instance, compressive stress is often desirable as many coating materials (brittle) are stronger in compression than tension. It also increases the hardness of coating but excessive stress can decrease the adhesion of coating to the substrate. Hard coating failures on relatively compliant substrate are caused by delamination of coating from the substrate (adhesive failure) and fracture in coating, i.e cohesive failure [1]. The failures are primarily related with relatively high compressive residual stress and stress gradient in the coatings.

In principle, the interior of ceramic films have equi-biaxial in-plane compressive residual stress which could cause delamination at edges which is schematically shown in Fig. 2.4a.
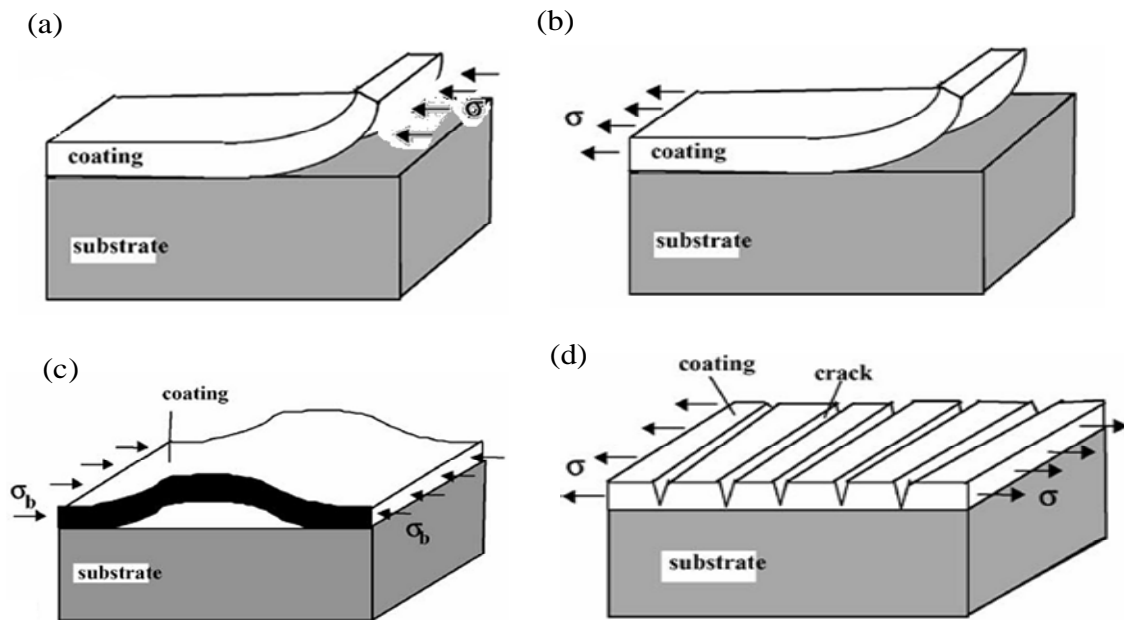
Fig. 2.4 Schematic of residual stress related failure mode in coatings: (a) Edge delamination (high in-plane stress and weak interface), (b) Delamination under high tensile stress with weak interface, (c) Buckling under in-plane stress, and (d) Bridge cracking, i.e. coating under tensile stress having strong interface, Source: [15]

The residual stress level is characteristic of a specific material combination (coating and substrate) and manufacturing process. Fig. 2.4 shows failure mode in coating under different state of stress. It is seen that in-plane tensile stress in coating cause delamination and fracture within coating (Fig. 2.4b and Fig. 2.4d).

In general, three possible failure mechanisms in coating under tensile residual stress can occur [16]. For example, a brittle coatings fracture by development of cracks through coating thickness (Fig. 2.4d). Tougher coating may fail by delamination along the interface (Fig. 2.4b) or by propagation of crack in the substrate. However, residual compressive stresses could cause edge delamination, buckling and prompt crack initiation and propagation within the coating. It is seen that failure modes are also affected by the relative strength of coating-substrate interface.

In addition, it is well-established that ceramic coated circular disk-shaped metal components mainly fail by the magnitude of axial stress at or near the radial free edge of the specimen. The associated failure of de-cohesion at metal-ceramic interface resulted in progressive delamination and spallation of coatings. Analytical and finite element models as well as experimental studies showed the influence of these stress components on coating failures. Also, when coating is applied on engineering components with geometrical features like edges, corners, notches and relatively rough surfaces generate interfacial stresses. It is also named as lift-off stress. The lift-off stress magnitude is further increased with tribological service loadings. The stress level could exceed up to 50 % of residual stress [17]. Fig. 2.5 schematically shows some of stress concentrations arise with unfavourable geometry and high in-plane stress whilst Fig. 2.6 shows actual (real-time) failure mode examples.
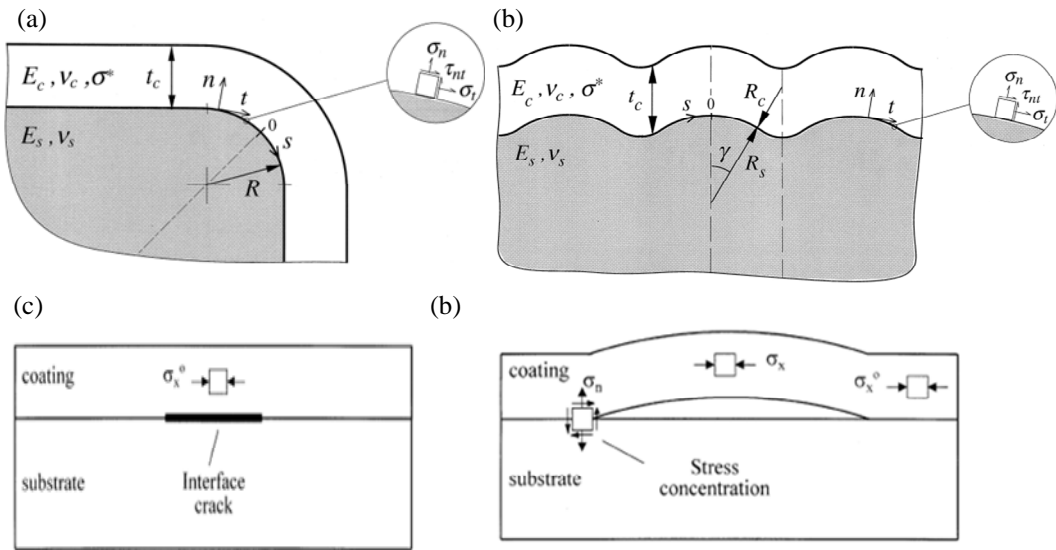
Fig. 2.5 High in-plane stress in combination with unfavourable geometry: (a) Coating on smooth 90° substrate edge, (b) A periodically rough substrate surface, (c) High in-plane stress in attached configuration, and (d) Stress re-distribution as a result of delamination.
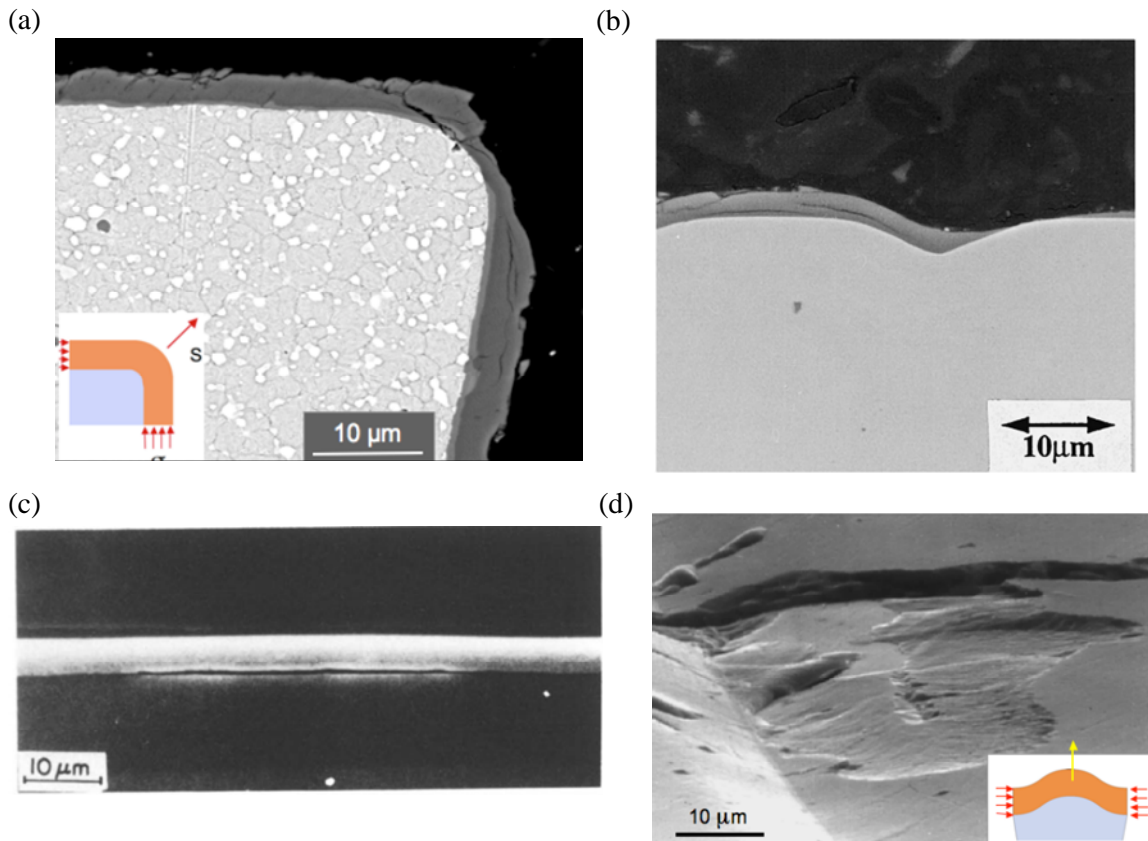
Fig. 2.6 High in-plane stress in combination with unfavorable geometry: (a) A partially detached TiAlN coating at edge of cutting tool [18], (b) Cross-section indicating the initiation of fracture at

small convex curvatures, i.e. substrate roughness effect, (c) Delaminated layer of ZnO on Si [19]. (d) The PVD TiB_2 with $\approx$ 10 GPa compressive stress on austenitic stainless steel [17].

In all the cases mentioned above, the residual stress deviates from perfect bi-axial stress state. As a result interfacial normal and shear stresses are generated which are exaggerated with 2-D plane stress element in Fig. 2.5a. Under this stress orientation, maximum principal stress is suspected to cause the initiation of cohesive fracture (Fig. 2.6a). However, the interface has lower strength generally than either of coating or the substrate. To avoid possible coating delamination, therefore interfacial (across interface and shear stress along the interface) residual stress analyses are usually performed under such situations.

2.5 Multilayer Coatings

Multilayer coating is a class of hard layer material in which individual layers of different materials are produced. Individual layer thickness can vary from micro-scale to nano-scale as long as individual layer maintain its properties. The materials properties vary differently; in order to have a coating-substrate system for a specific application, only a few material combinations could results in required level of performance. The important material parameters to be considered in achieving better performance are elastic modulus, coefficient of thermal expansion, morphology of coating and chemical compatibility of the coating and substrate [20, 21].

The mechanical and tribological behaviour of brittle coatings on compliant substrate materials is usually very much influenced by the in-service loading conditions and residuals stresses. To meet the specific functional requirements for various uses, multilayers in comparison with bi-layer, offer much more ease: to control residual stresses, improve adhesion, increase overall thickness, improve abrasive wear, producing the toughening response and adopted for multi-functional use. This has lead to increasing use of multilayer coatings. Multilayer coatings not only offer a combination of properties from different materials but also increase the overall performance of systems.

To show a real-time example of multilayer coating system, a commercially available multilayer coating system developed by Aesculap® for the artificial knees implant (Fig. 2.7) [22]. The coating system comprised of seven layers in which external layer of ZrN has exceptional hardness and CrN layer provide the hardness gradient through coating thickness and prevent allergy. The coating system has excellent performance in terms of adhesion, wear and materials fatigue. In view of structure-property relation, multilayer system in comparison with bilayer has refined grains that increase the performance of the coating system; however bilayer has coarse grains of open columnar structure close to surface.
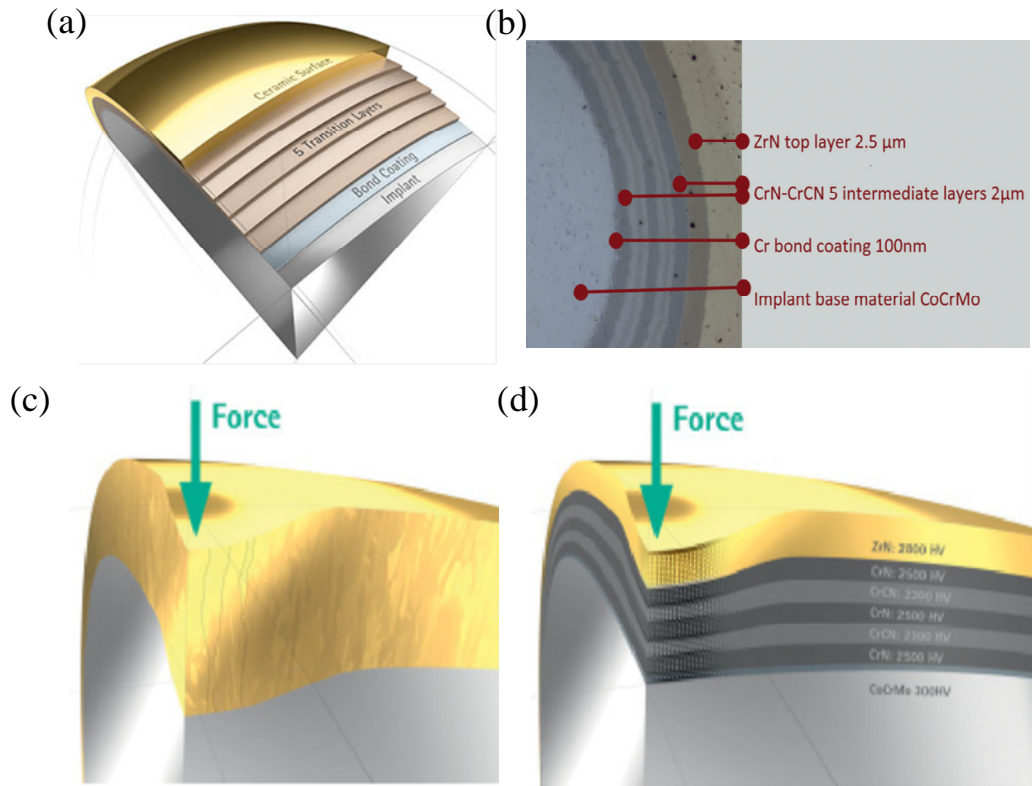
Fig. 2.7 Multilayer coating system in comparison with bilayer used for artificial knees: (a) Enlarged image at a point on artificial knees, (b) Cross-sectional view showing individual layer thickness, (c) Monolayer system grain morphology, (d) Multilayer structure showing hardness gradient.

It is clear from the above-mentioned literature that even though multilayer coatings offer promising solutions for wear resistance applications, the demand of different applications can be met by

adjusting relative thickness of different layers. For instance, Ma et al. [23] emphasized the need for the optimization of Ti-layer thickness for greater coating adhesion in Ti-TiN multilayer coatings.

2.6 Finite Element Modelling of Residual Stress in Coatings

Coatings systems enhance the performance and increase the lifetime for a wide variety of engineering components. Engineering design approach is commonly used for the design of component before manufacturing for specific functional use. However, coating of component is simply performed as a finishing operation. To obtain a full benefit of multilayer coating it could be considered at the component design stage. For this analytical and FEM optimization measures are therefore required. General design rules need to be found for performance optimization.

Modelling of materials behaviour is common practice in graded materials fabricated at relatively high temperature depending upon their composition to produce composite structure for better properties [24, 25]. Although, the continuum approach is at much larger scale in comparison with micro-structural features but the materials simulated behaviour could be very useful for further refinement and improvement.

Finite element analyses of thermal stresses in Ti-TiN bi-layer verified via analytical calculation is extensively researched. The results suggest that inter-layer decrease the interfacial stresses that improve coating substrate adhesion [26, 27].

2.7 Optimization of Multilayer Coating Architecture

Multilayer coating system with alternate hard and soft layers play a major role for the better performance in tribological and wear applications over mono-layer coatings. ***However, the role of overall thickness, number of layers and individual layer thickness cannot be overlooked and need to be optimized.*** To effectively design a coating architecture for a specific application and depending upon design constraint of the component, it is necessary to know the state of stress in coatings. For this, measures in terms of stress-optimization seem imperative.

Lakkaraju et al. [28] optimized chromium-chromium nitride (Cr-CrN) multilayer coating architecture comprising of eight layers on steel and aluminium substrate subjected to Hertzian contact. The overall coating thickness was fixed to 2 µm and the thickness of Cr and CrN were chosen as design variables. Multi-objective optimization was used to minimize the von-Mises stress in the topmost CrN layer and strain discontinuity in the coating thickness direction along the Cr-substrate interface. The approach in the study provides an important and promising direction for the design of wear-resistant multilayers coating to minimize coating damage under given set of loading conditions. However, the choice of objective function to be minimized, von-Mises stress and strain discontinuity, may not be appropriate to address the damage in the coating. The brittle behaviour of thin CrN layer perhaps required a maximum principal stress type function. Also strain discontinuity seems to be vague parameter to quantify delamination of the coating. A stress-based approach better reflect damage at interfaces.

To address the residual stress related failure in PVD-coatings, a mathematical model of stress analysis was proposed by Lyubimov et.al [29]. The model calculates residual stress as a function of coating layer thickness, deposition temperature, composition and substrate bias voltage. The model addresses the interfacial failure and suggests the use of compliant metal layer to decrease the stress. However, the model involved time-consuming mathematical calculations.

In a study on various design of metal-ceramic (Ti-TiAlN) multilayers deposited onto substrate pre-treated with different plasma-sputtered etching conditions [30]. The different multilayer designs were investigated for their influence on the level of residual stress and mechanical properties. It was found that multilayer with thick ceramic layer has lower compressive stress in ceramic layer. However, multilayer with decreasing ceramic layer thickness in graded fashion towards substrate has higher compressive stress.

The above referred investigations help conclude that multilayer coating offers promising solution to control the residual stress and improve adhesion. ***In the present work,*** finite element Modelling of residual stress analysis coupled with the ANSYS optimization algorithm, as a robust measure was

use to design and develop Ti-TiN stress-optimized multilayer coating comprising of 6-layres. During the optimization, a realistic bi-axial thickness dependent intrinsic stress (ion peening stress) in each TiN layer was reproduced as an initial in-plane stress. The thickness dependent intrinsic stress for numerical calculations was adopted from the growth-stress model for columnar structures proposed by Daniel. et.al. [14].

Chapter 3 MODELLING ACTIVITIES

In this chapter, details about the formulation of Finite Element Model (FEM) for the analyses and optimization of residual stresses in multilayer coatings are provided. The numerical optimization algorithm used and mesh refinement measures are elaborated. In addition to FEM Modelling, the use of analytical Modelling for the analytical description of failures (adhesive and cohesive) during the coating adhesion evaluation is described.

3.1 Residual Stresses in Coatings

A complete state of stress in the PVD-coatings is important for their mechanical performance. Intrinsic stresses in coating itself not leaving the substrate unstressed and could be added to the ones originating from other source such as external loading and temperature etc. Usually, the intrinsic stresses in coating are much smaller than their yield strength otherwise coating will not form at all. High compressive intrinsic stress could cause plastic deformation in the substrate, coating delamination from the substrate. The actual stress during the service is given by Eq. 3.1:

$$\sigma = \sigma_{res} + \sigma_{app} \qquad\qquad 3.1$$

Where σ_{app} is the external force including the frictional heating during service. General classification of stress in coating is shown in Fig. 3.1.

```
                    ┌─────────────────────┐
                    │ Thin coating stresses│
                    └─────────────────────┘
           ┌────────────────────┐        ┌──────────────────┐
           │ Internal/Residual stress│    │ External stress  │
           └────────────────────┘        └──────────────────┘
                                              ── Service loading
                                              ── Geometric constraints
   ┌────────────────────┐   ┌──────────────────────┐
   │ Intrinsic/Growth stress│ │ Extrinsic/Thermal stress│
   └────────────────────┘   └──────────────────────┘
      ── Recrystallization process    ── Difference in thermal expansion of
      ── Grain growth                    coatings and substrate
      ── Phase transformation
      ── Variations of interatomic spacing with the crystal size
      ── Microscopic voids and arrangement of dislocations
```

Fig. 3.1 Classification of stresses in coatings

Residual intrinsic stresses in the PVD-coatings mainly arise from contribution and interactions of two sources: the low thermal stresses and the high intrinsic stresses. Thermal stresses arise from thermal mismatch between the coating and the substrate: during final cooling from deposition to room temperature. It effects become exaggerated when multiple layers of materials have different thickness and big difference in stiffness [31]. A thermal mismatch-strain, ε_{th} , arises by change in temperature; result in residual stress given by the following Eq. 3.2 [32]:

$$\sigma_{th} = \left(\frac{E_f}{1-v_f}\right).\varepsilon_{th} = \left(\frac{E_f}{1-v_f}\right).\left(\alpha_s - \alpha_f\right).(T_r - T_D) \qquad 3.2$$

Where E_f and v_f are Young's modulus and Poisson's ratio of the film; $(\frac{E_f}{1-v_f})$ = bi-axial elastic modulus of the film; α_f and α_s are thermal expansion coefficients of the film and the substrate, respectively; $T_{sub\{r\}}$; $T_{sub\{D\}}$ are the room and deposition temperatures of the substrate, respectively. The quantity σ_{th} is the stress that will develop in the thin film. Here, only differential thermal stress is considered; however thermal expansion is structure dependent property which could vary with the layer thickness.

The intrinsic stresses in PVD-coatings arise during deposition and its magnitude depends on deposition conditions, such as reference potential on the substrate, pressure of the working gas and the target to the substrate distance, as well as on stoichiometry and thickness of coating-layer [33-35]. Usually, the resulting residual stress field is formed by a simple superposition of the two sources (Eq. 3.3):

$$\sigma_{res} = \sigma_i + \sigma_{th} \qquad\qquad 3.3$$

In addition, intrinsic stresses in the PVD-coatings are thickness-dependent although the stress gradient through coating thickness is common.

3.2 Finite Element Analysis of the Residual Stress

In general, analytical procedures have been developed to evaluate the average in-plane thermal stresses in bi-layer and multilayer coating-substrate systems based on linear-elastic calculations and uniform temperature [36, 37]. However, it is difficult to carry out stress analyses analytically for multi-layered coating systems and numerical methods, therefore, are followed. Also, for more detailed stress analyses, 2-D or 3-D numerical method such as FEM has been successfully developed. The FEM application could overcome the difficulties mostly associated with laborious solution of analytical equations and can be easily used to simulate stress distribution for the temperature gradient.

Finite element models have been successfully used to investigate the influence of inter-layer on the thermal stress in coatings [27, 38]. The thermal stress is effectively decreased with combination of coating and substrate material properties, interlayer material, coating thickness and interlayer material thickness. Stress concentration with abrupt change in materials behaviour at coating-substrate interface can cause propagation of cracks parallel to interface and therefore, could cause coating delamination.

 Thus FEM can be considered as an efficient tool to simulate the residual stress problem in multilayer coating system because of its robustness and ease in solving problems with complex geometries including material nonlinearity as well as formulations of different types of problems. In

the present work, FEM Modelling is used to design stress-optimized Ti-TiN multilayer coatings with optimal coating layer thickness. For this, finite element package ANSYS coupled with optimization module was used. Finite element models developed so far for stress analyses did not take into account the intrinsic residual stress. To fill this gap, thickness dependent intrinsic stresses were considered in model.

3.3 Finite Element Modelling Consideration

3.3.1 Materials properties

The structure dependent materials properties such as elastic modulus, thermal expansion coefficient and materials behaviour are shown in Table 3.1[27, 39]. Material properties were assumed as temperature independent and residual thermal stresses were computed for simulated cooling from uniform deposition temperature (250 °C) as stress-free temperature to room temperature (25 °C) of the substrate. Deposition temperature was sufficiently low to ignore thermal diffusion effects. Plastic hardening behaviour of substrate, an ideal elasto-plastic behaviour of Ti metallic layer equivalent to bulk Ti and TiN layer was considered as purely elastic for its brittle nature [39, 40]. The materials behaviour is shown in the form of stress strain curve in Fig. 3.2a. In addition to material thermal response, materials thickness dependent intrinsic stresses were considered in the Modelling. A realistic bi-axial thickness dependent intrinsic stress (ion peening stress) in each TiN layer was reproduced as an initial in-plane stress using the INISTATE command in ANSYS. The thickness dependent intrinsic stress for numerical calculations was adopted from the growth-stress model for columnar structures (Fig. 3.2b) [14].

Table 3.1 Physical and thermal properties of inter-layer, coatings and substrate materials

Materials	Elastic Modulus (GPa)	Poisson's Ratio	Thermal Expansion (10^{-6} °C^{-1})	Materials Behaviour
Ti	116	0.32	9.0	Ideal Elastic Plastic
TiN	600	0.25	9.4	Perfectly Elastic
Substrate	200	0.30	13.0	Plastic Hardening
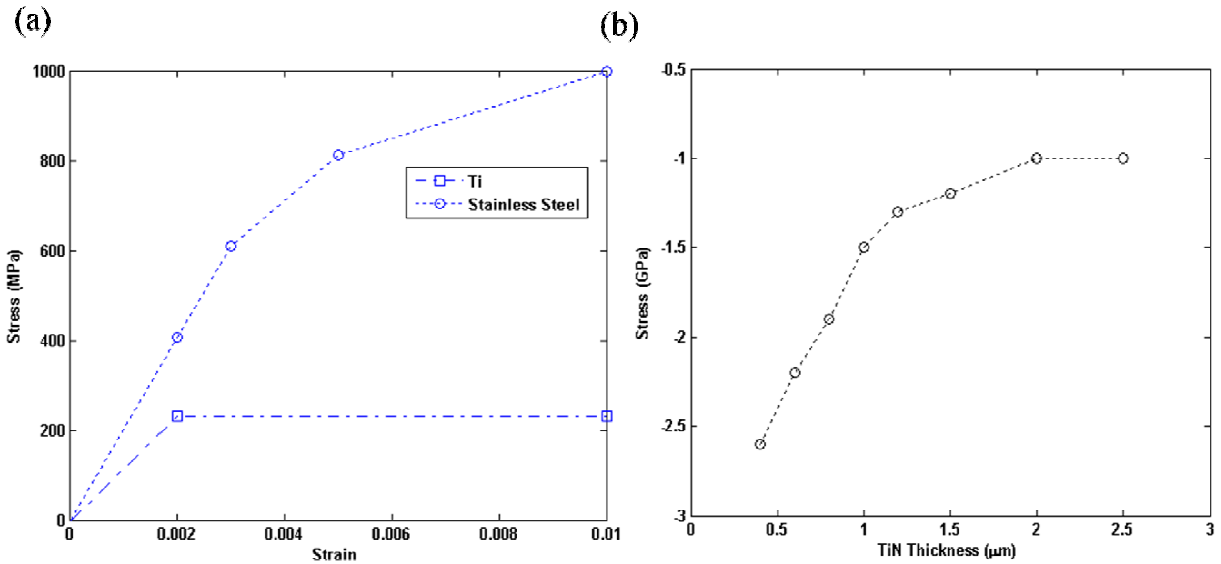
Fig. 3.2 (a) Materials behaviour in terms of stress-strain curve, and (b) Thickness dependent intrinsic stress reproduced in TiN.

3.3.2 Description of model

For the Modelling of residual stress under the influence of thermal and intrinsic stresses generated in TiN and Ti coatings deposited with magnetron sputtering, a 2D axi-symmetric stainless steel model of 600 μm diameter and 300 μm thickness was formulated in ANSYS multi-physics with Parametric Design Language (APDL). Model is built in parametric form to enable changing these parameters during optimization. The APDL model consists of a circular disk-shape, which exactly reproduces the actual sample shape and has significant dimension in comparison with coating

23

thickness considered in this study. In addition, the model dimension throughout the numerical calculations remained same for the qualitative comparison of results. Following were the simplifying assumptions in this model:

i. The interfaces (coating/substrate, multilayer) were assumed to be perfectly bonded. In finite element, terminology, the nodes are shared at all the interfaces.

ii. Coating and substrate materials were assumed as homogeneous isotropic and linear thermo-elastic.

iii. The structure dependent materials properties were also assumed as thickness independent.

iv. Equal bi-axial intrinsic stress in x and z-directions was reproduced in all the TiN layers.

v. Residual thermal stresses were computed for simulated cooling from an assumed deposition temperature (300 ℃) as stress-free temperature to room temperature (25 ℃) of the substrate. This is maximum temperature that can be developed in the PVD coating system used in the present study.

Two models were formulated one of Ti-TiN bi-layer and other Ti-TiN multilayer with middle position of interlayer. The two models developed are described as follows (thickness of layers is always starting from top layer):

i. Model type of bi-layer "BL" (single layer of 2.55 μm thickness and Ti inter-layer of 0.05 μm thickness);

ii. Model type multilayer with middle position of Ti inter-layer "MMPI" (three TiN layers each of 0.80 μm thickness and three inter-layer of Ti each of 0.06 μm thickness).

A schematic description of both the models is shown in Fig. 3.3.
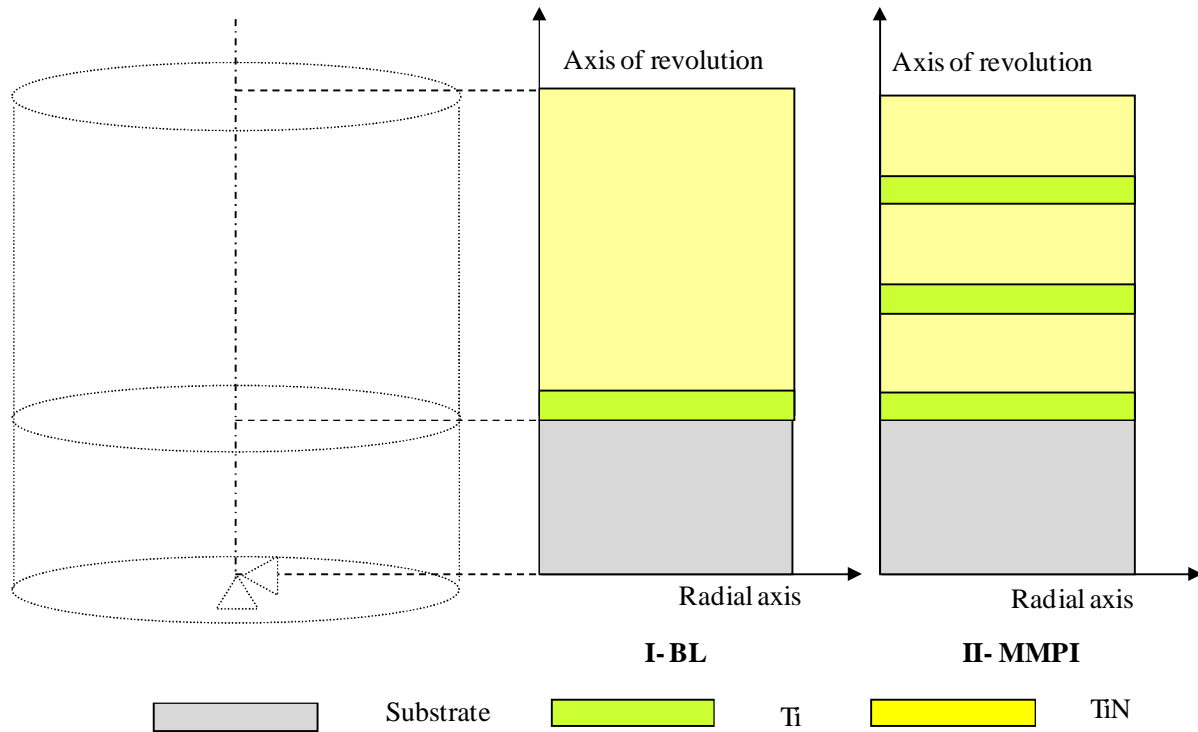
Fig. 3.3 Schematic description of finite element model (not to scale) realized to evaluate residual stress arising from deposition process.

3.3.3 Description of element

Materials behaviour was simulated with axi-symmetric thermal element PLANE77. The element was 2-D thermal element, eight nodes (quadrilateral form) or six nodes (triangular form) and only has temperature degree of freedom at each node. For a coupled thermal-structural analysis, the element was automatically replaced with an equivalent structural element PLANE183. The structural element was eight nodes (quadrilateral format) or six nodes (triangular format) and has two degree of freedom at each node: translation in x and y directions. This element has material plasticity, elasto-plastic, stress stiffening and initial stress supporting capabilities. These elements were also used during the FEA optimization. The geometry of an element (Fig. 3.4) has quadrilateral or triangular areas and nodes are indicated by dots except for element midside node that acted as connector between the two or more elements. All the elements that shared a node had the same displacement components at that node.
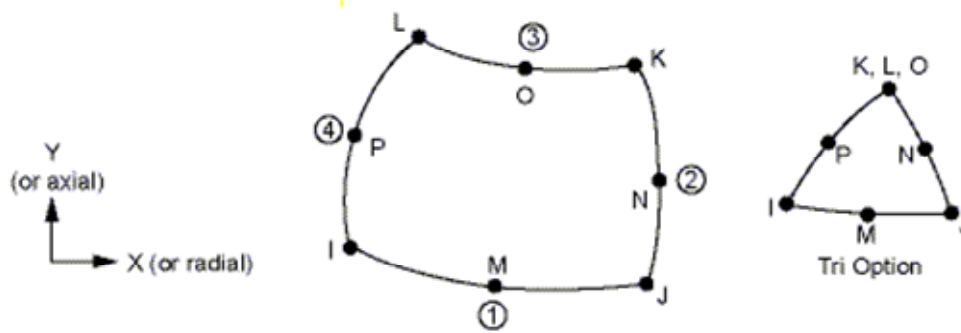
Fig. 3.4 Geometry of an element

3.3.4 Meshing and validation of numerical model

The previously described, quadrilateral shaped element was used to mesh the model. A finer mesh size was introduced into the model along the thickness of coating in a graded fashion (biasing element size) in order to minimize element size both from the coating and substrate sides towards the coating-substrate interface and other interfaces, in case of multilayer coating. The interfaces were expected to be sharp with high stress concentration as the PVD magnetron sputtering was low temperature process without significant diffusion between the layers. A finer mesh was also introduced close to edge in a graded fashion across the thickness of the coating and substrate. While in lower part of the substrate, an increasingly coarse mesh was used in order to decrease the computational time.

In addition, for the refinement of mesh in multilayer coating configurations, numerical model was validated through numerical tests under different material properties and dimension values of the coating and substrate. A change in thermal residual stress with a change in thickness was also verified with analytical solution [41]. This was accomplished by the reduction in bending induced stress with an increase in layer thickness. This effect was significant for the axial stress; however, for the in-plane stress, it was less significant. The thickness of the each layer was simulated with sufficient number of elements (number of elements in thickness direction) to have stress distribution within each layer. In addition, the bottom left corner of axi-symmetric model was fixed for bending

to occur during cooling that changed the residual stress with a change in thickness of the coating layer during the optimization. These boundary condition does not relieve the in-plane intrinsic stress which was reproduced in each layer during optimization. The analysis was first performed to assess the independent effect of thermal stress and validate the in-plane stress with analytical calculation. Elastic theoretical calculation were performed to calculate the average stress using analytical relation given in Eq. 3.4 and 3.5 [36].

$$\sigma_c = E_c \ (\varepsilon_0 - \alpha_c \Delta T) \qquad\qquad 3.4$$

Where,

$$\varepsilon_0 = \frac{E_c \ (\alpha_c - \alpha_m) \ \Delta T \ t_c)}{E_m t_m + E_c t_c} \qquad\qquad 3.5$$

Then combined effects of thermal and intrinsic stresses on axial stress profile were examined.

3.4 Finite Element Optimization of Residual Stress in Multilayer Coating

For the residual stress optimization in multilayer coatings, the thickness of individual layers need to be optimized. For this, FEM residual stress analyses coupled with ANSYS optimization algorithm (build in) was used to develop stress-optimized Ti-TiN multilayer coatings.

3.4.1 Single-objective optimization procedure

The goal of optimization was to determine optimum value of design variables those minimize or maximize the objective functions. If the objective is to find a maximum of the function "f", it will be minimization of function – f. Optimization algorithm contains three components: design variable (independent variables), constraints (dependent variables) and objective function (dependent variables) to be minimized. Within specified lower and upper limits of design variables and constraints, the optimization algorithm will search in design space for the minimization of objective function with analysis-evaluation-modification cycle as shown in Fig. 3.5 [42]. As per optimization cycle, an analysis of initial design is performed, results are evaluated against specific design criterion, and the design is modified accordingly.

The procedure of single-objective optimization implemented in ANSYS subproblem algorithm is described here. In mathematical form, the standard single-objective optimization statement can be defined as Eq.3.6 and 3.8:

$$\text{Minimize } f(x) = f(x_1, x_2, \ldots \ldots, x_n) \tag{3.6}$$

$$\text{Subject to } g_i(x) = g_i(x_1, x_2, \ldots \ldots, x_n) \leq 0, i = 1, \ldots, p \tag{3.7}$$

$$\text{and } h_j(x) = h_j(x_1, x_2, \ldots \ldots, x_n) = 0, \quad j = 1, \ldots, m \tag{3.8}$$

Where, f is objective function to be minimized and $x = (x_1, x_2, \ldots, x_n)$ and is design variable with lower and upper limits. While h_i and g_j are vectors of equality and inequality constraints also called linear and non-linear constraints, respectively. The limits on design variable and state variable make the optimization problem as constrained one. The sub-problem program establishes relationship between objective function and design variable by curve fitting. This is done by calculation of objective function for several sets of design variables value (i.e. performing the least squares fit between the data points of several designs). The resulting curve is called an approximation. Each optimization loop generates new set of data points, and the objective function approximation is updated. In the similar way, an approximation is generated for each of the state variable and updated at the end of each loop. Now, this approximation is minimized instead of actual objective function. In this way, optimization program converts this problem into unconstrained optimization problem by adding penalty function to the objective function to account for the imposed constraints. The penalty function method is as per Eq. 3.9 and 3.10:

$$\text{Minimize } P(x) \tag{3.9}$$

Where

$$P(x, \rho, \beta) = f(x) + \sum_{j=1}^{m} \rho h_j^2(x) + \sum_{i=1}^{p} \beta g_i^2(x) \tag{3.10}$$

Where $P(x, \rho, \beta)$ is penalized objective function and $f(x)$ is the un-penalized objective function. The penalty parameters ρ_j and β_i are computed by Eq. 3.11 and 3.12:

$$\rho \gg 0 \tag{3.11}$$

$$\beta_i = \begin{cases} 0 & if \ g_i(x) \le 0 \\ \rho \gg 0 & if \ g_i(x) > 0 \end{cases} \tag{3.12}$$

Now the problem is formulated into unconstrained optimization. The minimum of the unconstrained approximated objective function is then carried out by applying a sequential unconstrained minimization technique (SUMT). It is iterative approach that solves the problem in each of the iteration. However, by solving directly, the large values of ρ can cause instability and inefficiency when deriving solution with high accuracy. The SUMT algorithm is implemented as follows:

i.   Initialization step: Choose tolerances $\varepsilon > 0$ such that starting point $x_0 = 0$ for the initial penalty parameter $\rho = 1$.

ii.   Iterative step: Perform unconstrained optimization $P(x, \rho_k)$ to get x_k.

iii. Convergence criteria: Check the convergence criteria. If $\|x_{k-1} - x_k\| < \varepsilon$ or the difference between two successive objective functions value is smaller than ε, then stop. Otherwise, set $\rho_{k+1} = 10 \ \rho_k$, $x_0 = x_k$, and return to step (ii).

For a model with fixed number of alternating Ti-TiN layers on the stainless steel substrate, a single-objective constrained (total thickness was constrained during optimization iteration) optimization algorithm (sub-problem) was employed to find the optimal thickness of each coating layer that minimized the axial stress (perpendicular to interface) at edges.

In the present work, coating layers were used as design variables (independent variable) within constraints of total thickness (2.6 µm). The axial stress (normal to surface), which was highest at the at the model edge, was used as objective function. The optimization algorithm will search for minimum objective function within specified upper and lower limits of design and state variables. Thickness of Ti inter-layer was varied from 60 to 150 nm. Each TiN layer has initial thickness of 0.8 µm and varied from 500 nm to 1.5 µm.

During optimization, a realistic bi-axial thickness dependent intrinsic stress (ion-peeing stress) in each TiN layer was reproduced as an initial stress using the INISTATE command. It was adopted

from the growth-stress model for columnar structure [14]. The in-plane intrinsic stress (Fig. 1c) was applied on structural elements of each material and as a check, the stress in each solution was written out to a file by issuing the "inis, list" command. In addition, with the change in thickness of TiN during optimization-cycle, the corresponding value of intrinsic stress for that thickness was reproduced on structural elements and as a monitoring check, it was also written out to a file in each previous solution. All the modelling activities in the present studies were carried out on an Intel-Xeon 3 GHz processor machine with 8 GB of random access memory, running a Windows 64-bit operating system and time taken for an optimization was $\approx$ 20 min.

The Multilayer configuration (MMPI) was optimized in two ways according to the optimization frame work is shown in Fig. 3.5. In the first optimization, only the position of Ti inter-layer was changed within a fixed overall thickness of all the three TiN layers. Second optimization was performed with variable thickness of all the Ti interlayers and TiN layers.

```
                         ┌─────────────────────┐
                         │  FEA Analysis Model │
                         │       (APDL)        │
                         └─────────────────────┘

┌──────────────────────────┐    ┌─────────────────────────┐
│ Change in Thickness of   │    │ Objective Function &    │
│        Ti & TiN          │    │ Constraint Evaluation   │
└──────────────────────────┘    └─────────────────────────┘

                No                 ◇ Convergence Check ◇

                                         Yes

                         ┌────────────────────────────┐
                         │ Optimal Thickness of Ti &   │
                         │           TiN               │
                         └────────────────────────────┘
```
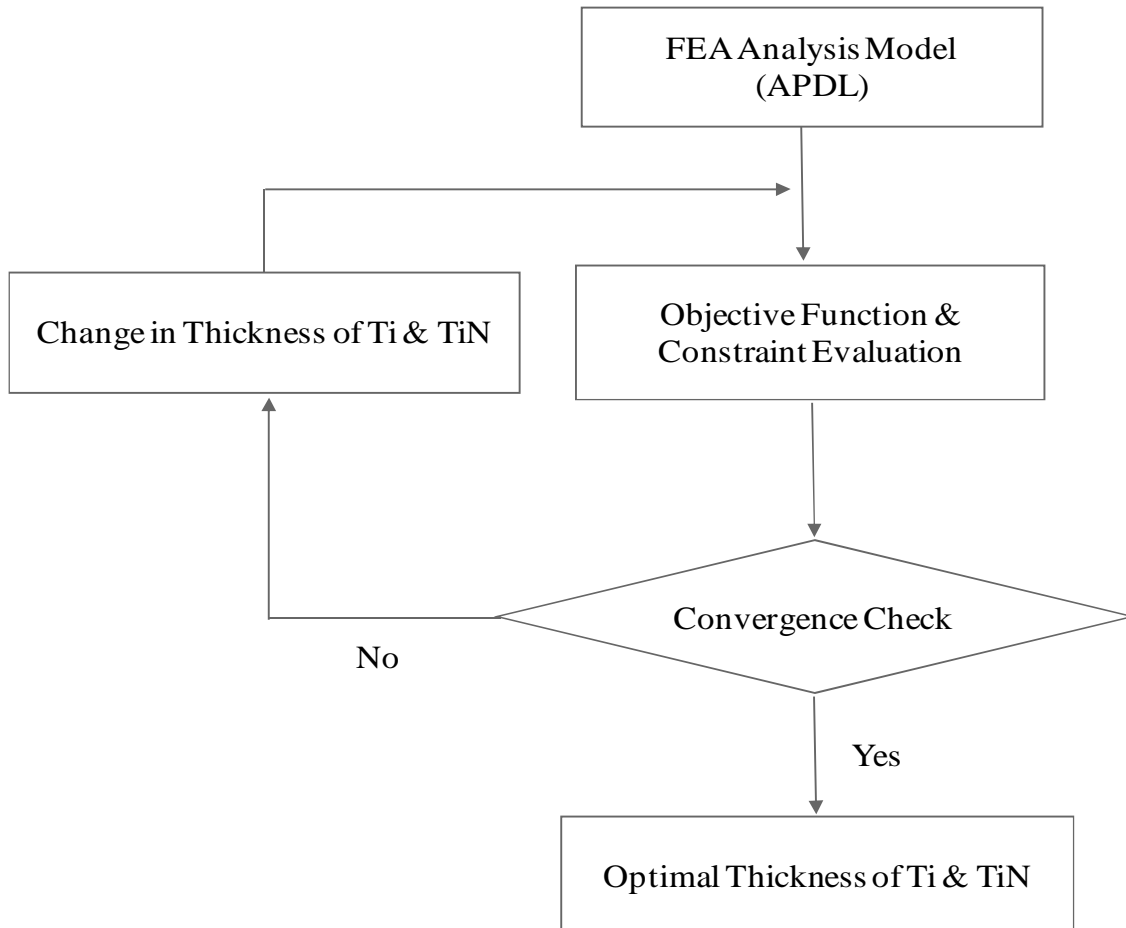
Fig. 3.5 Followed optimization frame work

This was simply done by only taking the TiN three layers as design variables and there thickness was changed during optimization cycle. During the second optimization, thickness of all the layers was changed. To facilitate reading, the two optimal models developed are described as follows:

   i.   Model type "MOPI": Multilayer with optimal position of Ti interlayers;

   ii. Model type "MOTI": Multilayer with optimal thickness of Ti interlayers.

3.4.2 Analysis through batch file

As per requirement of the optimization and reproducing the thickness-dependent intrinsic stress, ANSYS batch mode was used instead of the Graphical User Interface (GUI) mode. The batch input file for the analyses was written in APDL. The batch processing mode is highly modular as once the batch file was created, changing materials properties, dimension of model, mesh refinement, load etc. is snap. It helps to save lot of time to optimize or make several ANSYS runs without doing everything by hand. The analysis in batch mode is shown in the Appendix-A as an input file.

3.5. Analytical Modelling for Description of Adhesive and Cohesive Failures in Coatings

A physical analysis of mechanical contact in measurements, like instrument indentation, scratch and tribo-tests (wear) enables to find out why a coating system fails under certain loading conditions. The results provide indications on how the investigated coatings can be improved. Analytical Modelling of mechanical contact in coating substrate system could provide comprehensive information about specific coating property. For example, in case of coating on compliant substrate under micro scratch and indentation test only fails as a result of severe deformation in the substrate without specific coating property. Therefore, significant measurement information is essential for a sound determination of mechanical properties of the coating or the interface as well as the physical analysis of failure mechanism [43].

3.5.1 Theory of analytical Modelling method

Analytical approach based on method of image indenter and its application to mechanical contact problem in layer materials is a well-established and widely used [44-46]. A description of the procedure is illustrated in Fig. 3.7, where two-layered half space is investigated with respect to elastic field within the area $0 \leq z < h$.

(a)   (b)
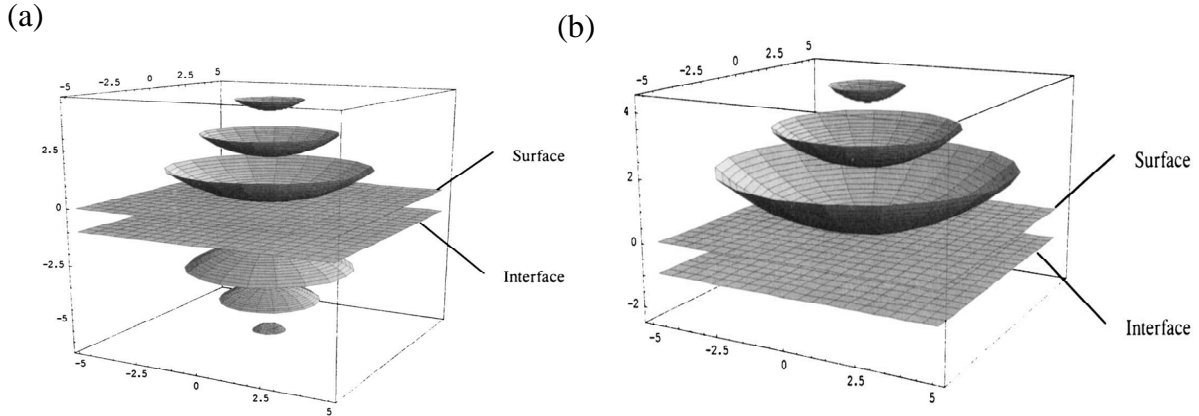
Fig. 3.6 Figurative description of the mathematical method (method of image indenters): (a) The result for the region $z < h$ ($z < 0$), i.e. the observer located within the layer, (b) For the observer within the substrate $z \geq h$ ($z < 0$) where h is thickness of coating. Source [46]

With already known homogeneous solution for the load conditions, all the interfaces and surfaces are treated as boundaries at which special conditions for the elastic field has to be satisfied. For the non-homogenous half-space (layered half space) an observer interprets the sets of additional potentials as sets of additional indenters which act from the positions $z = -2h$, $z = -4h$..., provided under the same load conditions. Alternatively, in the same manner for the homogeneous half-space (substrate half space), fictitious observer interpret the elastic field in the $z \geq h$ zone as one of the infinite space with the original contact at $z = 0$ as well as addition indenters (image contacts) at the positions $z = 2h$, $z = 4h$... and so on, in relations to added potential functions. The von-Mises stress produced in the material under the influence of both normal and shear loading was calculated using the relation in Eq. 3.13:

$$\sigma_M = \sqrt{\frac{1}{2}\left[\left(\sigma_{xx} - \sigma_{yy}\right)^2 + \left(\sigma_{zz} - \sigma_{yy}\right)^2 + \left(\sigma_{xx} - \sigma_{zz}\right)^2 + 6\left(\tau_{xy}^2 + \tau_{xz}^2 + \tau_{zy}^2\right)\right]} \qquad 3.13$$

3.5.2 Analytical Modelling for description of adhesive and cohesive failures

For practical adhesion evaluation, scratch test is commonly followed technique in which critical load acting normal to surface at incident of failure is usually related to adhesion between the coating and the substrate. However, it is strongly affected by various parameters such as scratch indenter tip radius, film thickness, friction effects, hardness and elastic modulus of coatings and substrate material, etc. In hard-coatings cohesive failures are due to an extensive deformation in the compliant substrate by high indenter tip radius during the scratch test. Indenter tip radius significantly controls the depth of deformation zone. The plastic deformation mainly starts in the substrate and does not initiate in coatings until the large plastic zone has develop at coating-substrate interface [47]. With relative increase in indenter tip radius, the critical scratch load and deformation depth within substrate is increased. As a result, sufficiently high tensile bending stresses developed in coating and being sensitive to tensile stress cohesive failure occurs. In general, high compressive shear stress at interface and tensile stress at contact edge cause delamination at interface and crack formation in brittle ceramic layer close to surface [48]. Therefore, the pre-requisite for producing adhesive failures and suppressing cohesive failures in the thin hard coatings on relatively compliant substrate is to choose proper scratch indenter tip radius.

In the present studies, first scratch test was performed with standard indenter (200 µm). However, the cohesive failure mode was found, indicating the cohesive property rather than adhesive. Then scratch test was performed with 100 µm indenter, the adhesive failures were found. Finally, the adhesive and cohesive failure modes were analytically described with analytical modelling software package (FilmDoctor®) [49]. It was found in accordance with the studies by Schwarzer et.al [43] that the position of maximum von-Mises stress (criterion related to the plastic flow of the material due to shear stress) is the controlling factor for adhesive failures. The maximum von-Mises stress

should be increase sufficiently above the critical yield strength of metallic layer at interface to ensure adhesive failure. The state of the stress was simulated with tangential frictional force of 10 % of the applied normal load (apparent friction coefficient), which roughly model the interaction between the indenter and the coating. The critical load was determined by scratch test, defined as load where delamination or crack failure appear, was used as input to analytical Modelling. The interaction was modelled with two hemi-spherical tip conical indenters of tip radii (100 and 200 µm), in order to characterize the most likely occurring cohesive and adhesive failures. The position of the von-Mises stress with respect to the coating-substrate interface and the normal stress on the surface at trailing edge of scratch indenter was qualitatively compared. The elastic modulus input data were measured with nanoindentation and interaction was modelled without an influence of the coating intrinsic stresses. The data used in analytical calculations are shown in Table 3.2.

Table 3.2 Physical properties of inter-layer, coatings and substrate materials

Material	Elastic Modulus (GPa)	Poisson's Ratio	Thickness for BL Modelling (µm)	Thickness for MMPI Modelling (µm)
Ti	116	0.32	0.05	0.05
TiN	400	0.25	2.55	0.80
Substrate	200	0.30	NA	NA

3.6. Summary

In this chapter, an overview on the use of modelling techniques in this thesis has been provided. The procedure and theoretical basis are explained. The aim of using the modelling in the present study has been explained. Please note that the procedure can be easily reproduced by any user who reads this document, for any multilayer system architecture, given the ANSYS input files that are provided as in the appendix-A. This is a key-factor for dissemination and wider use of this method.

Chapter 4 EXPERIMENTAL DETAILS

4.1 Substrate Preparation

Stainless steel substrate having thickness of 5-7 mm was cut from 25 mm diameter commercially available steel rod. The specimen grinding was accomplished with 180, 400, 600, 800 and 1200 grits silicon carbide-papers and polished with diamond suspension of 6, 3 and 1µm. In each successive grinding (lapping) stage, scratches from previous stage were removed with perpendicular orientation of the substrate with respect to the previous scratches. The switch over to fine grit paper was done when the same orientation of all the scratches like hair became visible under microscope. In addition, before moving to finer paper, samples were thoroughly washed with water followed by alcohol and then allowed to dry. With the finer grit (1200), all the scratches were removed till the sample showed a mirror finish. At this stage by seeing under the optical microscope, all the light was diffused without any reflection and the sample surface became opaque. Sample was gently held stationary with balanced force during each grinding stage to keep it completely flat as uneven surface was not suitable for scratch testing as well as XRD residual stress measurements. The other side of samples was also grinded to make sure the flatness of sample for all the designed investigations. After grinding, all the substrates were polished to mirror finish. It was performed on polishing discs with rubber pads of 6, 3 and 1µm using corresponding diamond suspension as lubricant. Finally, samples were ultrasonically pre-cleaned in acetone and isopropyl alcohol for 10 min. The roughness of sample was in the range of 25-35 nm measured with optical profilometer (Leica DCM 3D).

4.2 Physical Vapour Deposition (PVD) and Magnetron Sputtering

The PVD is a physical way of producing condensable vapour followed by deposition of thin film from those vapours. To produce vapours, a variety of physical means are used, such as simple heating of source material (thermal source), laser beam with an intense photon beam (pulsed laser

deposition) and knocking of atoms out of target with energetic ions (sputtering). The technique is performed under vacuum, evaporation under high (10^{-6} torr) to ultra-high (10^{-9} torr) and sputtering under moderate to low vacuum (10^{-4} to 10^{-1} torr) [50]. The PVD was used to deposit thin films particularly at lower temperature (200~250 °C) and possible to deposit coating on heat sensitive material without affecting their properties.

In the sputtering process, material to be coated (target) was subjected to high negative voltage. The fundamental physical embodiment (hardware) configurations of practical deposition systems in wide-spread use, with the representative operating parameter were: DC sputtering, RF (radio frequency) sputtering, and the magnetron sputtering (MS).

The schematic of DC sputter deposition with parallel-plate discharge is shown in Fig. 4.1a. Here discharge means current flowing through a low-pressure gas. Argon is the most common sputtering gas, at a pressure of the order of one torr. The power supply was simply a high-voltage DC source of supplying several kilo-Volts (kV). The sputtering target was the cathode of the discharge, tens to several hundred square centimetres; the anode may be the substrate and/or vacuum chamber walls. The cathode-anode separation was typically a few centimetres. Argon gas was transformed into positive ions under the influence of vacuum and electrical charge. These positively charged ions sputtered the material to be deposited.

The RF sputtering offers advantages over DC, for instance, lower voltage and lower sputtering gas pressure may be used with high deposition rate. Sputtering of an electrically insulating target becomes possible. Schematic of RF sputtering with a parallel plate discharge capacitive is shown in Fig. 4.1b. The power supply was a high voltage RF source (offering 0.5-1kV amplitude, ≥ 0.1 MHz frequency). A blocking capacitor (C) was placed in the circuit to develop DC self-bias, and matching network was used to optimize power transfer from RF source to the plasma. The RF source produced and maintained the plasma in the same way as DC discharge does.
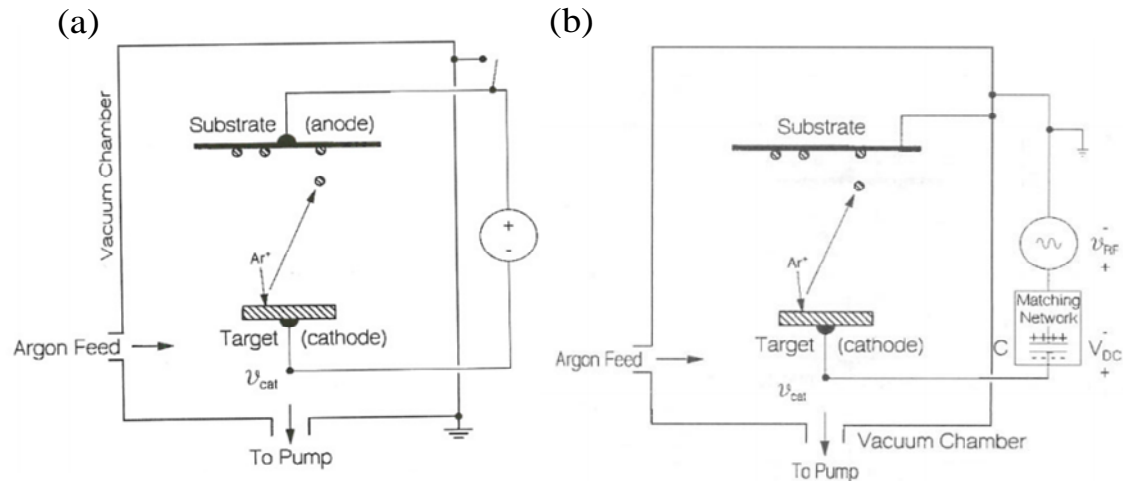
Fig. 4.1 Schematic arrangement: (a) DC sputtering, and (b) RF sputtering

In magnetron sputtering (MS) permanent magnets are placed behind the target that forms a magnetic field in front of the target. The permanent magnet creates lines of magnetic flux those are perpendicular to the electric field (as in DC sputtering there is electric field perpendicular to the target surface) and parallel to the target surface. It confines the free electrons (secondary electrons) close to the target that increase the local gas ionization for the provision of more efficient and high sputtering rate. The schematic of MS is shown in Fig. 1.2a along with magnetron sputtering facility used in the thesis work.
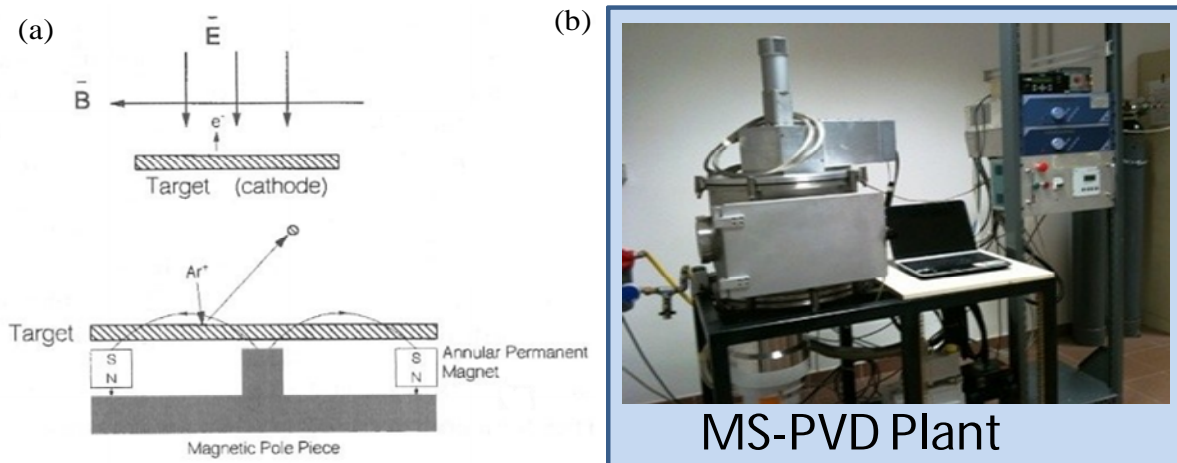
Fig. 4.2 The magnetron sputtering arrangement and sputtering plant: (a) Planar and annular magnetron sputtering arrangement, (b) Photograph of magnetron sputtering deposition facility.

4.3 Preparation of Magnetron Sputtering Ti-TiN Multilayer Coatings

The multilayer coatings of the Ti-TiN in the present work were produced using in-house developed balanced-magnetron sputtering plant, with DC powered Ti target and RF powered sample holder capable of inducing bias to the substrate. Nitrogen was put into chamber to produce TiN by reactive sputtering. The chamber was pumped down to a base pressure of 6×10^{-6} mbar and each TiN layer was deposited with 120 and 14 sccm respective flows of argon and nitrogen. Samples were ultrasonically pre-cleaned in acetone and isopropyl alcohol for 10 min and mounted on a sample holder that was fixed at 110 mm distance from the target. The substrates were subsequently sputter-etched in argon plasma for 10 min in order to remove the surface oxide layer. The deposition rate of Ti and TiN measured with FIB was $\approx$ 1 and 35 nm/min, respectively. The differentiation of each layer thickness was achieved by choosing the deposition time. All the TiN layers were coated with an applied potential of 150 V while all the Ti layers were coated with floating potential (around 30 V from plasma). The temperature developed during deposition and ion-etching was measured with a temperature measurement strip gauge. The gauges were mounted on the rod which held the sample on other side. At the end of deposition the temperature was 290 °C. The images of samples produced were shown in the Table. 4.1.

Table 4.1 Images of produced samples

| BL | MMPI | MOPI | MOTI |
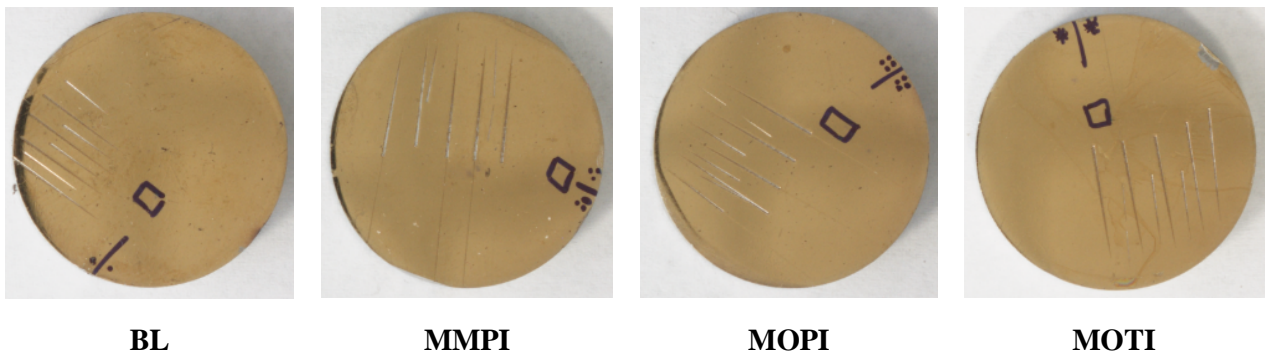
4.4 Focused Ion Beam for Thickness Evaluation

A focused ion beam (FIB) system is an instrument used extensively in the semiconductor and materials science fields for site-specific micro-machining, analyses and for deposition. A FIB

column resembles that of a scanning electron microscope (SEM) but is equipped with electrostatic lenses rather than electromagnetic lenses. Most commercially available FIB systems use a focused beam of gallium ions (Ga$^+$) from a liquid metal ion source (LMIS) to perform micro-machining tasks [51]. Gallium is commonly used because it has a low melting point (29.8 $^\circ$C). Minimal heating is required to melt gallium to wet the tungsten needle at the LMIS. The minimal heating requirement reduces any reaction between the gallium and the tungsten needle. The low instability and low vapour pressure of viscous liquid gallium contributes to source stability.

A FIB system looks and operates very much the same as a scanning electron microscope (SEM), the only difference is that Ga+ ions are used as an alternative to electrons. Just like in SEM, the intensity of the secondary electrons produced at each raster position of the beam are displayed to create an image of the sample. Since ions are heavier than electrons and can strike with greater energy, these result in sputtering of neutral and ionized substrate atoms (milling). During this process, chemical interaction also occurs, like breaking of chemical bonds, dissociation of molecules. Hence this phenomenon can be exploited during the deposition process. Fig. 4.3. summarized all the three processes.
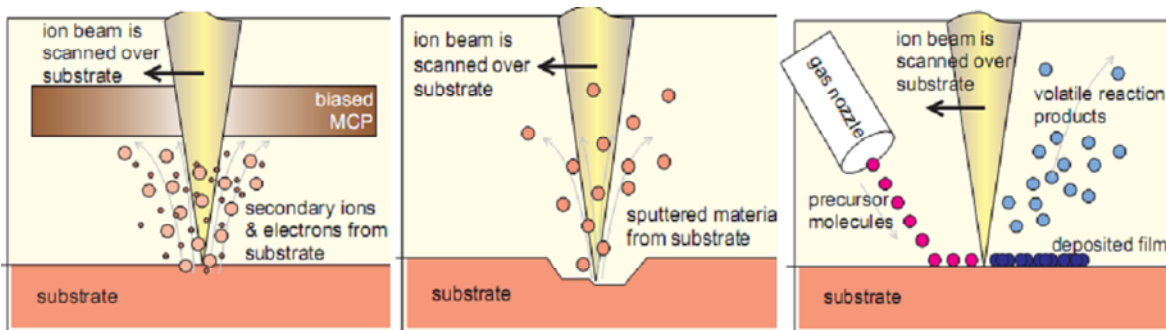
Fig. 4.3 The FIB principle, from left to right: Imaging, Milling and Deposition. Source [52]

One of the most common applications of the multi-beam instrument is the cross sectional imaging of samples. The sample is tilted towards the FIB column such that the ions beam is normally incident on the sample surface. An area is milled out, normally 20-30 µm in width and 10-15µm in length. A Ga$^+$ high ion beam current (greater than 1nA) is used to rapidly mill the area to a depth of

5-10 µm and then a finer beam with the smaller current (< 500pA) is used to polish one face of the cross section. The polished face can then be imaged directly with the SEM. If the surface layer is of particular interest (as in the present studies) then the gas injection system is used to deposit a thick layer (0.5 ~ 1 µm) of Pt, C or W to act as a sacrificial layer to protect the sample surface. Fig. 4.4a shows a FIB cross section of a titanium nitride (TiN) coating along with the sacrificial Pt layer, while Fig. 4.4b shows the cross section of a multilayered coating highlighting not only the multilayers but also the bond layers. The FIB cross sectioning in the present studies was carried out with the FEI Helios NanoLab 600 system. A FIB current of 21 nA was used for milling the trench while 2.8 nA and 0.92 nA were used for rough and fine polishing, respectively.
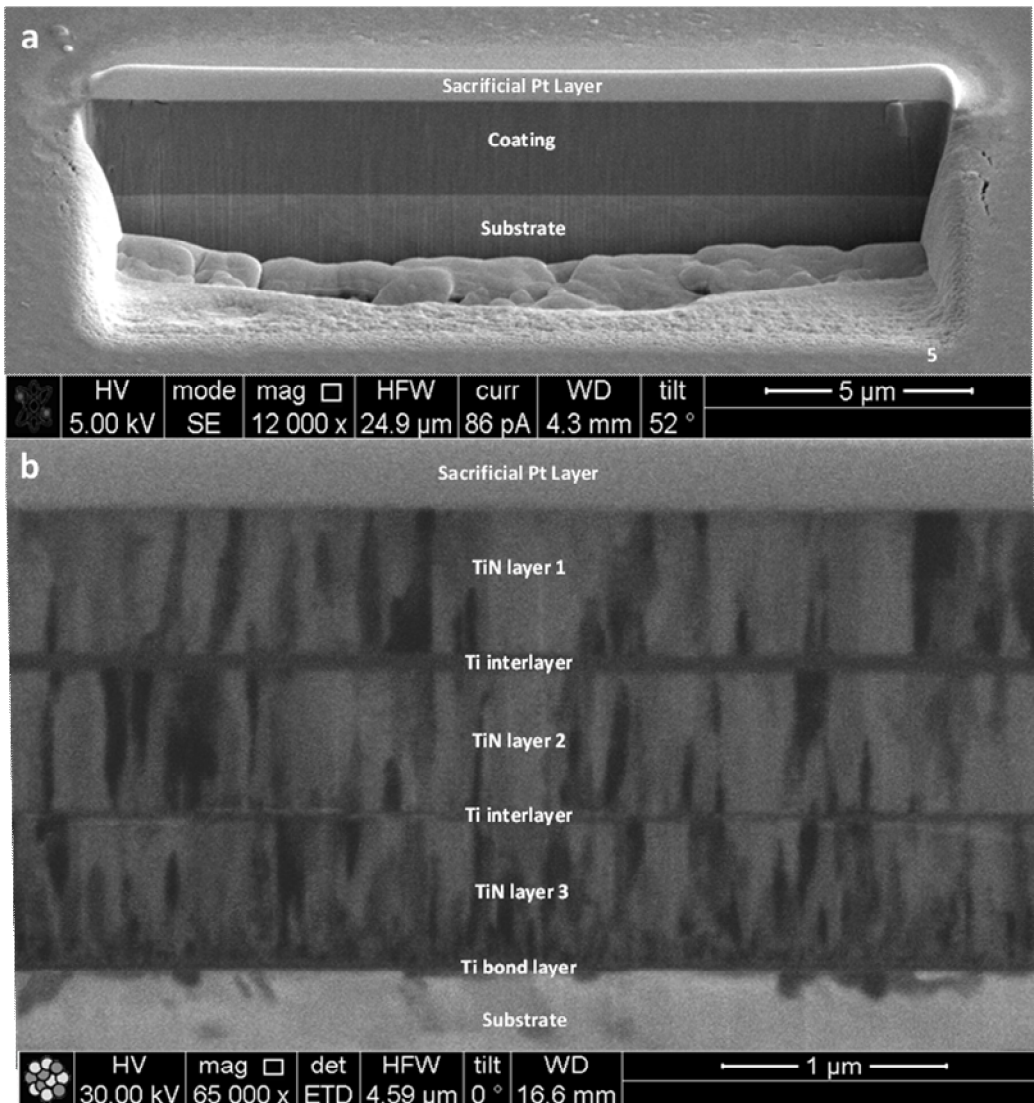
Fig. 4.4 The FIB cross section: (a) Single layer, (b) Multilayer TiN coating showing the sacrificial layer, interlayer and bond layer.

4.5 Nanoindentation Testing

Nanoindentation testing, also known as instrument indentation test (IIT) involves pressing a hard indenter (diamond of known geometry) into test material and continuously-recording the resulting load versus displacement data [53-55]. The ultra-low-load (1nN) can be applied and displacement of 0.1 nm can be measured. An instrument indentation provides the acquisition and continuous control in feedback during the applied load and indentation depth, by using load cell and displacement sensor which varies according to type of instrument. The resulting load-displacement response of material is analyzed using the realistic physical models for hardness and elastic modulus calculations.

In the Agilent Nanoindenter G200, the force is applied by means of magnetic coil through varying the intensity of the circulating current. The displacement measured with a capacitive sensor consisting of three plates: One connected to indenter and other two are fixed. By varying the displacement, capacitance is measured with in nominal resolution of 0.01nm. The vertical movement (only one degree of freedom) of the indenter is guaranteed by a system of springs (Fig. 4.5b) which ensure very high transverse stiffness (maintaining a low vertical stiffness).

(a)   (b)
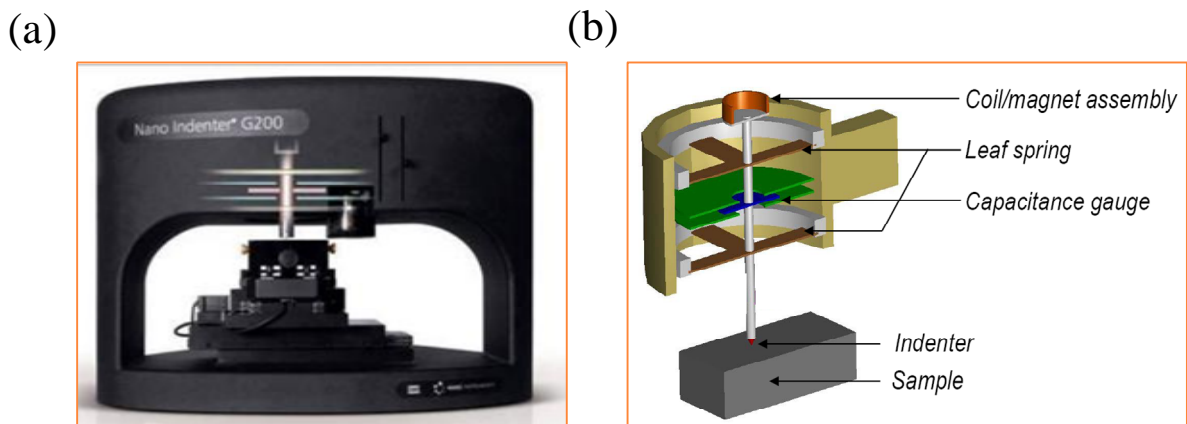
Fig. 4.5 Nanoindentation equipment: (a) Nano Indenter G200, (b) Schematic representation.

The typical outcome of instrument indentation test is represented with *P-h* curve, as an example, a typical data set with the Berkovich indenter (three-sided pyramid) is presented in Fig. 4.6. The curve is mainly characterized by loading and unloading portion. Loading portion shows elastic-plastic response of material and its shape is dependent on load and geometry of indenter. However, the unloading curve is completely different. Initial stage of unloading curve shows elastic recovery in the material.
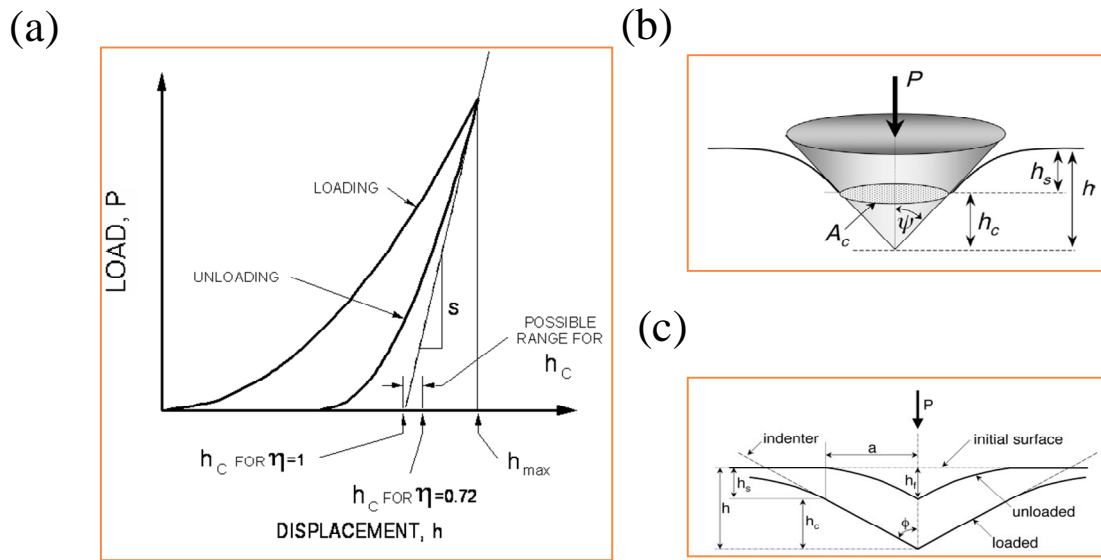
Fig. 4.6 Schematic description: (a) Schematic description of load (P) versus displacement into material (h) curve with basic parameters, (b) Schematic of contact geometry under action of load P; plastic deformation within area of contact and elastic deflection (sink-in) to the edge of contact area, (c) Contact geometry for a load P (loaded) and following the removal of indenter (unloaded).

The two most important mechanical properties, hardness (H) and modulus (E) are frequently measured using the classical Oliver-Pharr [56, 57] procedure. The procedure is based on the analysis of generic P-h curve from a test performed with instrumented indentation without the requirement of testing parameters. The procedure is based on some fundamental materials assumption: The test material is homogenous and isotropic, and the materials behaviour is independent of the strain rate and creep phenomena. The analyses involve the calculations of three important parameters from the P-h curves namely; maximum load, P_{max}, maximum displacement

into surface, h_{max}, and the elastic unloading stiffness, $S = dP/dh$, defined as the slope of upper portion of unloading curve (also called contact stiffness). The hardness and elastic modulus are uniquely derived from these parameters.

The stiffness of contact is the rate of change in load with depth which is measure of elastic modulus E of the material. The elastic modulus (reduced modulus, which describes the elastic contact between the sample and the indenter) is simply determined by measuring the contact stiffness and area of contact, made at the time of initiation of the unloading (Fig. 4.6c), through the following analytical relation derived from the solution of Sneddon for the elastic contact between a cone and a plane surface:

$$E_r = \frac{1}{\beta} \frac{\sqrt{\pi}}{2} \frac{S}{\sqrt{A_{proj}}} \qquad 4.1$$

Eq. (4.1) is derived from theory of elastic contact [58] and is valid for all types of indenter described as smooth function of a solid of revolution. Since this equation is derived for an axisymmetric indenter, it formally applied only to circular contacts. However, the correction factor β is then introduced to take into account of the geometry which is not axisymmetric as commonly used indenter (Vickers, Berkovich). In experimental practice (Oliver-Pharr), the contact stiffness S is calculated by interpolation of a portion (typically 50%) of the unloading by an equation of the type:

$$P = \alpha \left(h - h_f \right)^m \qquad 4.2$$

Where α and m are the interpolation parameters (h_f is the final sink-in). The contact stiffness S is calculated analytically by differentiating Eq. (4.2) and calculating the value for $h = h_{max}$ i.e:

$$S = \left[\frac{dP}{dh} \right]_{h = h_{max}} = \alpha \cdot m \left(h_{max} - h_f \right)^{m-1} \qquad 4.3$$

The next step in the procedure is to determine the contact sink-in h_c, which is in accordance with the assumptions of the method (Fig. 4c), is expected to be always lower than the total depth of penetration h_{max}.

The sink-in of contact is calculated as:

$$h_c = h - \varepsilon \frac{P}{S} \qquad\qquad 4.4$$

Where ε is constant which depends on the geometry of the indenter. Analytical solutions of elastic contact mechanics predict that for spherical indenters $\varepsilon = 0.75$ and $h_c/h = 0.5$ and $\varepsilon = 0.72$ and for conical indenters $hc/h = 2/\pi$. Finite element analysis [55] have shown that Eq. (4.4) functions optimally for a contact-type elastic-plastic using $\varepsilon = 0.75$.

The contact area A_{proj} is calculated (eq. 4.1) in a continuous manner as a function of the indentation depth h_c:

$$A_{proj} = \sum_{i}^{8} C_n (h_c)^{2-n} = C_0 h_c^2 + C_1 h_c + C_2 h_c^{\frac{1}{2}} + C_3 h_c^{\frac{1}{4}} + \cdots + C_8 h_c^{\frac{1}{128}} \qquad\qquad 4.5$$

$$A_{proj} = f(h_c) \qquad\qquad 4.6$$

Where the area function represents the characteristic section of the indenter as a function of sinking-in of the contact; this function is calculated using calibration standard sample of amorphous silica (SiO_2) with known elastic properties and is essential for precise description of the indenter geometry. Where C_0 ... C_8 are constants determined by the procedure of the measurement curve. The number of terms are chosen according to good fit over the entire range of depth and determined by comparing the log-log plot of the data fit. This type of relationship allows to easily describing a large number of geometries relevant from the practical point of view. The perfect pyramid or cone is represented only by the first term C_0, while the second term describes a paraboloid of revolution, approximated to a sphere for small depths of penetration. A perfect sphere of radius R is instead described by the first two terms with $C_0 = C_1 = - \pi$ and $2\pi R$.

Finally, once the projected area of contact and stiffness of contact is known, the hardness and elastic modulus are determined by using the fundamental analytical relations as follows:

$$H = \frac{P_{max}}{A_{proj}} \qquad\qquad 4.7$$

Where P is load and A is the area of contact at that load, and elastic modulus from Eq. (4.1)

The entire procedure (Oliver-Pharr) for the extrapolation of the basic properties of a nanoindentation test is summarized schematically in Fig. 4.7.
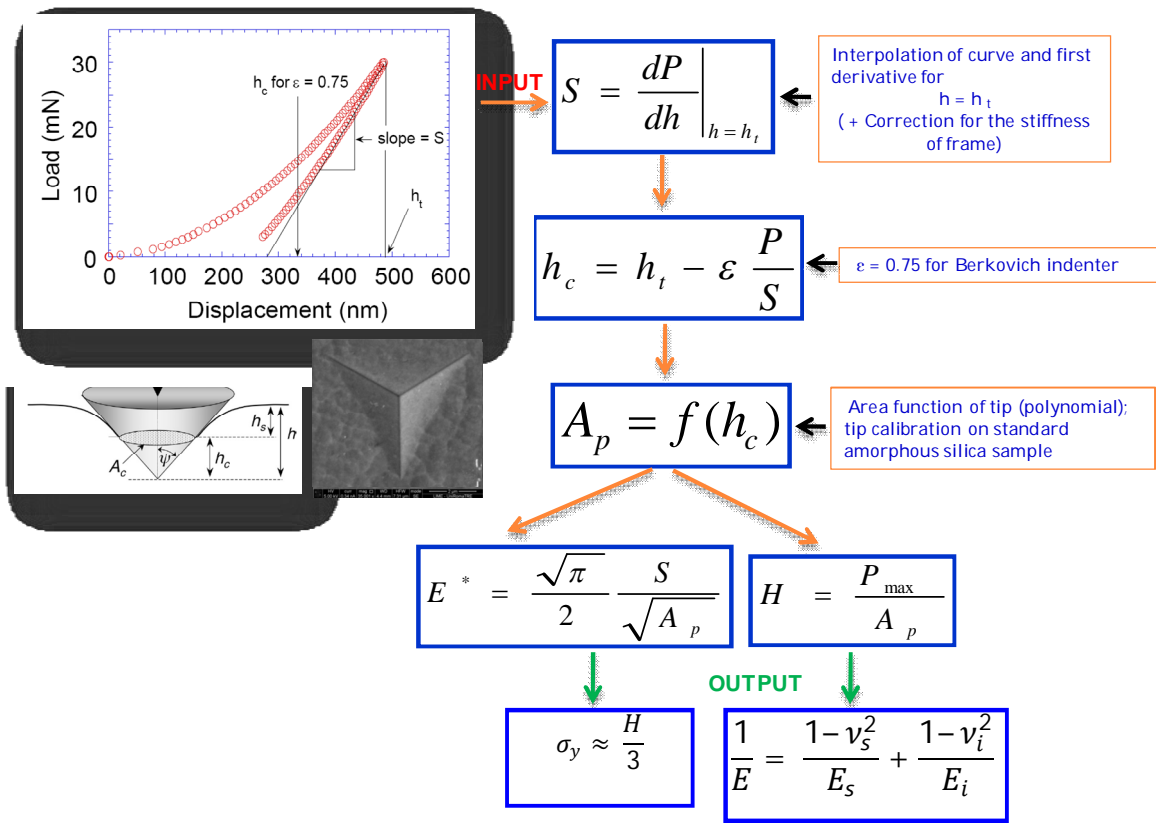
Fig. 4.7 Schematic summary of the procedure followed (Oliver-Pharr [56, 57]) for the calculation of hardness and elastic modulus for a standard nanoindentation test. INPUT is a generic curve Load-displacement, OUTPUT is the hardness and elastic modulus calculated at the maximum load.

In the present work, intrinsic hardness and reduced modulus of bilayer and three multilayer configurations were measured by nanoindentation (Nanoindenter Agilent G-200). A diamond Berkovich indenter was used to perform the measurement in continuous stiffness mode (CSM). This means that the contact stiffness was measured continuously as a function of displacement into surface, thus allowing for a continuous measurement of the indentation modulus and hardness. The correct load-displacement curves were analyzed with the Oliver and Pharr procedure and hardness and modulus were evaluated as an average of sixteen measurements. Mechanical properties were evaluated for penetration depth of 100-200 nm which is within 10 % of the coating thickness to avoid substrate effects.

4.6 Scratch Testing

The Scratch Test consists of introducing stresses at coating-substrate interface through diamond stylus with constant, progressively increasing normal load. The instrument controls vertical load on the indenter meanwhile the specimen is linearly moved. The stresses was generated as combination of indentation stress field, frictional stress field and residual stress present in the coating .The resulting stresses caused adhesive and cohesive failures. The smallest load is called the critical load at which a specific failure took place. Other transducers located in the specimen stage continuously recorded acoustic emission and tangential forces (friction force) during the test and used this information to estimate adhesive and cohesive events and friction coefficient, respectively. The track produced by the indenter is consequently observed with an integrated optical microscope and for more resolution with optical profilometer. Sometimes, the failure modes were analysed in detail by 3D microscopy, with the main objective of critical load evaluation for specific coating system. With the optical survey of the surface, it is possible to recognize typical critical load, where coating is damaged. Correlating the location on the track with the load applied, it is possible to establish the amount of force necessary to damage the coating.

In general, the standard scratch test [59] is effectively used for the substrate that does not deform plastically to any great extent before the coatings are effectively detached and uncover the substrate, which is used as indication of adhesion failure. The test depends on many other parameters such as indenter radius, coating thickness, residual stress in coatings and friction coefficient between diamond stylus and coatings. Therefore, results of the test are evaluated qualitatively in terms of good and bad adhesion rather than an absolute value of adhesion strength.

In the present investigations, the CSM Instrument Revetest Scratch Tester was used, a schematic illustration of this equipment is shown in Fig. 4.8.
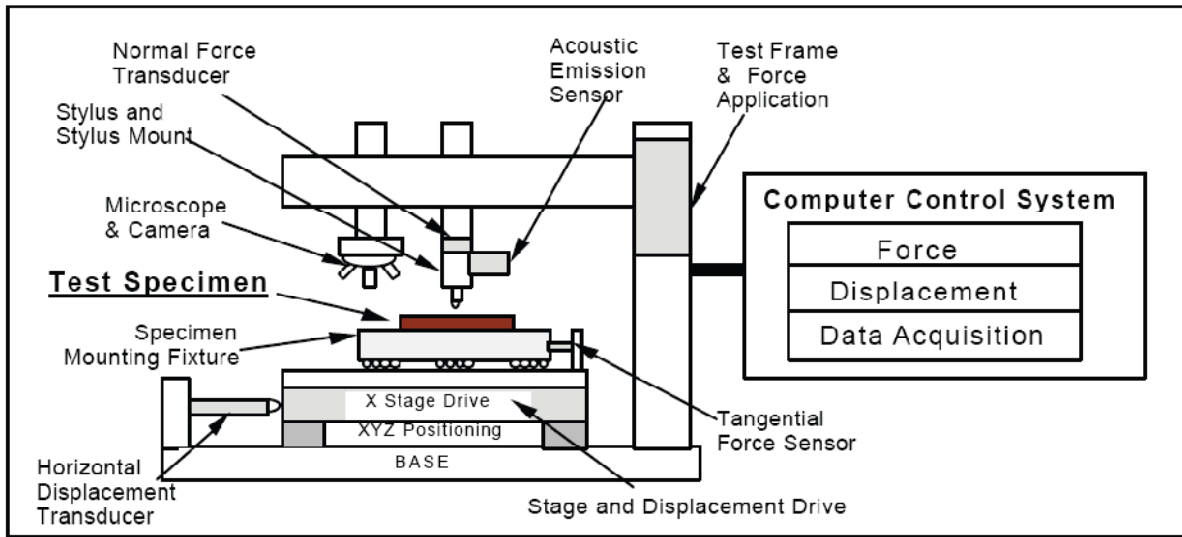
Fig. 4.8 Schematic illustration of scratch test instrument. Source [59]

Scratch tests were performed on bilayer and three multilayer configurations in order to evaluate adhesion to the stainless steel substrate. According to the UNI EN 1071 (3) Standard at least three scratches are performed on each sample with a CSM Instruments Revetest [60]. A 10 mm long scratch was made using the Rockwell "C" diamond indenter tips of radii 100 and 200 µm with sliding speed of 10 mm/min and loading rate of 30 N/min. A progressively increasing loading mode with starting load of 1N was used to identify the start of scratch track. Quite different failure modes were visible with different indenter radii. With indenter radius of 200 µm, scratch failures were characterized as: L_{C1}- buckling failure (semi-circular crack beyond scratch edge); L_{C2} - chipping at scratch edge with partial delamination; L_{C3} - complete delamination (appearance of substrate). However, for 100 µm indenter radius, critical failure were evaluated (critical loads: L_{C1}- first delamination (partial appearance of substrate); L_{C2} -complete delamination (semi-circular appearance of substrate)) by means of scratch data analyses. After scratch, the critical load for failure was calculated by analysing the scratch track using optical profilometer.

4.7 XRD Residual Stress Measurement

The X-ray diffraction is promising and widely used technique for residual stress evaluation in crystalline materials. It is developed from theories of crystallography and solid mechanics. Brief description of the physical principal involved for the evaluation of in-plane residual stress is the measurement of normal strain (ε_z) under the assumption of plane stress condition. The grains that have planes parallel to surface will diffract at certain 2θ angle. By the use of well-known Bragg's law the inter-planar spacing is measured. The inter-planar spacing acts as strain gauge. The magnitude of peak shift with reference to the stress free data of powder material is related to magnitude of residual stress. Thus, if there is no residual stress, the peak shift will be zero. The details of briefly described physical principal involved in XRD measurement is given below.

4.7.1 Bragg's equation

The X-rays diffracted from family of atom-containing planes in the crystal structure are in phase and constructively interfere with one another under the Bragg's conditions. Mathematically, the conditions are (Eq.4.8):

$$\lambda = 2d \sin \theta \qquad\qquad 4.8$$

Here λ is the wavelength of X-ray beam, d is inter-planar spacing, and θ is the angle of diffraction. The derivation of condition is as follows;
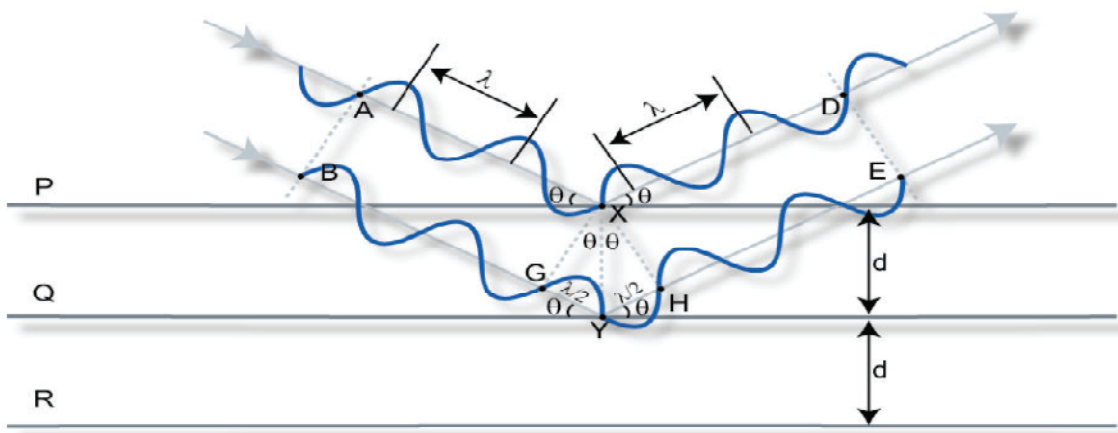
Fig. 4.9 Bragg's Conditions

48

Fig. 4.9 shows monochromatic X-rays beam incident on the surface of a crystal at an angle of θ. The P, Q and R represent a family of planes separated by the distance d. The plane P reflects AX in XD. Similarly, plane Q reflects BY in YE at the same angle θ. Although the beam penetrates many more planes only consider the top two.

As the plane Q is lower than P, the beam path BYE is longer than AXD by the amount equal to GY + YH. This is the path difference between two beams.

From the geometry of the Fig. 4.9,

The angle AXG = θ + angle PXG = 90°

Then angle PXG = 90° - θ

and angle PXY = PXG + GXY = 90°

Then angle GXY = θ

Similarly, YXH = θ

From the triangle GXY, the sin θ could be calculated as (Eq.4.9),

$$Sin\theta = \frac{GY}{d}$$
4.9

And from the triangle YXH, the sin θ could be calculated using Eq.4.10,

$$Sin\theta = \frac{YH}{d}$$
4.10

Therefore, the path difference (GY + YH) = 2d sin θ

The angle between the transmitted and diffracted beam is always equal to 2θ to fulfill the Bragg's conditions for diffraction from surface parallel planes. In Bragg-Brentano (θ-θ) arrangement, both the X-ray source and detector rotate around common axis at the center of goniometer where sample is placed which is stationary. The X-ray source, detector and sample form a vertical plane (scattering plane) while sample lies on horizontal plane. Both the X-ray source and the detector moves are synchronized to form equal angle with surface of sample. However, in θ-2θ configuration, the X-ray source is stationary while sample is rotated around the same axis as

detector. In this configuration, sample and detector are synchronized to meet the 2θ scattering conditions. Results of X-ray diffraction are always given in terms of 2θ. However, the angle used in Bragg's Equation to calculate the inter-planar spacing is always the angle between the incident and diffracted beam, i.e θ.

4.7.2 Measurement of strain

Inter-planar spacing between the parallel planes acts as strain gauge. When the material is strained, elongation and contraction will produce within the crystal lattice as a result of Poisson's ratio which will change the inter-planar spacing in the lattice planes.

Under plane stress conditions, stress normal to surface of sample will be zero; however the strain will not be equal to zero. The strain ε_z is then measured precisely in shift of peak position with reference to unstrained inter-planar spacing d_0. Mathematically the ε_z can be determined following the Eq.4.11 as:

$$\varepsilon_Z = \frac{d_n - d_0}{d_0} \qquad \qquad 4.11$$

Equation 4.11 gives strain normal to surface of sample. By tilting the sample, measurement of inter-planar spacing between planes at an angle of Ψ is made and strain along that orientation is calculated using Eq. 4.12 as:

$$\varepsilon_{\Phi\Psi} = \frac{d_{\Phi\Psi} - d_0}{d_0} \qquad \qquad 4.12$$

Planes parallel to the surface and at an angle of ΦΨ to the surface of sample are shown in Fig. 4.10. This is to illustrate how the strains (inter-planar spacing) at angle to sample surface are measured by tilting the scattering vector.
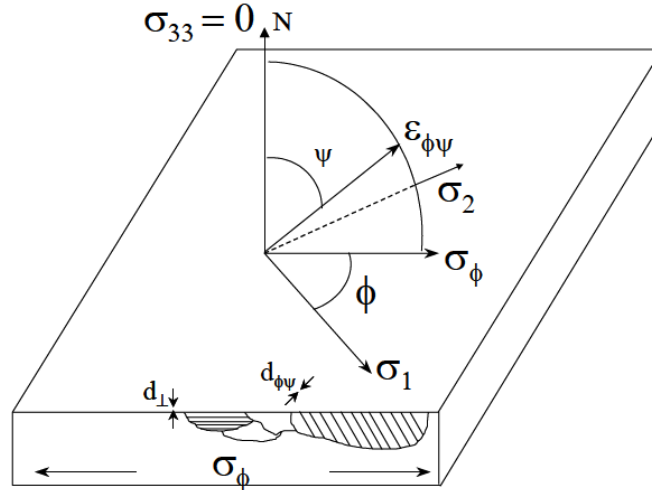
Fig. 4.10 Plane stress elastic model. Source [61]

The measured strain is always normal strain as the scattering vector is rotated with Ψ rotation to fulfil the Bragg's conditions. In order to find the in-plane stress, strains are then transformed from measuring coordinate system to sample coordinate system using strain transformation tensor from theory of elasticity.
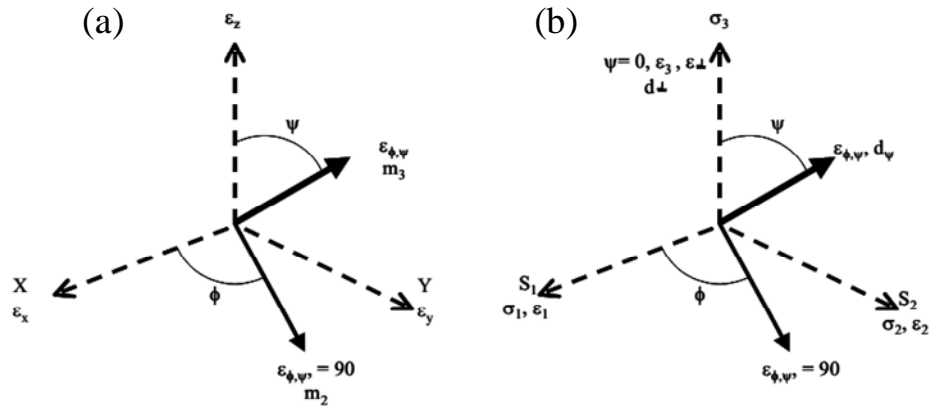
Fig. 4.11 Coordinate systems used for stress and strain calculations: (a) Principal axis of strain, (b) principal stress corresponding to stress and strain orientations.

According to theory of elasticity for isotropic materials, the strain along an inclined line m_3 in Fig. 4.11a is corresponding to the tilt and orientation of sample. The strain ($\varepsilon_{\Phi\Psi}$) in the orientation is defined by angle Φ and Ψ (Eq. 13) as:

$$\varepsilon_{\Phi\Psi} = \frac{1-\nu}{E}(\sigma_1 \cos^2 \Phi + \sigma_2 \sin^2 \Phi)\sin^2 \Psi - \frac{\nu}{E}(\sigma_1 + \sigma_2) \qquad 4.13$$

51

4.7.3 Stress calculations

Once the strains are measured, then stresses are related to these strains by Hook's law (Eq. 4.14) as:

$$\sigma_y = E\varepsilon_y \qquad\qquad 4.14$$

It is also well known that the tensile force in x-direction could not only produce strain in that direction but also results in the compressive strain in the transverse directions. The ratio of transverse to longitudinal strain is Poisson's ratio (v) and is determined using the Eq. 4.15 as:

$$\varepsilon_x = \varepsilon_y = -v\,\varepsilon_z = -\frac{v}{E}\,\sigma_y \qquad\qquad 4.15$$

According to X-ray measurement, the strain in z-direction is related to strain in other two directions using Hook's law in three dimensions as in Eq. 4.16 below:

$$\varepsilon_z = -v\,(\varepsilon_x + \varepsilon_y) = -\frac{v}{E}\,(\sigma_x + \sigma_y) \qquad\qquad 4.16$$

By putting the value of ε_z from equation 4.13 into Eq. 4.17, the expression (Eq. 4.17) is as:

$$\frac{d_n - d_0}{d_0} = -\frac{v}{E}\,(\sigma_x + \sigma_y) \qquad\qquad 4.17$$

For the biaxial state of stress, the equation 13 takes the form of Eq. 4.18 as:

$$\frac{d_{\Phi\Psi} - d_0}{d_0} = \frac{1 + v}{E}\,\sigma_\Phi \sin^2 \Psi - \frac{v}{E}(\sigma_1 + \sigma_2) \qquad\qquad 4.18$$

Where the elastic constants E and v are not the bulk values but are the values of crystallographic direction normal to lattice planes defined by Miller Indices (hkl) in which the strains are measured. Equation 4.18 describes the basic relationship between inter-planar spacing and biaxial stress in the sample. The inter-planar spacing $d_{\Phi\Psi}$ is linear function of $\sin^2 \Psi$. The actual dependence of inter-planar spacing of (311) plane for Ψ ranging from 0 to $45°$ for shot peened 5056-O aluminum having stress of -148 MPa is shown in Fig. 4.12.
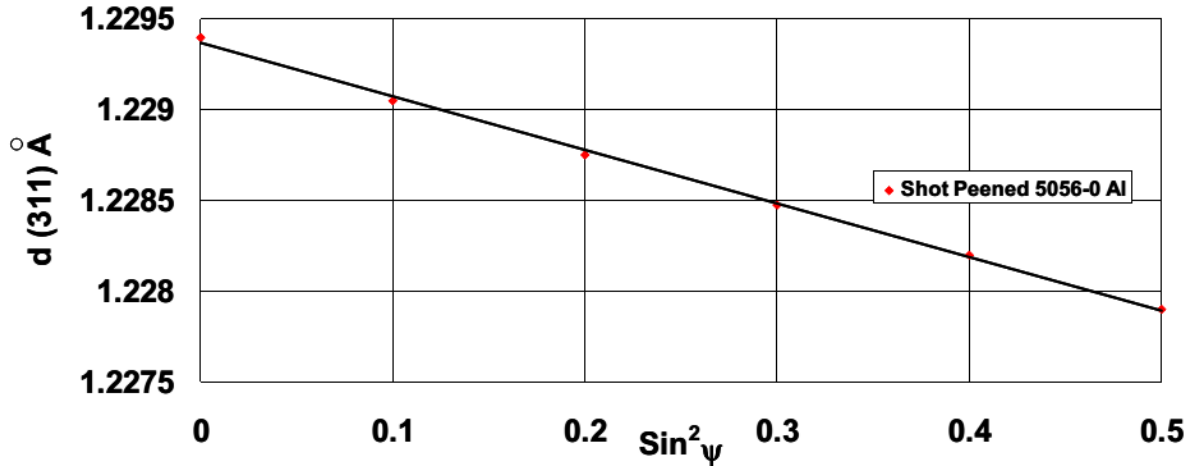
Fig. 4.12 Linear dependence of inter-planar spacing of plane (311) upon $\sin^2\Psi$ for 5056-O aluminum shot peened alloy. Source [62]

The straight line is fitted by least square regression analysis. The intercept of the plot at $\text{Sin}^2\ \Psi = 0$ is equal to unstressed inter-planar spacing (d_0), minus the Poisson's ratio contraction caused by the sum of principal stresses (second term on right hand side of Eq.18). Finally, the slope of plot is in-plane stress and can be calculated using Eq. 4.19 as given below:

$$\sigma_\Phi = \frac{E}{(1 + v)\sin^2 \Psi}\ \frac{d_{\Phi\Psi} - d_n}{d_n} \qquad\qquad 4.19$$

This is classical method for residual stress evaluation and is known as $\text{Sin}^2\ \Psi$.

In this work, in-plane residual stresses analyses in the bilayer and three multilayer configurations were conducted with Bruker D8 Discover System in parallel beam geometry optics arrangement using Cu-K$_\alpha$ radiation ($\lambda = 1.54$ Å). As the precision of residual stress measurement with classical X-ray $\sin^2\ \Psi$ method depends strongly on accurate determination of diffraction peak position. Several full scans in Bragg-Brentano (θ-2θ scan mode) were performed to identify the peak at high angle to be used for residual stress quantification. The TiN (111) peak shifted with reference to the standard TiN powder diffraction data which showed that coatings were (under or over) stoichiometric [63]. Moreover, the low angle peak (111) was intense and higher angle peaks were very weak. By tilting for Ψ measurements the peaks are disappeared that could be due to the texture in coating. Therefore, the X-ray data were collected for peaks (422) and (511) for all the samples at

grazing-incidence X-ray diffraction (GIXRD) for qualitative residual stress analyses. The grazing angle was set at 1° for all the samples with a scan step size of 0.02° over a 2θ range of 110° to 160°. The grazing-incident is reasonable to have residual stress from a shallow region of coatings for qualitatively comparison.

Chapter 5 RESULTS AND DISCUSSION

5.1 FEM based Design of Stress-Optimized Ti-TiN Multilayer PVD-Coatings

Results of residual stress modelling and the optimization of multilayer coatings thickness for minimization of residual stress are summarized in this section. In the first subsection (5.1.1), interfacial axial and in-plane shear stress induced by the thermal and intrinsic stress in bilayer and multilayer configurations is compared. In the subsequent subsection, results of multilayer coating configurations optimized under variable position and thickness of all the layers are elaborated. Finally, conclusions of modelling results are presented.

5.1.1 Stress analysis in bilayer and multilayer coating configuration

The failure mechanisms in coatings as described in the Literature Review Chapter are mainly controlled by the magnitude of in-plane stress and interfacial stress (axial stress and in plane shear stress). In-plane normal stress at the centre of axi-symmetric model in compressive state is of practical significance, as buckling could result from this component. Similarly, axial normal stress and in plane shear stress at the edge of model are most important to address the peeling and spallation related failure mode in the coatings. These stress components are first analysed in bilayer and multilayer coating configuration subsequently multilayer coating configuration is subjected to stress-optimization.

At first, the finite element analyses was performed for model verification, validation and then independent effect of thermal and intrinsic stresses are analysed. Thermal in-plane stress as shown by open circle in Fig. 5.1 is predicted in TiN ceramic layers along the node path in correspondence of the model axi-symmetric axis. According to bimetallic strip model [36], thermal stress in coating after assumed deposition temperature could be compressive or tensile depending on the thermal expansion coefficients of the coating and the substrate. If the coating thermal expansion coefficients are lower than the substrate during cooling the substrate will contract more than the coating. As a

result compressive stress will be generated in the coating. Thermal stress in TiN and Ti layers are in accordance with the thermal expansion properties used in the present study. This stress component has been also analytically evaluated for one dimensional case using Eq. 3.4 given in Chapter on Modelling Activities without considering substrate bending. The FEM calculations showed good agreement with elastic theoretical solution which ensured proportionate thickness of substrate in numerical model.
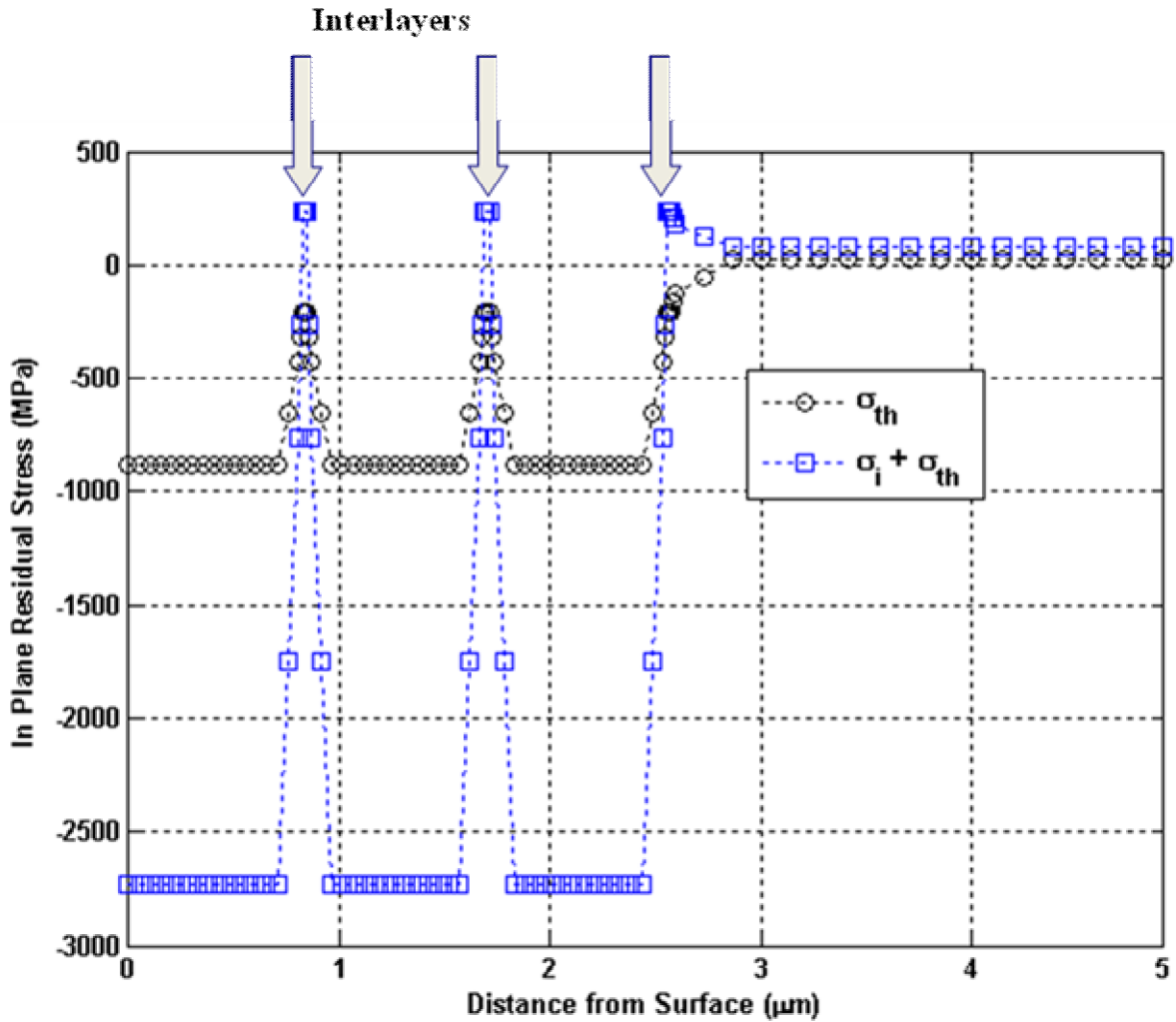
Fig. 5.1 Predicted average in-plane normal stress in multilayer configuration (MMPI)

Analytical solutions of the in-plane thermal stress developed up-till-now do not take into account the average intrinsic stress component. On reproducing average intrinsic stress of -2 GPa from

growth stress model [14] in all the TiN layers and intrinsic stress of 1 GPa in all the Ti layers, the resulting magnitude of the in-plane stress is shown by square dots in Fig. 5.1. From the plot, it seems that final stress increased in uniform manner by just superimposing on the thermal stress. However, the stress magnitude is not just the addition rather it is slightly less under the influence of intrinsic stress imposed on Ti interlayers. It is also noted (Fig. 5.1) that stress peak in Ti layer changed from compressive to tensile. The stress in each layer is an average value because only elastic analysis was performed in the present studies and results are compared with the exact analytical solution. Therefore, final stress state is under combined effect of the average intrinsic stress and thermal stress. Of course during optimization, average thickness dependent intrinsic stress in each TiN layer was reproduced while constant intrinsic stress was imposed on all the Ti layers.

The results of the finite element modelling of the interfacial axial stress (under the influence of both thermal and intrinsic stresses) for bilayer (BL) and multilayer configuration (MMPI) in terms of stress profile through thickness of coating (from surface to few microns into substrate) with respect to Ti interlayer position is presented in Fig. 5.2. The axial stress along the node path corresponding to the model edge is also depicted in Fig. 5.2. As expected, out-of-plane (axial stress) stress showed a peak in TiN layer adjacent to substrate and obviously is zero at the free surface. Theoretically, it makes sense that maximum stress should be at interface between the coating and the substrate material. This seems due to large mismatch of the thermal expansion and the elastic modulus between TiN and substrate material. The Ti bond layer between TiN coating and substrate decreased the thermal and elastic modulus mismatch. As a result, interfacial stress decreased and adhesion improved. This observation is in accordance with the experimental studies in scientific literature [65]. Qualitative comparison of axial stress component (Fig. 5.2) in multilayer coating configuration (MMPI) and bilayer (BL) showed a difference of ≈ 16 %. The introduction of two Ti interlayers showed significant decrease in the interfacial axial stress.
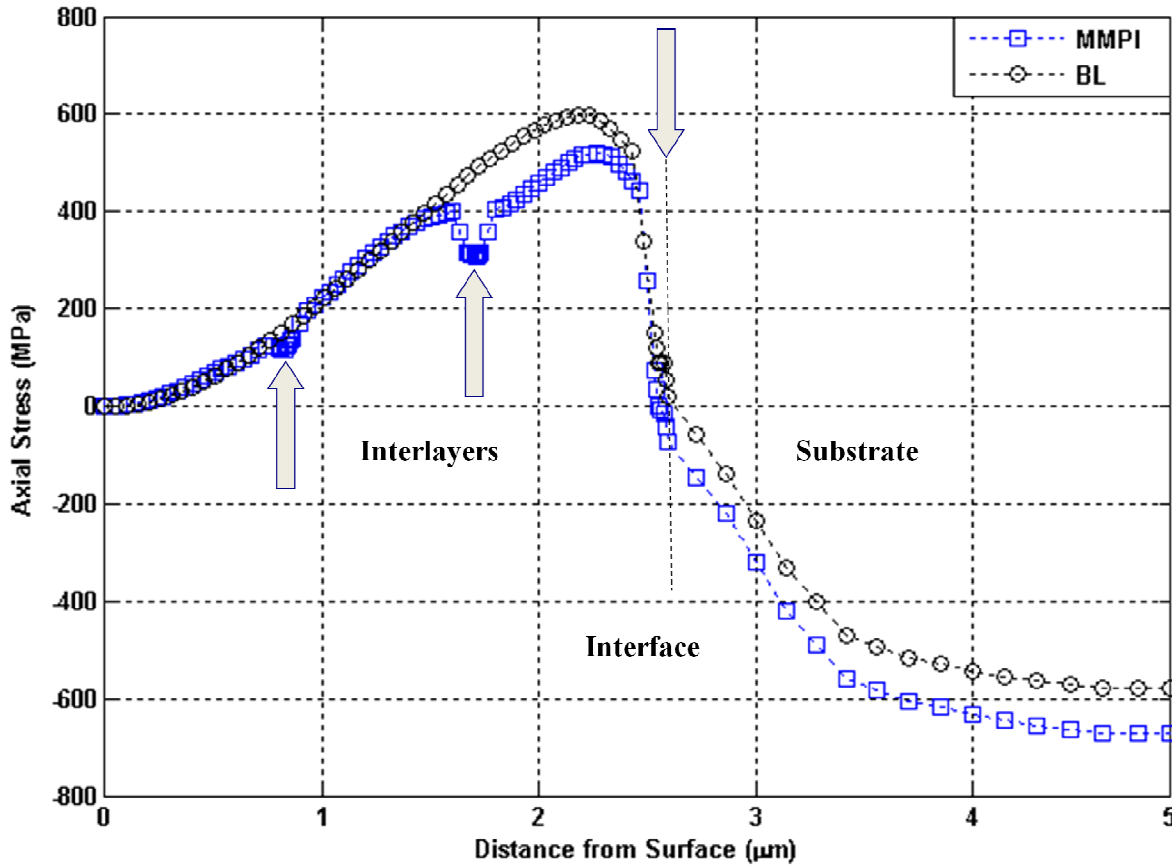
Fig. 5.2 Qualitative comparison of predicted shear stress in model BL in comparison with model MMPI

The in-plane shear stress in the bilayer (BL) and multilayer configurations (MMPI) was found far less than other stress components such as axial stress (out-of-plane) and in-plane stress along the same path (Fig. 5.3). Maximum shear stress was at interface between the TiN and Ti bond layer close to the substrate and peak of maximum slightly shifted towards Ti bond layer which could affect adhesion adversely. For bilayer, stress reversal (from compressive to tensile) took place only at interface. However, in multilayer stress reversal took place at each of the interface. In multilayer (MMPI), there are two peaks at each of the interface. Ti interlayer at each of interface caused tensile stress due to tensile intrinsic stress in interlayers. Similarly bond layer having tensile intrinsic stress of 1 GPa caused maximum tensile shear stress in the Ti bond layer, depending on ideal elastic-plastic properties of Ti layers assumed in this study.
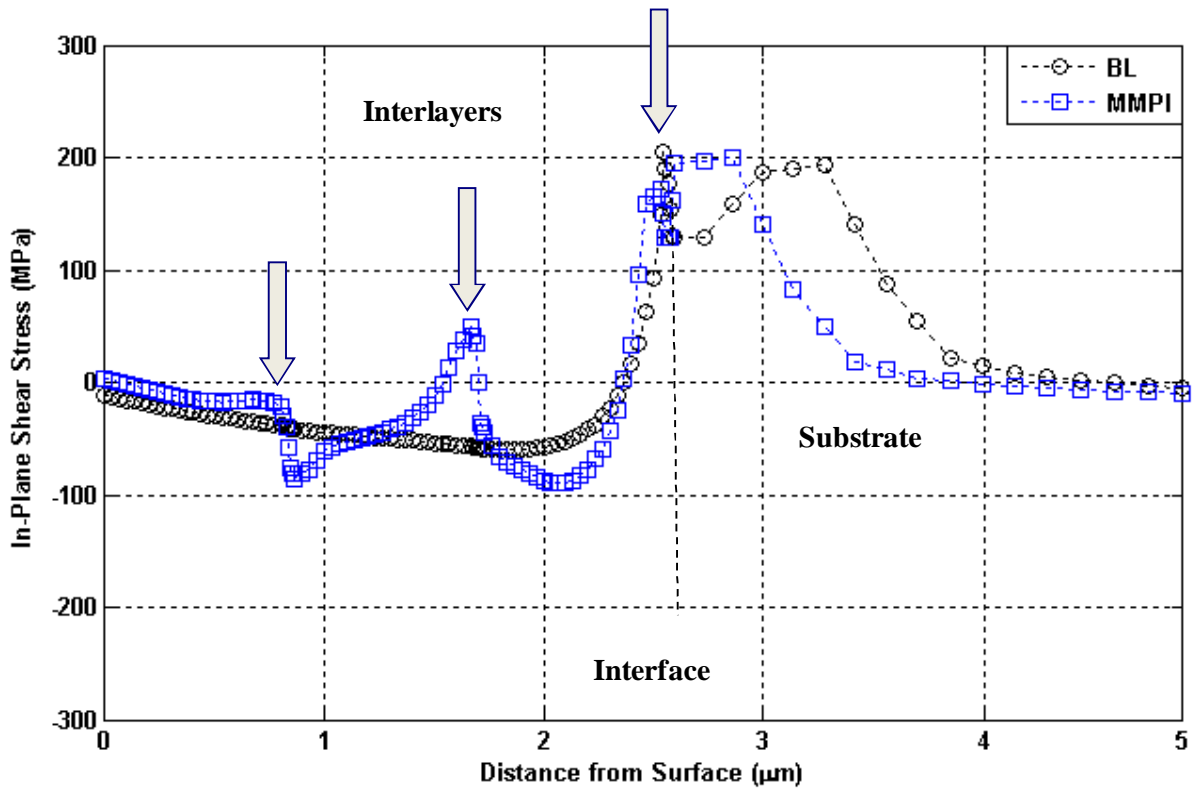
Fig. 5.3 Qualitative comparison of predicted normal to surface stress in model BL in comparison with model MMPI

5.1.2 Residual stress optimization in multilayer coating configuration

Based on axial stress profile in multilayer configuration MMPI (Fig. 5.2), which is not symmetric as maximum magnitude is in TiN layer close to the substrate; three types of optimization run were performed. During the first optimization, only the thickness of Ti interlayers and bond layer were changed to see that which Ti layer thickness effectively decrease the axial interfacial stress. The optimization iteration results are shown in Table 5.1. The optimization iteration mimics the stress profile of MMPI is shown in the Fig. 5.2. All the iterations in Table 1 showed a decrease in maximum stress value. However, iteration No. 7 showed higher decrease in axial stress probably due to increased Ti quantity from top towards the coating substrate interface. It is clear from the axial stress profile as well as from the iteration results (Table 5.1) that Ti bond layer and the first Ti interlayer thickness are most effective to decrease the stress. The axial stress profile (from surface

59

of coating to coating-substrate interface) in both the BL and MMPI remained almost similar up to the second Ti interlayer (Fig. 5.2).

Table 5.1 Iteration results of multilayer MMPI under Ti interlayer thickness variation

It. No	Axial stress (OBJ) (MPa)	Ti interlayer thickness (DV) (nm)			Total Ti Thickness (nm)
		Bond	1st	2nd	
1	530	60	60	60	180
2	510	69	78	93	240
3	467	80	81	87	248
4	497	73	60	93	226
5	460	83	91	72	246
6	444	95	96	96	287
7	435	99	98	70	295

From the first hand observation, the second optimization run was performed in which only the thickness of all the TiN layers were changed within fixed Ti interlayer thickness; this only changed the position of Ti interlayer compared with the middle position of Ti interlayer MMPI. The thickness of all the TiN layers was changed within the fixed total thickness of all the TiN layers. By changing the position of Ti interlayers, a significant decrease in the interfacial axial stress was recorded (Fig. 5.3). The decrease in stress was $\approx$ 10 % compared with multilayer configuration in which all the TiN layers have equal thickness; however, it is significantly decreased in comparison with bi-layer. The optimization iteration results are shown in Table 5.2.

Table 5.2 Optimization iteration results for multilayer with optimal position of inter-layer (MOPI)

It. No	Axial stress (OBJ) (MPa)	TiN layers thickness (DV) (nm)			Total TiN Thickness (nm)
		First	Middle	Top	
1	530	800	800	800	2400
2	480	730	900	900	2530
3	570	810	760	1300	2870
4	620	730	500	1400	2630
5	800	500	900	1000	2400
6	430	570	725	1100	2400

Minimum axial stress was recorded in optimization iterations number six (Table 1.2). It corresponds to the decrease in thickness of TiN layer (1st TiN layer) close to substrate and an increase in

thickness of top TiN layer. However, according to iteration number five, thickness dependent intrinsic stresses put a cap on the thickness of TiN first layer. While comparing iteration number two and six, decrease in thickness of the second TiN layer also could also has induced a decrease in the axial stress.

The third optimization with the combination of the first and second optimization was performed in which thickness of both Ti and TiN layers were changed and named it as MOTI. A decrease of ≈ 25 % in the axial stress was observed with an increase of ≈ 4 % relative quantity of Ti in the multilayer. With further increase in Ti interlayer thickness and a decrease in the TiN layer thickness within the specified final thickness, thickness dependent residual stress involved that perhaps also limited the optimization and increased in the Ti layer thickness but is practicably unacceptable. Optimization iteration results in terms of layer thickness and its influence on axial stress are shown in Table 5.3.

Table 5.3 Optimization iteration results for optimal position and thickness of interlayer (MOTI)

It. No	Axial stress (OBJ) (MPa)	Optimal thickness of Ti interlayers and TiN layers (DV) (nm)					
		Bond layer	1st TiN	1st Ti	2nd TiN	2nd Ti	Top TiN
1	530	60	800	60	800	60	800
2	540	85	847	76	876	85	1135
3	581	83	896	72	904	60	1135
4	458	99	764	64	825	62	1021
5	465	92	738	82	1100	66	973
6	373	120	650	82	610	60	1120

Finite element results showed that axial stress at radial free edge played a major role in the optimization of Ti and TiN thickness in multilayer configurations. The decrease in stress is much effective in case of model MOPI (Fig. 5.4). However, in case of model MOTI, an increase in thickness of intermediate Ti interlayer and interlayer between the coating-substrate interface lead to a much more effective decrease in stress peak probably by elastic deformation of less stiff Ti layers while Ti interlayer close to top surface remained ineffective. It was found that axial stress was distributed similarly in all the configurations (bilayer and multilayer), but the peak value of stress

varied from one configuration to another. The peak value was significant to enhance crack propagation from the edge, along the interface or within the TiN close to the interface [38].

Fig. 5.4 Qualitative comparison of predicted normal to surface stress profile in two models of multilayer configurations, MOPI and MOTI in comparison with model MMPI.

Since, the comparison of these out-of-plane stress component with the experimental measurements involved synchrotron nano-beam stress analysis [66]. However, qualitative comparisons (Fig. 5.4) sufficiently show different residual stress level in the different multilayer configurations. The optimization of multilayer configurations involved a decrease in only the axial stress component at the edge of model. As a result, it seems possible that other stress components such as in-plane shear and in-plane residual stress might increase. Therefore, as a monitoring check, in-plane shear stress was analysed during the finite element calculations along the same path and in-plane residual stress was experimentally investigated with X-ray diffraction. In order to make sure that minimization of axial stress component might not increase other stress components; multilayer configurations were

62

simulated for evaluation of average in-plane shear stress component along the same paths. A decrease of few MPa in in-plane shear stress was observed as compared with the starting multi-layer configuration (MMPI). The increase in Ti interlayer thickness decrease the shear stress level but not very significant decrease was recorded as in case of MOTI (Fig. 5.5) as the flexible Ti bond layer between TiN coating and steel was used to increase the adhesion by reducing the shear stress [26, 27].
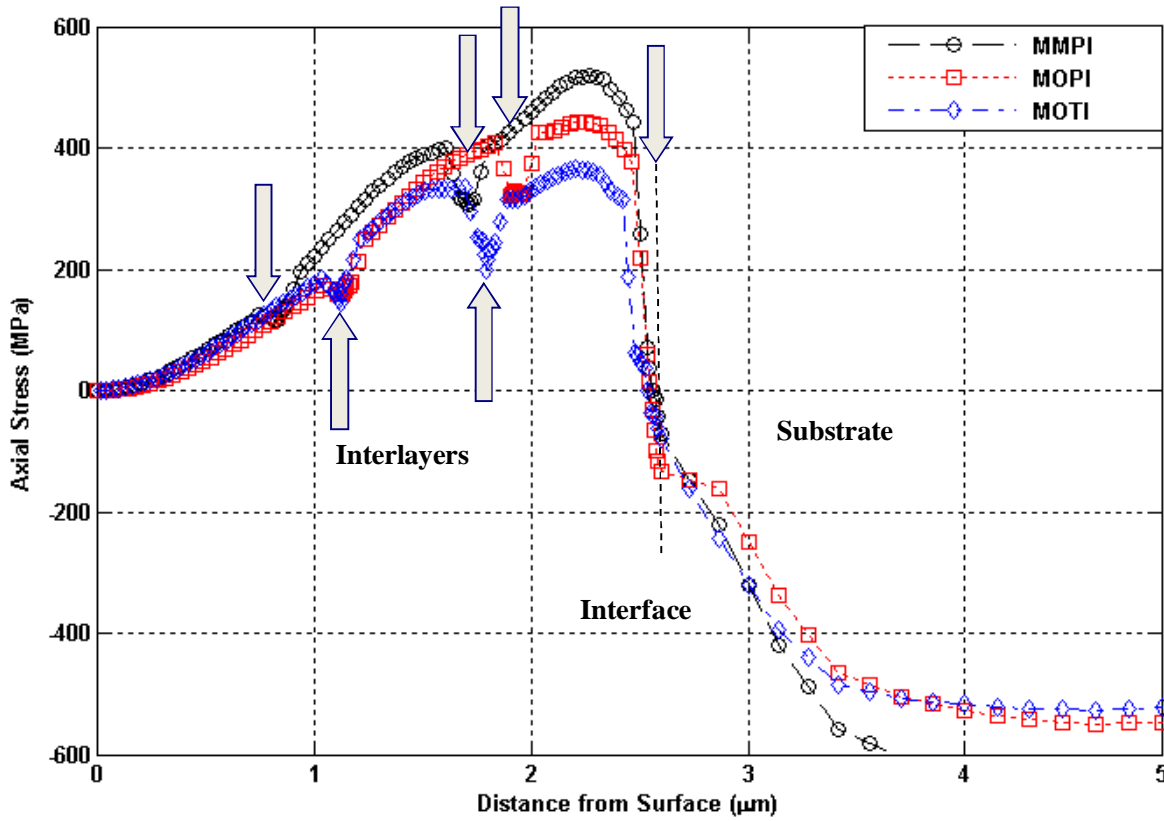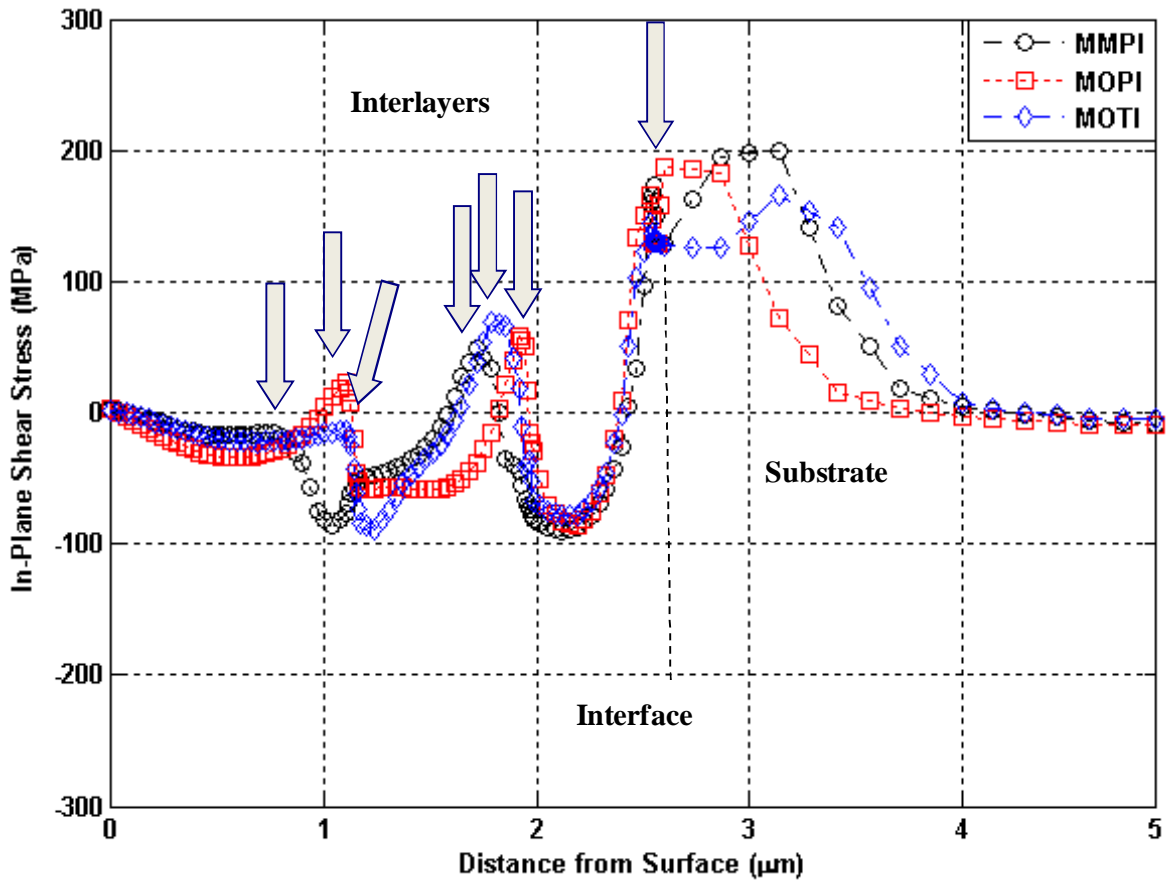

Fig. 5.5 Qualitative comparison of predicted in-plane shear stress profile in two models of multilayer configurations, MOPI and MOTI in comparison with model MMPI.

Finally, for the production and characterization, the two optimal configurations in comparison with BL and MMPI are described in terms of individual layer thickness (thickness of layers is always starting from top layer):

iii.   Model type of bilayer "BL" (single layer of 2.55 μm thickness and Ti interlayer of 0.05 μm thickness);

iv.   Model type multilayer with middle position of Ti interlayer "MMPI" (three TiN layers each of 0.80 μm thickness and three interlayer of Ti each of 0.06 μm thicknes).

v.   Model type "MOPI": Multilayer with optimal position of Ti interlayers (three TiN layers of thickness 1.10, 0.73 and 0.57 µm, and three interlayer of Ti having equal and similar thickness to model type MMPI);

vi.   Model type "MOTI": Multilayer with optimal position and thickness of Ti interlayers (three TiN layers of 1.10, 0.60 and 0.64 µm thicknesses, and three interlayer of Ti having thickness of 0.06, 0.08 and 0.12 µm).

5.1.3 Conclusions

Finite element analyses in conjunction with optimization technique was used to design a six-layer Ti-TiN multi-layer coating architecture for optimal layer thickness in order to decrease the interfacial stresses which mostly affect the coating adhesion. The findings help to main conclusions as:

- The interposition of a ductile Ti interlayer always involved a decrease in the predicted interfacial residual stress peak (axial stress component);

- The effectiveness of this Ti layer was strongly influenced by its position and followed by its thickness;

- The interfacial axial peak stress was relieved by ≈ 10 % by changing position of Ti interlayers.

- The interfacial axial peak stress was relieved by ≈ 25 % by increasing relative quantity of Ti by ≈ 4 % in relation to multilayer with middle position of interlayers.

5.2 Influence of Ti-TiN Multilayer Coating Design on Mechanical Properties and Scratch Adhesion

In this section, experimental results of the coatings produced based on FEM optimizations are presented. The morphological characterization including individual layer thickness and the presence of columnar structure was examined using the FIB. Mechanical response of multilayer is recorded using nanoindentation testing to investigate the stiffness and hardness in comparison with bilayer. Finally, the influence of multilayer coating design on the practical scratch adhesion is investigated.

5.2.1 Focused ion beam thickness evaluation

After deposition, the thickness of individual layer in multilayer and presence of Ti interlayer was observed with focus ion beam (FIB) cross-section measurements (Fig. 5.6).

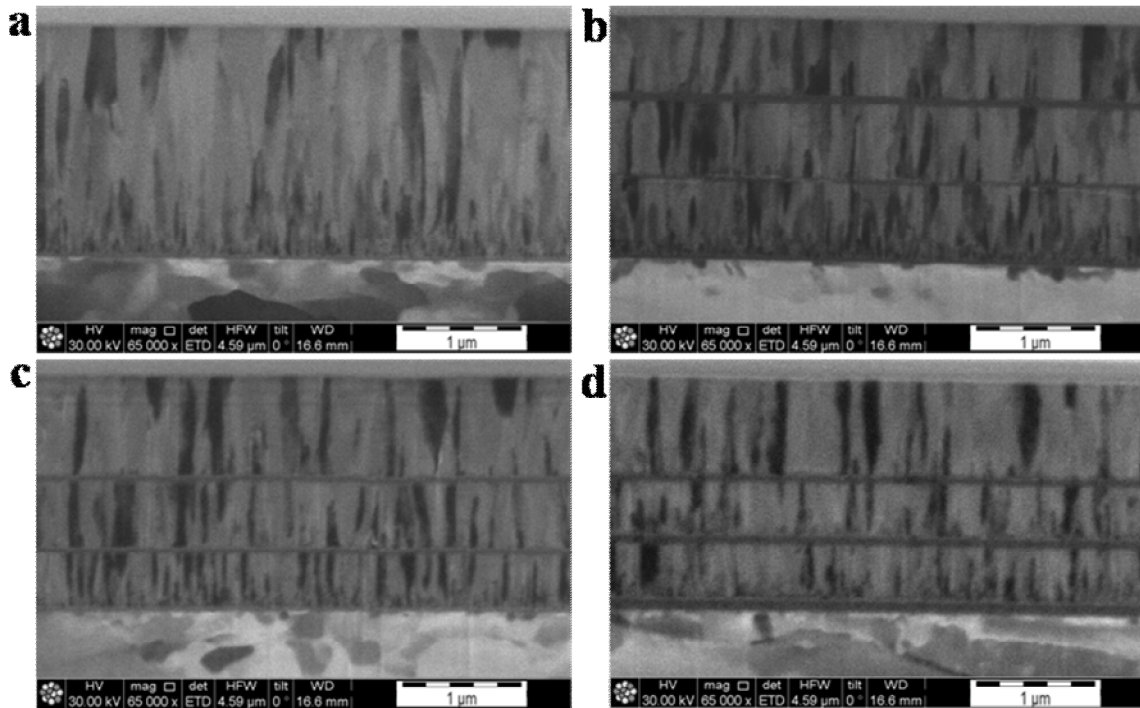Fig. 5.6 The FIB cross-section observation (30 kV, ETD, 65000x in all cases): (a) sample BL, (b) sample MMPI, (c) sample MOPI, (d) sample MOTI. Columnar structure and presence of Ti layer is clearly visible.

The sample MOTI (multilayer with optimal thickness of interlayer) showed slightly less overall thickness. Individual TiN layers and Ti interlayer thickness remained within the range of $\pm$ 50 nm

and $\pm$ 10 nm, respectively. All the samples show columnar growth in all the TiN layers. However, layers close to substrate showed a dense growth of columns which could result in relatively higher stress in the layer. It is not possible to interpret the microstructure of Ti thin films with models reviewed in the Literature Review Chapter.

5.2.1 Nanoindentation testing

Results of indentation test in bilayer and different multilayer configurations on stainless steel substrate are presented in Fig. 5.7. An increase in hardness at shallow displacement resulted from surface roughness. The difference in hardness and modulus between bilayer and multilayers is due to more measurements are performed on bilayer sample in comparison with multilayer samples. For penetration depth of 100 nm multilayer configuration showed slightly higher hardness than that of bilayer but it remained within limits of standard deviation. By taking penetration depth of 150 nm (penetration depth less than one-tenth of coating thickness) multilayer with middle position of interlayer slightly decrease its hardness in comparison with bilayer configurations. The difference in hardness between the remaining two multilayer configurations appeared most probably due to Ti quantity.

The nanoindentation modulus for coating configurations is shown in Fig. 5.7b. The values were derived from the continuous stiffness measurements mode. The effective modulus values of multilayers decreased with increasing displacement into coated system. The hardness and modulus remained more stabilized at penetration depth of 100 nm.

The results showed that hardness and modulus of multilayer configuration remained unaffected by the addition of Ti interlayers, even by increasing the Ti thickness up to 120 nm (Ti bond layer) and intermediate Ti layer (80 nm) in this study.

a

b
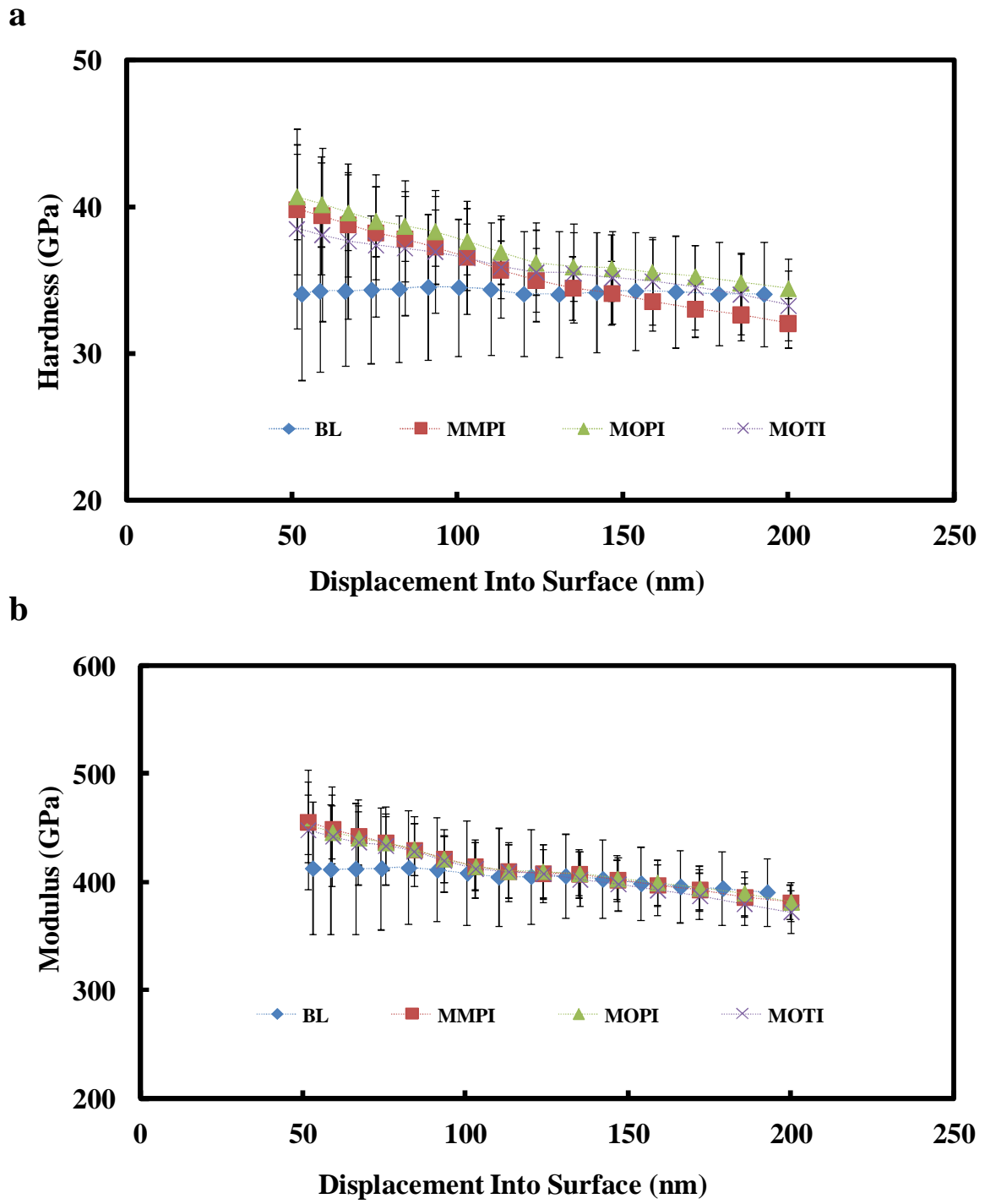
Fig. 5.7 Intrinsic hardness and elastic modulus of bilayer and multilayer configurations

5.2.3 Scratch adhesion testing

5.2.3.1 Standard scratch test with indenter of radius 200 μm

The scratch test with standard indenter of radius 200 μm was performed for the evaluation of coating adhesion to the stainless steel substrate. The first critical failure in all the configurations was a semi-circular crack (cohesive failure) as a result of extensive deformation in the substrate (Fig. 5.8). On comparing the difference in position of these cracks for critical load evaluation, the first visible crack in bilayer was ≈ 1 mm from starting point. However, in multilayer configuration having middle position of Ti layers (MMPI), it was at ≈ 2 mm. Also, tensile crack parallel to trailing edge of indenter on site of buckling failure was visible in multilayer configurations which showed that coatings were still fully adhered to the substrate [48].
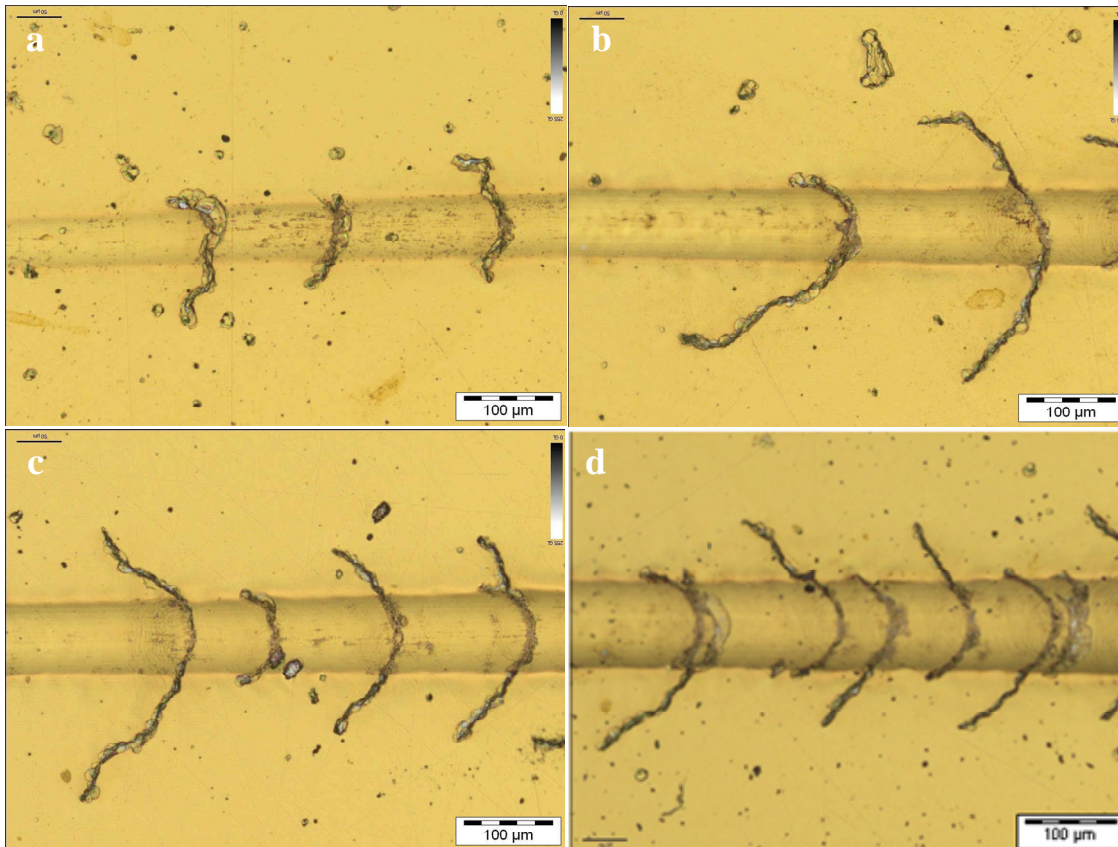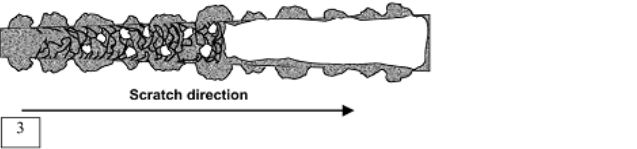
Fig. 5.8 Optical profilometer images at first critical (buckling cracks) failure in bilayer and multilayers: (a) Sample BL, (b) sample MMPI, (c) Sample MOPI, and (d) Sample MOTI.

It seems that radial cracks within and outside of scratch track most probably appeared due to the radial stress which is very much higher and continuously increased at coating surface with deep penetration of indenter into the substrate. Further, when multilayer was compared with different optimal configurations, there was a slight difference in the first critical load between multilayer with middle position of interlayer (MMPI) and with optimal position of interlayer (MOPI). The trailing cracks beyond scratch track edges were similar to those observed by Salas et al. [67]. They attributed these cracks to be associated with relatively tough coatings and high adhesion. In their studies, the investigated coatings are deposited on 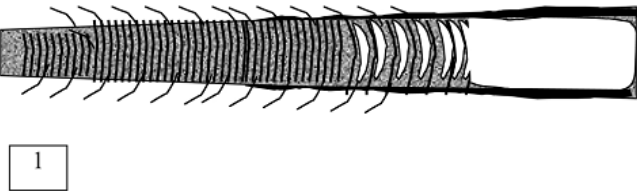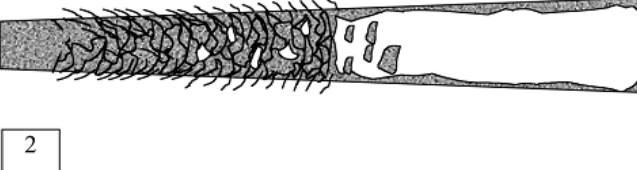aluminium die-casting dies made of tool steel grade H13. Even though the substrate has significantly higher hardness (HRC49), but the cracks showed that substrate was sufficiently ductile or coatings are tougher and had high adhesion. The crack morphology is presented here for comparison of crack mark morphology in the present studies (Table 5.5).

Table 5.4 Scratch marks morphology [67]

Scratch Morphology	Coatings (Lc)	Remarks
1	ZrN (46/63) CN (79) MoNx (66) TiAlN (59) CrN2 (47) CrN1 (44) TiN/TiCN (45) MoZrN (34)	**Good adhesion behavior:** Very fine semi-circular cracks within scratch and trailing cracks along edges. Deep scratches. Rel. tough coatings. High Lc values.
2	Cr₃Si (32) CrC (55) NiAl (55)	**Moderate to good adhesion behavior:** Coating cracking and some chipping within scratch. Moderate coating toughness and intermediate Lc values.
3	NiAlN (35) Ti-B-C-N (21) MoSiC+SiC (23) TiB2/TiC (20)	**Poor adhesion behavior:** Massive coating delamination along edges and multiple coating cracking and chipping within scratch. Brittle coating and low Lc values.

Attar et.al [68] also attributed the extensive transverse cracking of coating on tool steel substrate with a good adhesion of coating.

The second critical load was recorded when chipping at scratch edge accompanied with partial

within scratch track was observed (Fig. 5.9). Chipping at scratch edge appeared mostly due to bending induced tensile stresses, which was relatively higher on the surface of coatings, at the border of scratch channel. Instead of having differences in normal load for this failure, large differences in chipping damage area between bilayer and multilayer were also prominent. This damage was sudden in bilayer. However, in multilayer it occurred with intermediate radial crack formation and crack extension beyond scratch channel which indicated toughening response of multilayer. As seen from images (Fig. 5.9) that less chipping damage, higher critical load and increase buckling crack beyond scratch edge indicated tougher response of multilayer. It seems that in response to better adhesion, the mechanical energy was dissipated by extensive transverse cracking and edge chipping accompanied with less delamination within the scratch track. In addition, it is further supported by the appearance of fine cracks within scratch track parallel to trailing edge of the indenter.
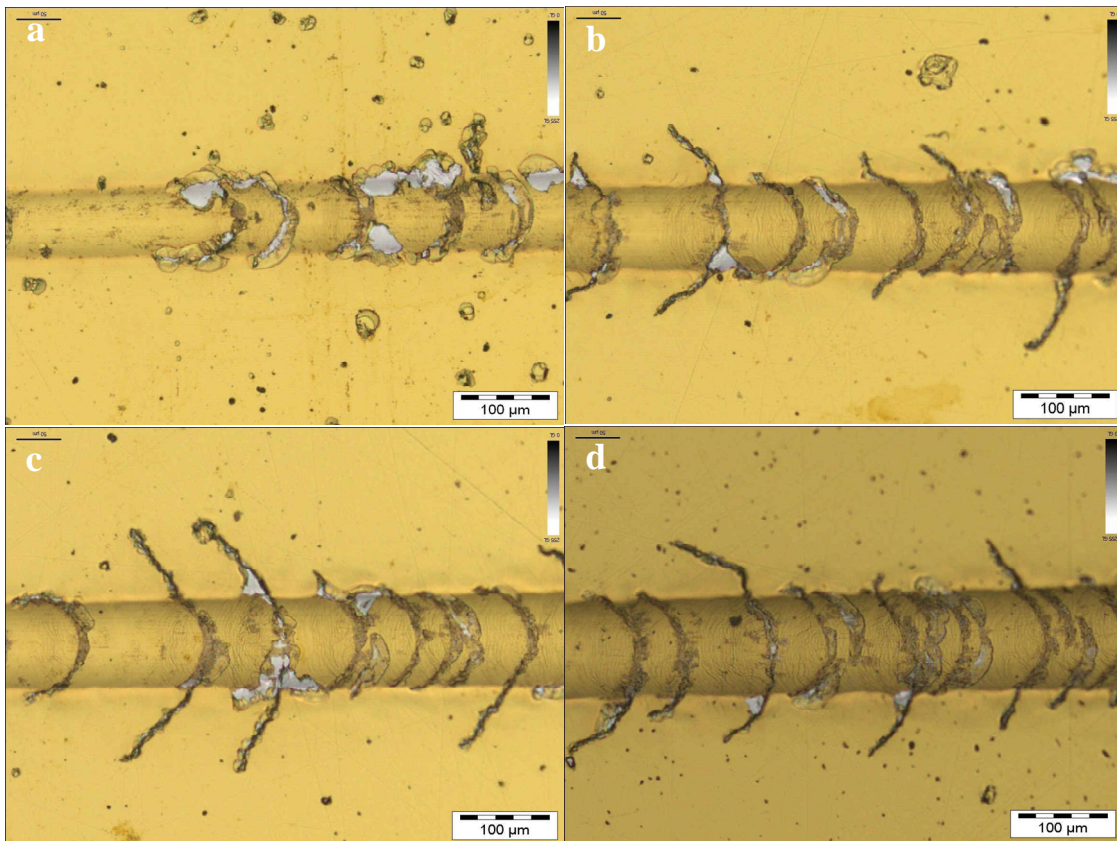
Fig. 5.9 Optical profilometer images at second critical (chipping at border with partial delamination inside scratch track) failure in bilayer and multilayers: (a) Sample BL, (b) Sample MMPI, (c) Sample MOPI, (d) Sample MOTI.

Complete delamination failure (Fig. 5.10) in bilayer was chipping at scratch edge accompanied with adhesive failure (appearance of substrate or Ti layer) within scratch track. However, in MMPI, the substrate appeared when conformal cracking stage was finished. The multilayer with optimal thickness of interlayers (MOTI) showed smearing of Ti within the scratch track as was clear from the change of substrate colour from white to silver. Smearing of Ti within scratch track in MOPI and MOTI was visible showing higher adhesion. However, in MMPI, the change in color was slightly less [69]. In addition, the scratch track width was linearly proportional to the normal load in this stage (complete failure), which indicated that indenter was in direct contact with the substrate.
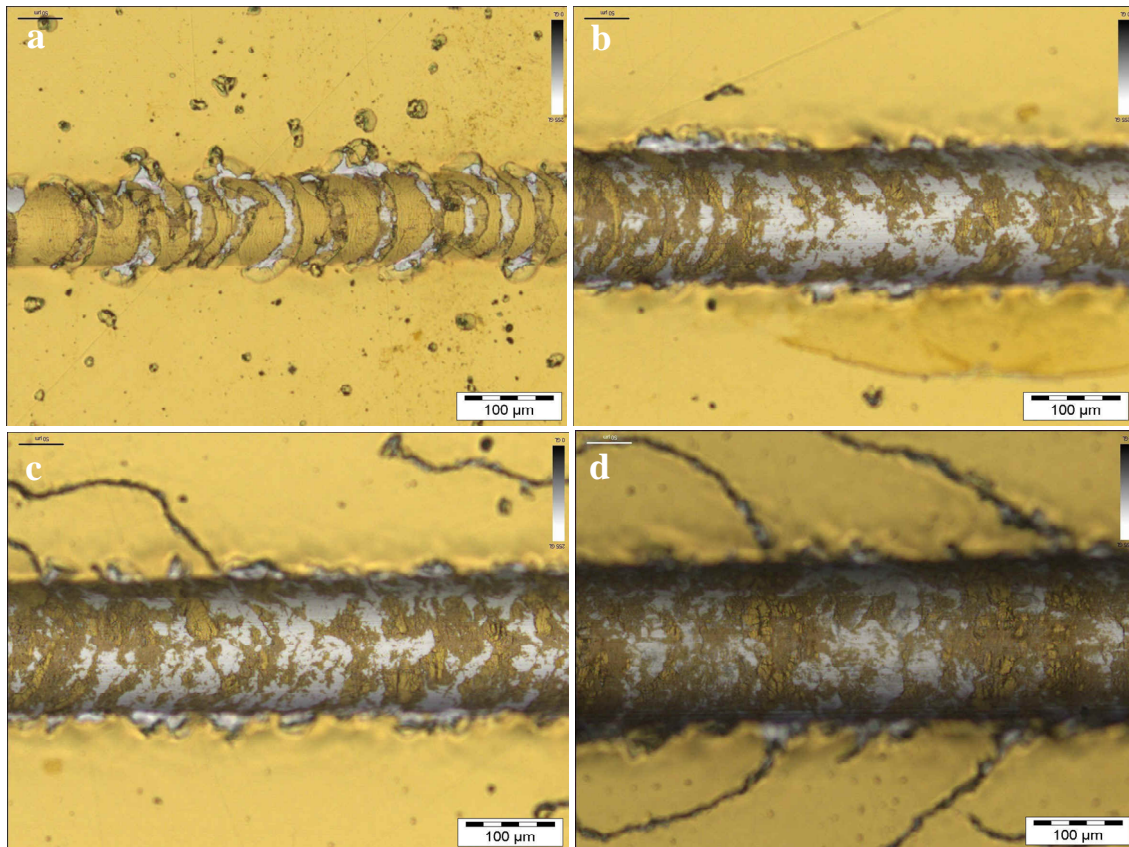
Fig. 5.10 Optical profilometer images at complete delamination failure in bilayer and multilayers: (a) Sample BL, (b) Sample MMPI, (c) Sample MOPI, and (d) Sample MOTI.

Finally, the critical load at incident of failure in coating is shown in Fig. 5.11. An increase in the multilayer coatings, first and second critical load was found to be 50 and 7 %, respectively in relation to the bilayer. When multilayer was compared with different configurations, an optimal position of the interlayer and optimal thickness of all the layers showed an increase of 11 % for the L_{C1}, and 13, 31 %, respectively for the L_{C2}. However, there was a large variation in the third critical failure load (L_{C3}). This showed that since critical load was gradually increased, owing to which most of the load was dissipated to produce deformation in the substrate.
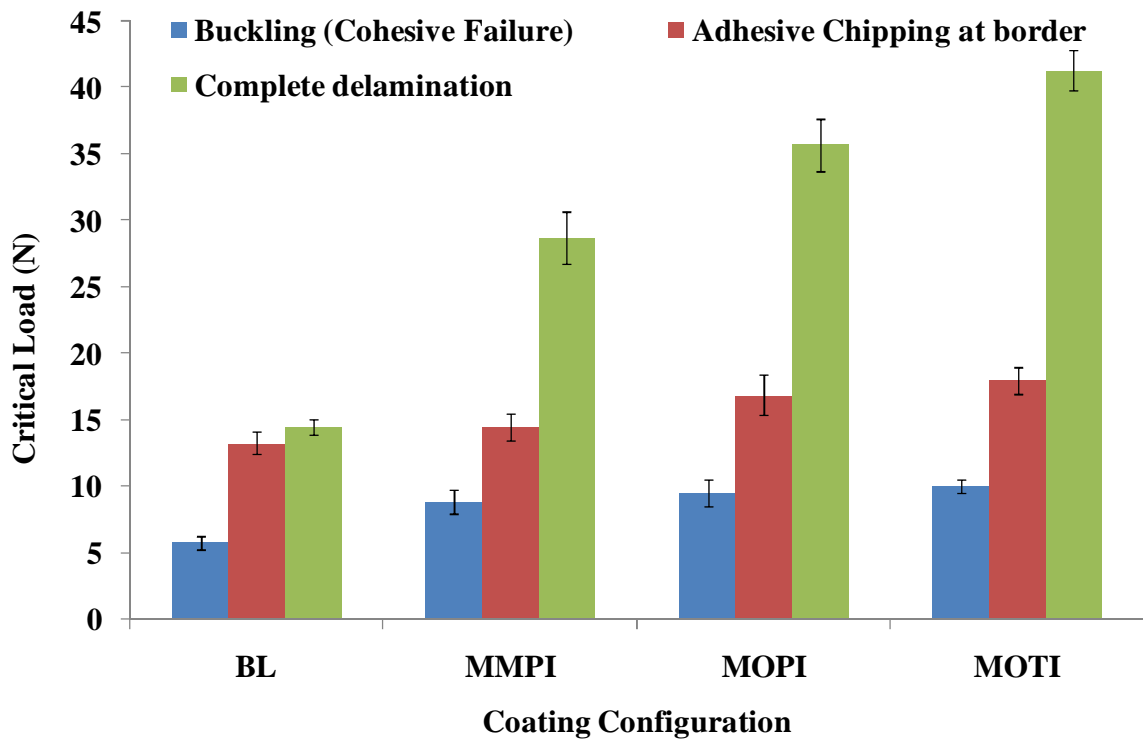
Fig. 5.11 Critical scratch loads in bilayer and multilayer configurations.

The above discussion on the results clearly indicated that standard scratch testing procedure using larger indenter radius for compliant material, like stainless steel, the depth of deformation was deep into the substrate as a result stress was generated at trailing edge of indenter. The ceramic coating being brittle was sensitive to tensile stress. The observed chipping and cracking seems the resulted failure without any knowledge about coating properties, like adhesion. In order to better evaluate

the practical coating adhesion, which clearly showed adhesive failure, the scratch tests with indenter of radius 100 µm were performed and results are described in the next section 5.2.3.2.

5.2.3.2 Scratch test with indenter of radius 100 µm

The failure modes associate with 200 µm indenter radius indicated that coating failure mechanism are cohesive one and does not involved the detachment at the coating substrate interface. Therefore, the scratch test with indenter of radius 100 µm was performed using the loading parameters described in Chapter Experimental Details. The chipping failures observed with 100 µm indenter were adhesive compared to those with 200 µm indenter. The adhesive failures at the first critical adhesive load (L_{C1}) are shown in Fig. 5.12a. The adhesive failure in all the coating configurations was semi-circular cracks probably due to buckling inside the scratch track accompanied with the first delamination within and close to the edge of scratch track. It is commonly occurring failure in hard coating on compliant substrate like stainless steel [70].

Fig. 5.12 Optical profilometer images at first delamination failure (partial appearance of substrate) in bi-layer and multilayers: (a) Sample BL, (b) Sample MMPI, (c) Sample MOPI, and (d) Sample MOTI.

The amount of spallation remained higher close to scratch border and continued until final delamination occurred in the bilayer (Fig. 5.12a). In the multilayer, it occurred with intermediate conformal cracking. It seems that thicker TiN ceramic layer in bilayer was responsible for continuous spallation of coating at relatively lower critical scratch load as shown in Fig. 5.12a where the white region of track is substrate. However, multilayer configurations with ductile interlayers absorbed more energy; consequently spallation took place at significantly high critical scratch load and remained confined within the scratch track.

Besides spallation within the scratch track, Fig. 5.12 and Fig. 5.13 showed that fine tensile cracks (semicircular crack parallel to trailing edge of indenter) on the site of buckling failure which are predominant in multilayer configurations that reflect coating was still adhered to the substrate. These cracks occurred mostly as a result of equilibrium between tensile frictional forces on trailing edge of indenter and compressive frictional force ahead of indenter [48]. This could be due to high friction stress involved by the presence of Ti interlayer with the indenter [69]. It can also be reasonably justified through that indenter at this stage is not fully in-contact with the substrate and the variation in load sufficiently reflect different coating behaviour. Also, it is expected that critical load in multilayer might be affected by the friction between Ti and diamond indenter. Specifically, the MOTI configuration showed the smearing of Ti along the scratch track due to its high adhesion. In addition, until complete delamination stage reached, buckle fracture segments in multilayer coatings remained more stable which also showed relatively good adhesion as comparison with those in the bilayer and is evident from Fig. 5.13 (a-d).

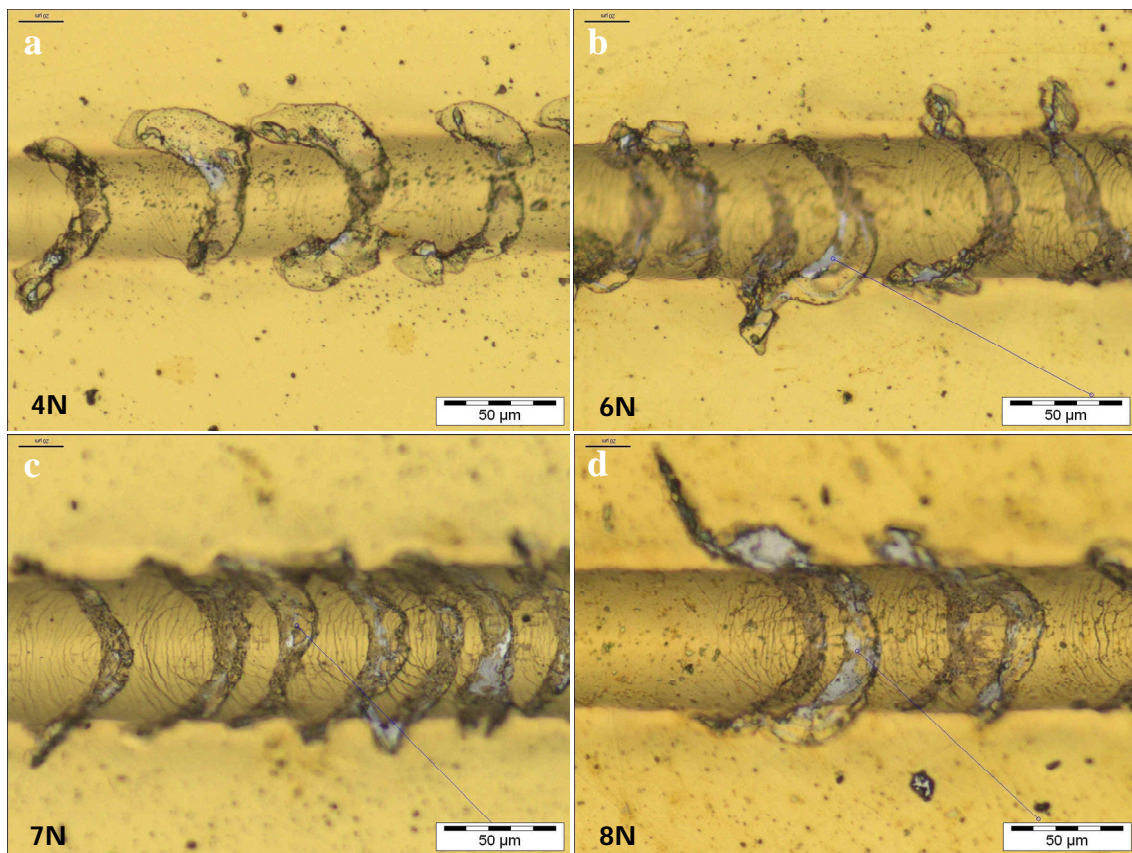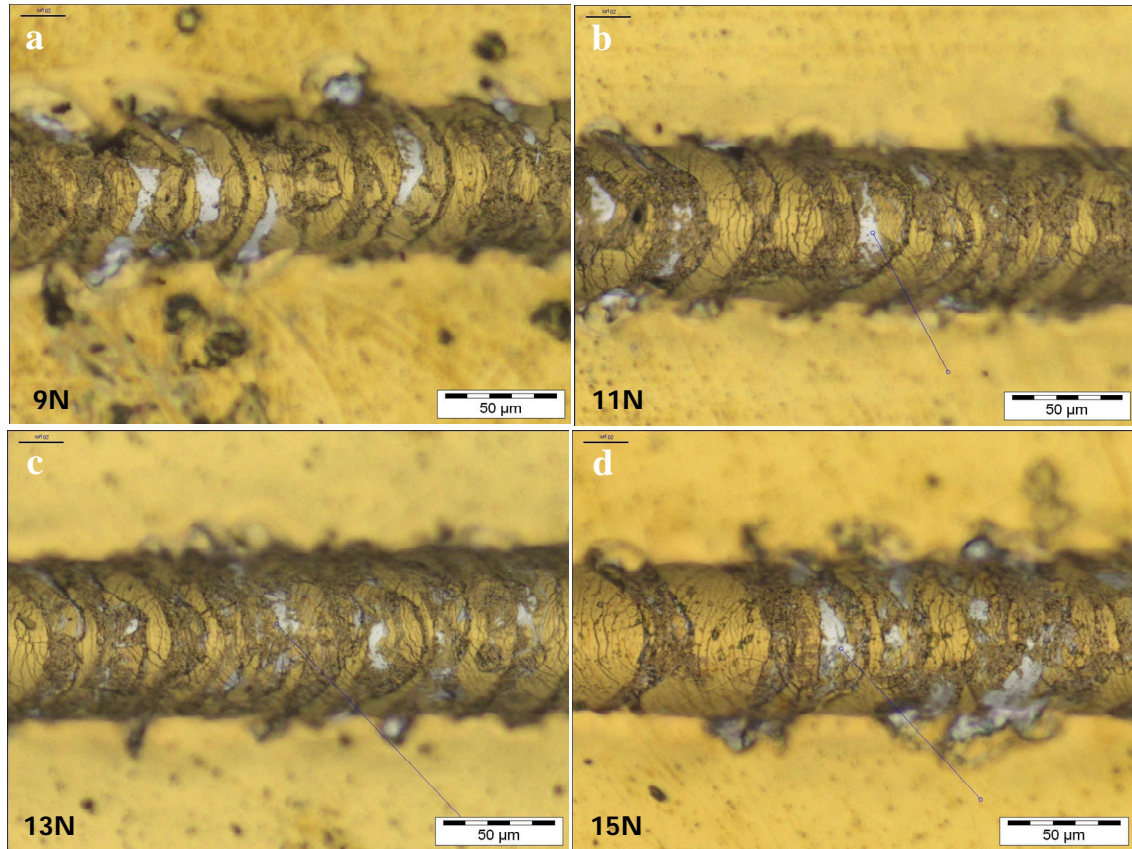Fig. 5.13 Images with optical profilometer at complete delamination failure (semicircular appearance of substrate) in bi-layer and multilayers: (a) Sample BL, (b) Sample MMPI, (c) Sample MOPI, and (d) Sample MOTI.

The adhesion of coatings in relation to critical adhesive load at incident of failure is shown in Fig. 5.14. An enhancement in the multilayer, first and second critical adhesive loads were found to be ≈ 50, 22 %, respectively that for the bilayer. When multilayer was compared with different configurations, an optimal position of the interlayer and optimal thickness of interlayer showed an improvement of ≈ 16 % for the L_{C1}, and ≈ 18 % and 27 %, respectively for the L_{C2}.
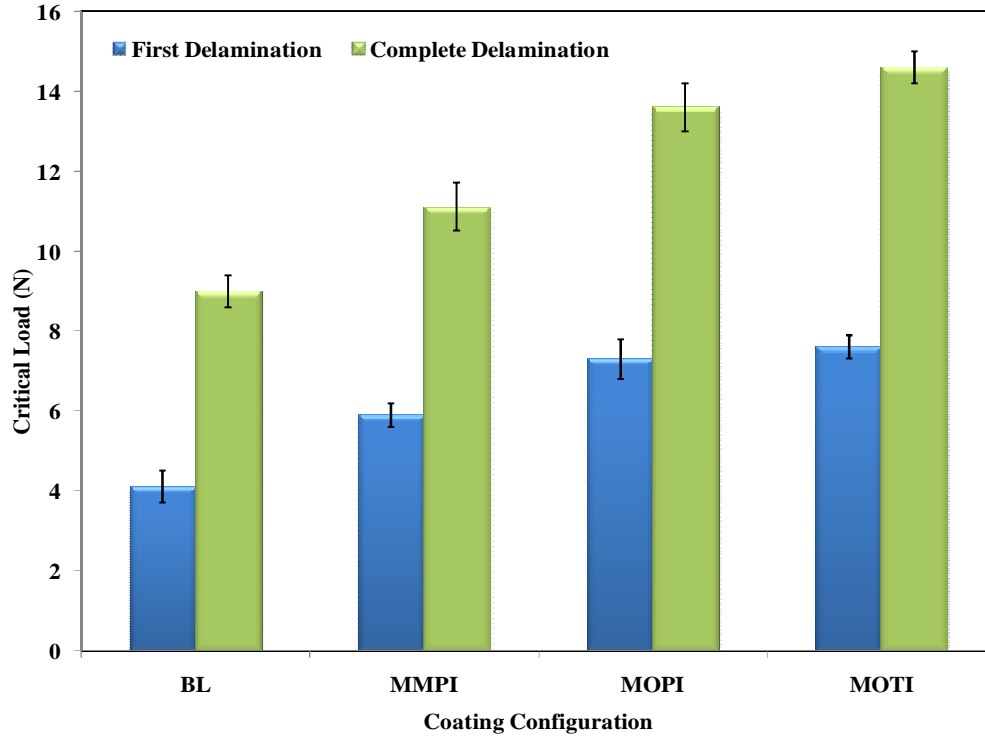
Fig. 5.14 Critical scratch loads in bilayer and multilayer configurations.

5.2.3.3 Analytical description of adhesive and cohesive failures

To further illustrate and characterize the adhesive and cohesive failures in coatings, the position of von-Mises stress relative to coating-substrate interface and the maximum normal stresses on trailing edge of scratch indenter at the incident of critical failure load were simulated with analytical modelling software package FilmDoctor® [43, 71]. This Analytical simulation was performed at the critical failure load determined with the real scratch test.

It was found that indenter with tip radius of 100 µm the position of maximum von-Mises stress was at the interface which was assumed responsible to produce the adhesive failure. However, as the critical scratch load was increased for larger indenter tip radius (200 µm), the resulting failures were cracks beyond scratch edges (cohesive failures). Because the position of the maximum von-Mises stress at critical failure load shifted deep into the substrate and probably most of the load was used to produce deformation in the substrate. As a result, sufficiently high bending induced tensile stresses on the sides of scratch track reached the critical cohesive strength of TiN which perhaps

caused failure. However, critical failure load with a smaller indenter tip radius (100 µm) was found lower and plastic flow increased and shifted to the substrate surface region. In Fig. 5.15, screen shot of analytical model with indenter size is shown. The virtual coating-substrate interface was indicated by white dash lines and black dot marks the position of the maximum von-Mises stress (Fig. 5.15 a and c). A good agreement was found between the adhesive failure and position of von-Mises stress. As indicated by red circle on scratch failure and position of von-Mises stress.

In multilayer, the critical scratch load was sufficiently high (Fig. 5.14), for which the simulated (with FilmDoctor®) maximum von-Mises stress shifted more deep into the substrate. However, von-Mises stress close to interface was considerably high enough to cause the delamination within the scratch track. This indicates relatively high adhesion of multilayers compared with that of the bi-layer.
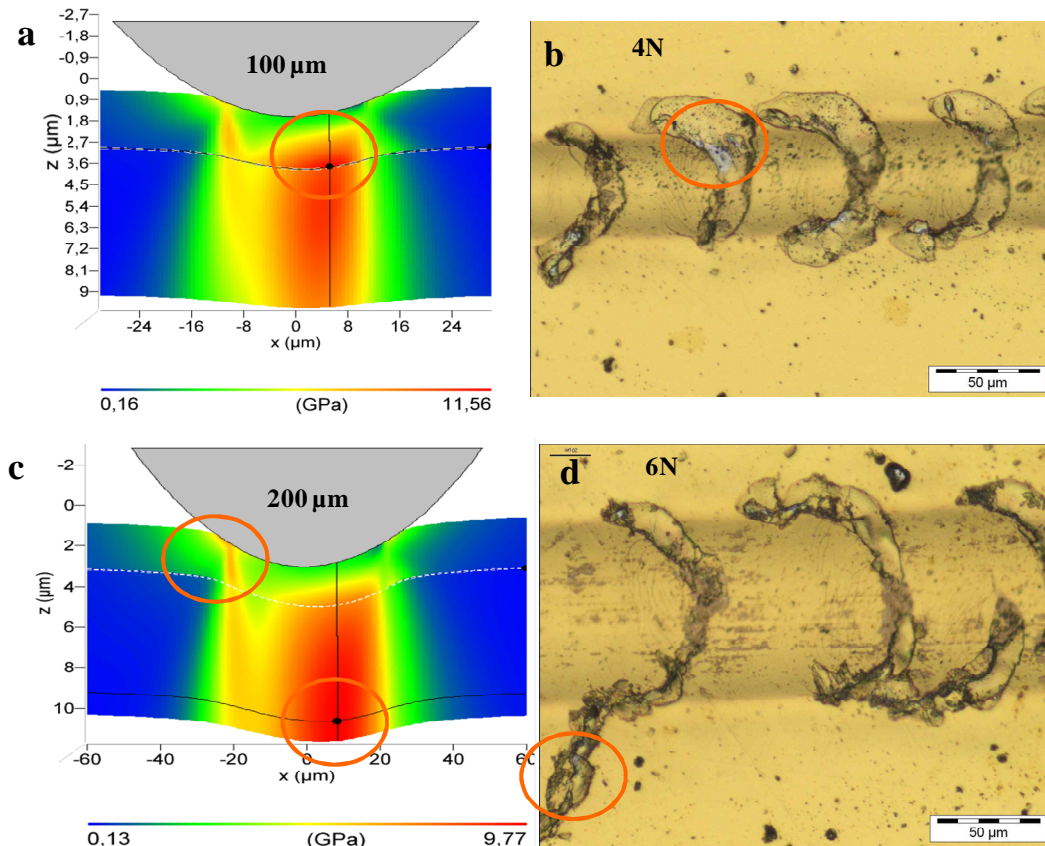
Fig. 5.15 Simulated position of von-Mises stress in bilayer with the critical scratch load (L_{C1}) along with critical failure mode: (a) With 100 µm indenter radius, (b) Optical profilometer image at

the incident of critical failure, (c) With 200 µm indenter radius, and (d) Optical profilometer image at the incident of critical failure.

From the analytical analysis, it was concluded that perhaps the shallow position of the maximum von-Mises stress was responsible for adhesive failure. Thus analytical description of scratch test for the evaluation of coating adhesion to the compliant substrate seems an efficient way for the selection of the indenter tip radius that will contribute to decrease the experimental time and resources.

5.2.4 Conclusions

An analytical description of scratch test provided comprehensive interpretation of observed failure and demonstrated its importance in order to accurately estimate specific coating properties such as practical adhesion. Considering the experimental results of scratch adhesion testing with 100 µm, it was concluded that multilayer showed significant improvement by 22 % in the first critical adhesive load. The multilayer with optimal position of interlayer showed improvement by 18 % and the best configuration with optimal thickness of interlayer showed 27 % increase in the critical adhesive load. With an introduction of two interlayers, the stiffness and hardness of all the multilayer configurations remained equivalent to the bilayer as recorded in nanoindentation results.

5.3 Influence of Ti-TiN Multilayer Coating Design on In-Plane Residual Stresses

It is indicated in the section 5.1 of this chapter that thickness of each layer in the multilayer coating has been optimized with FEM for the decrease in only axial stress component, it is possible that in-plane stress in the resultant coating might have increased. For this, it was planned to measure the in-plane stress with Wafer Curvature Method [72-74] and X-ray diffraction and FIB-DIC method. Unfortunately, coating has not been deposited on the silicon wafer, when it was put with the stainless steel substrate into the deposition chamber. After that, there were only two options left for the measurement of in-plane residual stress in the stress-optimized multilayer coatings. This section summarizes the results of intrinsic residual stress assessment with x-ray diffraction method.

5.3.1 X-ray diffraction residual stress analysis

In the Experimental Details Chapter, the critical issues related to the quantitative measurement of residual stress have been indicated. Here only qualitative comparison of the in-plane residual stress in bilayer and three multilayer configurations is presented. For this grazing-incidence, X-ray diffractograms taken under the same acquisition parameters were shown in Fig. 5.16. The diffraction patterns were smooth and shifted vertically for clarity. It is reasonable to consider that all the coatings were in compressive residual stress because magnetron sputtering deposition with bias on the substrate only induced the compressive stress in coating. The difference in peak position of bilayer and multilayer configurations diffractogram were primarily due to difference in residual stress. Considering X-ray diffractogram analyses, the high angle diffraction peak (511) in bilayer shifted to lower 2θ angle compared with multilayer sample MMPI which showed that BL sample has higher residual stress. The multilayer samples MMPI and MOPI almost have similar peak position and MOTI diffractogram shifted towards higher angle showing lower residual stress among all the multilayer configurations.
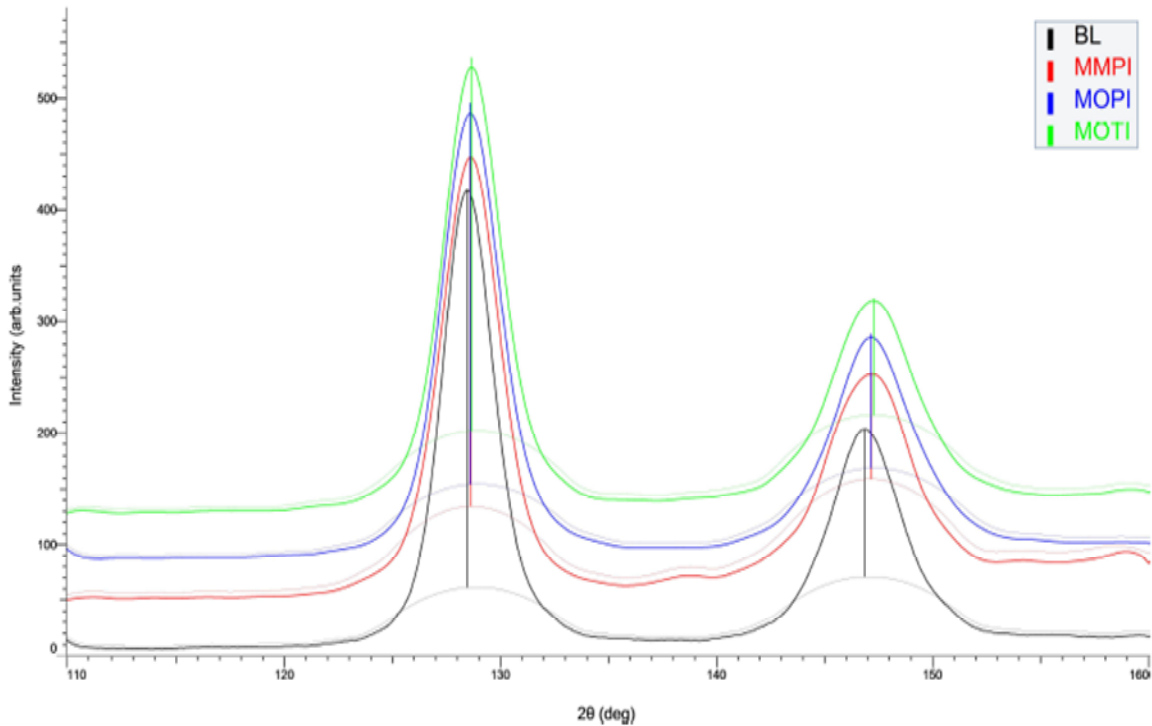
5.16 Grazing incidence X-ray diffractorgram of the bilayer and multilayer configurations

Considering the X-ray diffractorgram analyses, the bilayer (sample BL) has the highest in-plane residual stress among all the multilayer configurations (samples MMPI, MOPI and MOTI). The introduction of two interlayers significantly controlled the residual stress to improve the critical adhesive load. In addition, these results are also supported by the FIB cross-section analyses presented in Fig. 5.6 that showed columnar growth structure of PVD TiN layers which terminated with Ti interlayer in the multilayer configurations. This could be one of the main reasons of decreased residual stress and improved adhesion of multilayer configurations.

It was also noted that the expected penetration depth of X-rays at the selected grazing angle seems less than one micron. As a result, shift in peak seems to be related with the stress level in topmost coating area where open columnar structure was seen in FIB images (Fig. 5.6).

5.3.2 Conclusions

Concerning the in-plane XRD-residual stress analysis, the multilayer with optimal thickness of all layers has lower residual stresses and bilayer has higher stress. However, the multilayer with optimal position of interlayer has intermediate residual stress level.

Chapter 6 SUMMARY AND OUTLOOK

The work presented in this thesis is primarily focused on the design, development and characterization of stress-optimized multilayer PVD-coatings. The thickness of individual layers in Ti-TiN multilayer coating system comprising of six layers has been optimized for the optimal interfacial stress conditions using Finite Element Modelling (FEM). The interfacial stresses induced by the thermal and the intrinsic stresses have been taken into account. The optimization of multilayer coating configuration in terms of interlayer position and individual layer thickness has significantly decreased the interface stresses, which could improve coating adhesion to the substrate.

The multilayer coating design optimization, considerations were demonstrated through experimental investigations for the influence on adhesion, hardness and in-plane residual stress. Individual layer thickness of produced coatings comparable to the FEM based design was confirmed using focused ion beam. An improvement in adhesion was investigated through scratch test and influence on the hardness, modulus with nanoindentation. Analytical description of failure modes in scratch test was demonstrated with analytical software package FilmDoctor® that ensured accurate measurement of coating adhesion to the substrate. The in-plane residual stress in different multilayer configurations were qualitatively compared using x-ray diffraction. Not only adhesion other factors such as overall mechanical performance and in-plane residual stresses were also considered at the same time.

Multilayer coating configuration having middle positions of Ti interlayers in comparison with the bi-layer showed an improvement in scratch adhesion, decreased in in-plane residual stress without a decrease in mechanical performance such as hardness and modulus. When multilayer coating with middle positions of the Ti interlayer configuration was further compared with optimal position of interlayer configurations, a significant improvement is scratch adhesion, decrease in in-plane residual stress with comparable mechanical properties. Finally, the best coating configuration

having optimal thickness of all the layers showed much more improvement in scratch adhesion and reduction in in-plane residual stress without deterioration of coating stiffness response.

6.1 Original contribution to the scientific community

The original contributions of the present studies could be summarized as:

- A method of stress-optimization for multilayer hard coating has been developed using ANSYS finite element package. The method is useful for optimizing the interfacial stress (out-of-plane stress) particularly for the improvement of coating adhesion and in general for controlling the in-plane residual stress. It could be applied for any kind of coating and substrate material if the material properties and thickness dependent intrinsic stress profile is known.

- Guidelines for the optimization of coating/substrate adhesion by using analytical modelling of contact stresses are given, with specific focus on hard coatings;

- One new coating system has been produced, basing on the results of both FEM and analytical modelling activities;

- An innovative multi-technique characterization has been used for coating evaluation, based on the combined use of Focused Ion Beam microscopy, including residual stress analysis, nanoindentation experiments and scratch testing.

- The research has been published in international peer reviewed journal [1] (Materials & Design, Elsevier, Impact Factor 3.2) and presented at international conference and symposium [2], with publication of related peer reviewed proceedings. The presentations have gained interests from the audience and conference organizers.

6.2 Suggestions for future research

During the current research work, a few avenues have been opened which could be exploited for future research. These include:

i. The interfacial stress-optimization tools developed in the present studies could be coupled with cohesive zone finite element modelling (ANSYS damage module) to further optimize the multilayer coating architecture by taking into account also the service loading effects.

ii. The stress-optimization tools could provide the analytical description of coating failures at edges, corners and topographical irregularities of engineering components. In addition it could also help to find the optimal thickness of coatings at the location of engineering features (holes, ribs and chamfer.etc) as long as the material properties and process induced residual stresses are known.

6.3 List of Publications

1. Ali, R., M. Sebastiani, and E. Bemporad, *Influence of Ti–TiN multilayer PVD-coatings design on residual stresses and adhesion.* Materials & Design, 2015. **75**: p. 47-56.
2. R. ALI, M.S., M. RENZELLI, E. BEMPORAD. *Design of Stress-optimized Ti/TiN Multilayer PVD-Coating for Mechanical Applications.* in *Proceedings of the 28th International Conference on Surface Modification Technologies.* 2014. Tampere University of Technology, Tampere, Finland: Valardocs.

References

1. Djabella, H. and R. Arnell, *Finite element comparative study of elastic stresses in single, double layer and multilayered coated systems.* Thin solid films, 1993. **235**(1): p. 156-162.
2. Hintermann, H., *Adhesion, friction and wear of thin hard coatings.* Wear, 1984. **100**(1): p. 381-397.
3. Kim, G., et al., *Effects of the thickness of Ti buffer layer on the mechanical properties of TiN coatings.* Surface and Coatings Technology, 2002. **171**(1): p. 83-90.
4. Wang, L., et al., *Design and optimization of coating structure for the thermal barrier coatings fabricated by atmospheric plasma spraying via finite element method.* Journal of Asian Ceramic Societies, 2014. **2**(2): p. 102-116.
5. Bemporad, E., et al., *Modelling, production and characterisation of duplex coatings (HVOF and PVD) on Ti–6Al–4V substrate for specific mechanical applications.* Surface and Coatings Technology, 2007. **201**(18): p. 7652-7662.
6. Mattox, D.M., *Atomistic film growth and resulting film properties: residual film stress.* Vacuum Technology & Coating, 2001: p. 22-23.
7. Van Vliet, K. and A. Gouldstone, *First Prize Mechanical Properties of Thin Films Quantified Via Instrumented Indentation.* Surface engineering, 2001. **17**(2): p. 140-145.
8. Shan, Z. and S. Sitaraman, *Nanoindentation Studies and Material Characterization.* National Science Foundation.
9. Movchan, B. and A. Demchishin, *STRUCTURE AND PROPERTIES OF THICK CONDENSATES OF NICKEL, TITANIUM, TUNGSTEN, ALUMINUM OXIDES, AND ZIRCONIUM DIOXIDE IN VACUUM.* Fiz. Metal. Metalloved. 28: 653-60 (Oct 1969). 1969.
10. Thornton, J.A., *High rate thick film growth.* Annual review of materials science, 1977. **7**(1): p. 239-260.
11. Messier, R., A. Giri, and R. Roy, *Revised structure zone model for thin film physical structure.* Journal of Vacuum Science & Technology A, 1984. **2**(2): p. 500-503.

12. Musil, J., et al., *Ion-assisted sputtering of TiN films.* Surface and Coatings Technology, 1990. **43**: p. 259-269.
13. Anders, A., *A structure zone diagram including plasma-based deposition and ion etching.* Thin Solid Films, 2010. **518**(15): p. 4087-4090.
14. Daniel, R., et al., *The origin of stresses in magnetron-sputtered thin films with zone T structures.* Acta Materialia, 2010. **58**(7): p. 2621-2633.
15. Teixeira, V., *Residual stress and cracking in thin PVD coatings.* Vacuum, 2002. **64**(3): p. 393-399.
16. Thouless, M., *Cracking and delamination of coatings.* Journal of Vacuum Science & Technology A, 1991. **9**(4): p. 2510-2515.
17. Wiklund, U., J. Gunnars, and S. Hogmark, *Influence of residual stresses on fracture and delamination of thin hard coatings.* Wear, 1999. **232**(2): p. 262-269.
18. Gerth, J., et al., *On the wear of PVD-coated HSS hobs in dry gear cutting.* Wear, 2009. **266**(3): p. 444-452.
19. Evans, A. and J. Hutchinson, *On the mechanics of delamination and spalling in compressed films.* International Journal of Solids and Structures, 1984. **20**(5): p. 455-466.
20. Holleck, H., *Advanced concepts of PVD hard coatings.* Vacuum, 1990. **41**(7): p. 2220-2222.
21. Subramanian, C. and K. Strafford, *Review of multicomponent and multilayer coatings for tribological applications.* Wear, 1993. **165**(1): p. 85-95.
22. Aesculap®. *https://www.aesculapimplantsystems.com.*
23. Ma, K., A. Bloyce, and T. Bell, *Examination of mechanical properties and failure mechanisms of TiN and Ti– TiN multilayer coatings.* Surface and Coatings Technology, 1995. **76**: p. 297-302.
24. Drake, J., R. Williamson, and B. Rabin, *Finite element analysis of thermal residual stresses at graded ceramic-metal interfaces. Part II. Interface optimization for residual stress reduction.* Journal of Applied Physics, 1993. **74**(2): p. 1321-1326.
25. Williamson, R., B. Rabin, and J. Drake, *Finite element analysis of thermal residual stresses at graded ceramic-metal interfaces. Part I. Model description and geometrical effects.* Journal of Applied Physics, 1993. **74**(2): p. 1310-1320.
26. Chawla, V., R. Jayaganthan, and R. Chandra, *Analysis of thermal stress in magnetron sputtered TiN coating by finite element method.* Materials Chemistry and Physics, 2009. **114**(1): p. 290-294.
27. Haider, J., et al., *Simulation of thermal stress in magnetron sputtered thin coating by finite element analysis.* Journal of Materials Processing Technology, 2005. **168**(1): p. 36-41.
28. Lakkaraju, R., F. Bobaru, and S. Rohde, *Optimization of multilayer wear-resistant thin films using finite element analysis on stiff and compliant substratesa).* Journal of Vacuum Science & Technology A, 2006. **24**(1): p. 146-155.
29. Lyubimov, V., et al., *Stress analysis and failure possibility assessment of multilayer physically vapour deposited coatings.* Thin Solid Films, 1992. **207**(1): p. 117-125.
30. Vogli, E., et al., *Influence of Ti/TiAlN-multilayer designs on their residual stresses and mechanical properties.* Applied Surface Science, 2011. **257**(20): p. 8550-8557.
31. Bhadeshia, H., *Developments in martensitic and bainitic steels: role of the shape deformation.* Materials Science and Engineering: A, 2004. **378**(1): p. 34-39.
32. Pauleau, Y., *Generation and evolution of residual stresses in physical vapour-deposited thin films.* Vacuum, 2001. **61**(2): p. 175-181.
33. Mayrhofer, P.H., et al., *Influence of deposition conditions on texture development and mechanical properties of TiN coatings.* International Journal of Materials Research, 2009. **100**(8): p. 1052-1058.
34. Teixeira, V., *Mechanical integrity in PVD coatings due to the presence of residual stresses.* Thin Solid Films, 2001. **392**(2): p. 276-281.
35. Thornton, J.A. and D. Hoffman, *Stress-related effects in thin films.* Thin solid films, 1989. **171**(1): p. 5-31.
36. Hsueh, C. and A. Evans, *Residual stresses in meta/ceramic bonded strips.* Journal of the American Ceramic Society, 1985. **68**(5): p. 241-248.
37. Hutchinson, J.W., *Stresses and failure modes in thin films and multilayers.* Notes for a Dcamm Course. Technical University of Denmark, Lyngby, 1996: p. 1-45.

38. Wright, J., R. Williamson, and K. Maggs, *Finite element analysis of the effectiveness of interlayers in reducing thermal residual stresses in diamond films.* Materials Science and Engineering: A, 1994. **187**(1): p. 87-96.

39. Smith, W. and J. Hashemi, *Foundations of Materials Science and Engineering. 2006.* McGraw-Hill.

40. Design, G., *Cambridge Engineering Selector (CES).* 2002, Cambridge.

41. Zhang, X., et al., *Analyses of interfacial stresses and normal stresses within an elongated film strip/substrate system.* Thin solid films, 2006. **515**(4): p. 2251-2256.

42. Ansys, I., *ANSYS advanced analysis techniques guide.* Ansys Help, 2007.

43. Schwarzer, N., et al., *Optimization of the Scratch Test for specific coating designs.* Surface and Coatings Technology, 2011. **206**(6): p. 1327-1335.

44. Chudoba, T., N. Schwarzer, and F. Richter, *Steps towards a mechanical Modelling of layered systems.* Surface and Coatings Technology, 2002. **154**(2): p. 140-151.

45. Schwarzer, N., *Coating design due to analytical modelling of mechanical contact problems on multilayer systems.* Surface and Coatings Technology, 2000. **133**: p. 397-402.

46. Schwarzer, N., F. Richter, and G. Hecht, *The elastic field in a coated half-space under Hertzian pressure distribution.* Surface and Coatings Technology, 1999. **114**(2): p. 292-303.

47. Sun, Y., A. Bloyce, and T. Bell, *Finite element analysis of plastic deformation of various TiN coating/substrate systems under normal contact with a rigid sphere.* Thin Solid Films, 1995. **271**(1): p. 122-131.

48. Burnett, P. and D. Rickerby, *The scratch adhesion test: an elastic-plastic indentation analysis.* Thin Solid Films, 1988. **157**(2): p. 233-254.

49. FilmDoctor®:. *Software demonstration package, www.siomec.de/FilmDoctor.*

50. Mahan, J.E., *Physical vapour deposition of thin films.* Physical Vapour Deposition of Thin Films, by John E. Mahan, pp. 336. ISBN 0-471-33001-9. Wiley-VCH, January 2000., 2000. **1**.

51. Giannuzzi, L.A. and F.A. Stevie, *Introduction to focused ion beams: instrumentation, theory, techniques and practice.* 2005: Springer Science & Business Media.

52. Reyntjens, S. and R. Puers, *A review of focused ion beam applications in microsystem technology.* Journal of Micromechanics and Microengineering, 2001. **11**(4): p. 287.

53. Atkins, A. and D. Tabor, *Plastic indentation in metals with cones.* Journal of the Mechanics and Physics of Solids, 1965. **13**(3): p. 149-164.

54. Fisher, A., *Cripps, Nanoindentation.* 2002, Springer, New York.

55. Johnson, K.L. and K.L. Johnson, *Contact mechanics.* 1987: Cambridge university press.

56. Oliver, W.C. and G.M. Pharr, *An improved technique for determining hardness and elastic modulus using load and displacement sensing indentation experiments.* Journal of Materials Research, 1992. **7**(06): p. 1564-1583.

57. Oliver, W.C. and G.M. Pharr, *Measurement of hardness and elastic modulus by instrumented indentation: Advances in understanding and refinements to methodology.* Journal of Materials Research, 2004. **19**(01): p. 3-20.

58. Sneddon, I.N., *The relation between load and penetration in the axisymmetric Boussinesq problem for a punch of arbitrary profile.* International Journal of Engineering Science, 1965. **3**(1): p. 47-57.

59. Gonczy, S.T. and N. Randall, *An ASTM standard for quantitative scratch adhesion testing of thin, hard ceramic coatings.* International Journal of Applied Ceramic Technology, 2005. **2**(5): p. 422-428.

60. STANDARD, B., *Advanced technical ceramics—Methods of test for ceramic coatings—.* 2003.

61. Fitzpatrick, M., et al., *Determination of Residual Stresses by X-ray Diffraction. Measurement Good Practice Guide No. 52.* NPL. UK. Teddington. Middlesex, 2002.

62. Prevey, P.S., *X-ray diffraction residual stress techniques.* ASM International, ASM Handbook., 1986. **10**: p. 380-392.

63. Leoni, M., et al., *(Ti, Cr) N and Ti/TiN PVD coatings on 304 stainless steel substrates: Texture and residual stress.* Thin Solid Films, 1999. **345**(2): p. 263-269.

64. Korsunsky, A.M., M. Sebastiani, and E. Bemporad, *Focused ion beam ring drilling for residual stress evaluation.* Materials Letters, 2009. **63**(22): p. 1961-1963.

65.   Gerth, J. and U. Wiklund, *The influence of metallic interlayers on the adhesion of PVD TiN coatings on high-speed steel.* Wear, 2008. **264**(9): p. 885-892.

66.   Stefenelli, M., et al., *X-ray analysis of residual stress gradients in TiN coatings by a Laplace space approach and cross-sectional nanodiffraction: a critical comparison.* Journal of applied crystallography, 2013. **46**(5): p. 1378-1385.

67.   Salas, O., et al., *Tribological behaviour of candidate coatings for Al die casting dies.* Surface and Coatings Technology, 2003. **172**(2): p. 117-127.

68.   Attar, F. and T. Johannesson, *Adhesion evaluation of thin ceramic coatings on tool steel using the scratch testing technique.* Surface and coatings technology, 1996. **78**(1): p. 87-102.

69.   Bull, S., et al., *The use of scratch adhesion testing for the determination of interfacial adhesion: the importance of frictional drag.* Surface and Coatings Technology, 1988. **36**(1): p. 503-517.

70.   Bull, S., *Failure mode maps in the thin film scratch adhesion test.* Tribology International, 1997. **30**(7): p. 491-498.

71.   Fuchs, M. and G. Favaro, *Physical characterization of coated surfaces—Part II: scratch test.* Available online: www. csm-instruments. com/en/Physical-characterization-of-coated-surfaces-Part-II-% 3A-Scratch-Test (accessed on 17 April 2014).

72.   Janssen, G., et al., *Celebrating the 100th anniversary of the Stoney equation for film stress: Developments from polycrystalline steel strips to single crystal silicon wafers.* Thin Solid Films, 2009. **517**(6): p. 1858-1867.

73.   Standardization, E.C.f., *Advanced technical ceramics-Methods of test for ceramic coatings - Part 11: Determination of internal stress by the Stoney formula.* 2005: Brussels.

74.   Stoney, G.G., *The tension of metallic films deposited by electrolysis.* Proceedings of the Royal Society of London. Series A, Containing Papers of a Mathematical and Physical Character, 1909. **82**(553): p. 172-175.

APPENDIX-A. ANSYS Input File for Interfacial Stress-optimization

/com, author

/com, Rali

/com, University of Roma Tre

/com, Interfacial stress-optimization

FINISH

/CLEAR

/prep7

/Units,Si

T_dep = 300 + 273 ! Deposition Temperature (673)

t_amb = 25 + 273 ! Ambient Temperature (298)

/ com, **** Materials Properties of stainless steel ***

mp, nuxy, 1, 0.30

mp, ex, 1, 203E9

tb,miso,1,2,4

tbtemp, t_amb

tbpt, , 0.002, 406E6

tbpt, , 0.003, 609E6

/ com, **** layers of Ti ***

mp, nuxy, 2, 0.32   ! Invoke Mechanical Properties of Ti

mp, ex, 2, 116E9

tb,miso, 2,2,4

tbtemp, t_amb

tbpt, , 0.002, 232E6

tbpt, , 0.025, 232E6

tbpt, , 0.05, 232E6

tbpt, , 0.1, 232E6

tbtemp, t_dep

tbpt, , 0.002, 232E6

tbpt, , 0.025, 232E6

tbpt, , 0.05, 232E6

tbpt, , 0.1, 232E6

mp, c, 2, 528

mp, kxx,2, 17

mp, alpx, 2, 9e-6

mp, reft, 2, T_dep

/ com, **** layers of TiN ***

mp, ex, 3, 600e9   ! recalls the properties of TiN_1

mp, nuxy, 3, 0.25

mp, c, 3, 528

mp, kxx, 3, 19

mp, alpx, 3, 9.40e-6

mp, reft, 3, T_dep

mp, ex, 4, 600e9   ! recalls the properties of TiN_2

mp, nuxy, 4, 0.25

mp, c, 4, 528

mp, kxx, 4, 19

mp, alpx, 4, 9.40e-6

mp, reft, 4, T_dep

mp, ex, 5, 600e9   ! recalls the properties of TiN_3

mp, nuxy, 5, 0.25

mp, c, 5, 528

mp, kxx, 5, 19

mp, alpx, 5, 9.40e-6

mp, reft, 5, T_dep

/ com, **** coating layers ***

n_Ti = 3

n_TiN = n_Ti

n_tot = n_Ti + n_TiN

/ com, Geometry and mesh **** ****

/ com, thermal and structural elements **** ****

```
ET, 1, PLANE77          ! 2D planar mesh heating elements

keyopt,1,3,1

/ com, geometry parameters

re = 300e-6      ! outer radius of the disc

th_sub = 300e-6     ! thickness of the disc

w = 50e-6      ! disk depth

TiN_1 = 0.800e-6   ! Thickness of 1st layer of TiN (1.5 micron)

TiN_2 = 0.800e-6

TiN_3 = 0.800e-6          ! Thickness of 2nd layer of TiN (1.5 micron)

Ti_bond = 0.060e-6    ! Thickness of Bond layer (50 nm)

Ti_Buffer_1 = 0.060e-6

Ti_Buffer_2 = 0.060e-6

T_Thi = 2*TI_BUFFER_1 + Ti_Bond + TIN_1 + TIN_2 + TiN_3

rectng, 0, re, 0, th_sub

rectng, 0, re, th_sub, th_sub + TI_BOND

rectng, 0, re, th_sub + TI_BOND, th_sub + TI_BOND + TIN_1

rectng, 0, re, th_sub + TI_BOND + TIN_1, th_sub + TI_BOND + TIN_1 + Ti_Buffer_1

rectng, 0, re, th_sub + TI_BOND + TIN_1 + Ti_Buffer_1 , th_sub +   TI_BOND + TIN_1 + Ti_Buffer_1 + TIN_2

rectng, 0, re, th_sub + TI_BOND + TIN_1 + Ti_Buffer_1 + TIN_2 , th_sub + TI_BOND + TIN_1 + Ti_Buffer_1 +
TIN_2 + TI_Buffer_2

rectng, 0, re, th_sub + TI_BOND + TIN_1 + Ti_Buffer_1 + TIN_2 + TI_Buffer_2,th_sub + TI_BOND + TIN_1 +
Ti_Buffer_1 + TIN_2 + TI_Buffer_2 + TiN_3

nummrg,kp,1e-9

numcmp,line

/ com, **** attribution of elements and materials to areas ****

asel, s, , , 1     ! steel

aatt, 1, , 1

allsel

asel, s, , , 2    !bond layer

asel, A, , , 4     !Ti_Buffer_1

asel, A, , , 6     !Ti_Buffer_2
```

```
aatt, 2, , 1

allsel

asel, s, , , 3    !Coating of TiN 1st layer

asel, A, , , 5    !Coating of TiN 2nd layer

asel, A, , , 7    !Coating of TiN 3rd layer

aatt, 3, , 1

allsel

/ com, parameters of the mesh ***** *****

etin = 12      ! elements in which the thickness of the Titanium Nitride layers are divided

ebond = 3      ! elements in which the thickness of bond layer is divided

eti = 3      ! elements in which the thickness of titanium layers are divided

eacc = 150     ! elements in which the thickness of the steel is divided

oriz = 300      ! elements within the inner region leaving edges

racc = 25     ! rate of mesh thickening of in the steel

incr = 2                ! rate of mesh thickening at interface

base = 8

/com,****mesh****

lesize, 3, , , oriz

lesize, 4, , , eacc, racc

lesize, 1, , , base

lesize, 2, , , eacc, 1/racc

lesize, 5, , , ebond

lesize, 7, , , ebond

*do, j, 3, (n_tot+1)*3,3

    lesize, j, , , oriz

*enddo

*do, j, 10, (n_tot+1)*3+1,6

  lesize, j, , , etin

  lesize, j-2, , , etin

*enddo

*do, j, 13, (n_tot+1)*3-2, 6
```

```
  lesize, j, , , eti

  lesize, j-2, , , eti

*enddo

aglue,all

amesh,all

nummrg,all,1e-9

/com,****SOLVER*****

  antype,0

  csys, 0

/com,****Porto tutto a 400 °C****

  antype,static

  nropt,full

  outres,all

/prep7

  ddele,all

  d,all,temp,t_amb          ! imposes finally the ambient temperature

/solu

    solve

/ com, change in structural elements **** ****

/prep7

etchg

*IF,TiN_1,GE,0.800e-6,Then

esel,s,mat,,3

inistate,set,mat,3

inistate,define,,all,,,-3.30e9,,-3.30e9,,,

*endif

allsel

*IF,TiN_2,GE,0.800e-6,Then

esel,s,mat,,4

inistate,set,mat,4

inistate,define,,all,,,-3.30e9,,-3.30e9,,,
```

```
*endif

allsel

*IF,TiN_3,GE,0.800e-6,Then

esel,s,mat,,5

inistate,set,mat,5

inistate,define,,all,,,-3.30e9,,-3.30e9,,,

*endif

allsel

esel,s,mat,,2

inistate,set,mat,2

inistate,define,,all,,,1e9,,1e9,,,

allsel

/solu

        NSEL,S,LOC,Y,0

        D,All,Uy,0

allsel

        antype,static

        nropt,full

        nlgeom,on

        neqit,400

        cnvtol,u,1e-2

        outres,all,all

        ldread,temp,1,,,,,rth

        TREF,T_dep

solve

!!********** Optimization of Sy***************

/POST1

        NSEL,all

        NSEL,s,loc,y,300e-6,303.250E-6

/com,****Retrieve the results parametrically and set the state variables and objective function parameters****

/POST1
```

NSORT,S,Y

*GET,SY,SORT, ,Max   !defines max. stress for optimization routine

Lsel,s,line,,7,22,3   !All layers are included

/prep7

LSUM

ALLSEL

*GET,T_Th,Line,,LENG   ! *Get stor model or result information into parameters

LGWRITE,Ti-TiN,txt,C:\Users\administrator\

!LGWRITE,Ti-TiN,txt,C:\Users\Rashid\

/com,****Establish parameters****

/OPT

/com,****Enter OPT and specify the analysis file****

OPANL,Ti-TiN,txt,C:\Users\administrator\   ! Assign optimize.txt as analysis file

!OPANL,Ti-TiN,txt,C:\Users\Rashid\

/com,****Declare optimization variables and begin the optimization process****

OPVAR,TIN_3,DV,0.500e-6,1e-6

OPVAR,TI_BUFFER_2,DV,0.060e-6,0.100e-6

OPVAR,TIN_2,DV,0.600e-6,1e-6

OPVAR,TI_BUFFER_1,DV,0.060e-6,0.100e-6

OPVAR,TIN_1,DV,0.500e-6,1e-6

OPVAR,TI_BOND,DV,0.06e-6,0.100e-6

/com,****Declare limit to the design ,State variable (12)****

OPVAR,T_Th,SV,3.0e-6,3.40E-6

/com,****Define the objective that you are trying to optimize (13)****

OPVAR,SY,OBJ

/com,****Choose optimization tool or method (14)****

OPTYPE,SUBP

/com,****Controls for sub-problem optimization****

OPFRST,,,5   ! OPFRST, NITR, SIZE, DELT

OPPRNT,FULL   ! Activates detailed optimization summary printout.

/com,****Run the optimization (15)****

OPEXE   ! Run optimization

/com,**** Review the results from the 10 iterations (16)****

OPLIST,ALL,,0